HIGH TEMPERATURE HIGH PRESSURE STUDIES ON SOME NOVEL MATERIALS USING LASER HEATED DIAMOND ANVIL CELL FACILITY

By

NISHANT NATVARLAL PATEL

PHYS01201104017

Bhabha Atomic Research Centre,
Mumbai – 400085,
INDIA

A thesis submitted to the
Board of Studies in Physical Sciences

In partial fulfillment of requirements
for the Degree of

DOCTOR OF PHILOSOPHY

of

HOMI BHABHA NATIONAL INSTITUTE

August, 2018

Homi Bhabha National Institute

Recommendations of the Viva Voce Committee

As members of the Viva Voce Committee, we certify that we have read the dissertation prepared by **Shri. Nishant Natvarlal Patel** entitled **"High Temperature High Pressure Studies on Some Novel Materials using Laser Heated Diamond Anvil Cell Facility"** and recommend that it may be accepted as fulfilling the thesis requirement for the award of Degree of Doctor of Philosophy.

Chairman	**Prof. N.K. Sahoo**		**Date:** 6/3/2019
Guide/ Convener	**Prof. M.N. Deo**		**Date:** 06/03/2019
Examiner	**Prof. Amartya Sengupta**	Sengupta	**Date:** 06/03/19
Member	**Prof. T.C. Kaushik**		**Date:** 06/03/2019
Member	**Prof. N.V. Chandrashekar**	N.V. Chandrashekar	**Date:** 15/3/19
Technology Advisor	**Dr. Meenakshi Sunder**	Meenakshi	**Date:** 06/03/2019

Final approval and acceptance of this thesis is contingent upon the candidate's submission of the final copies of the thesis to HBNI.

I hereby certify that I have read this thesis prepared under my direction and recommend that it may be accepted as fulfilling the thesis requirement.

Date: 06/03/2019

Place: Mumbai

06/03/2019

Dr. M. N. Deo
(Thesis Supervisor)

STATEMENT BY AUTHOR

This dissertation has been submitted in partial fulfillment of requirements for an advanced degree at Homi Bhabha National Institute (HBNI) and is deposited in the Library to be made available to borrowers under rules of the HBNI.

Brief quotations from this dissertation are allowable without special permission, provided that accurate acknowledgement of source is made. Requests for permission for extended quotation from or reproduction of this manuscript in whole or in part may be granted by the Competent Authority of HBNI when in his or her judgment the proposed use of the material is in the interests of scholarship. In all other instances, however, permission must be obtained from the author.

Patel 16/08/2018

Nishant Natvarlal Patel

Mumbai

August 16, 2018

DECLARATION

I, hereby declare that the investigation presented in the thesis has been carried out by me. The work is original and has not been submitted earlier as a whole or in part for a degree / diploma at this or any other Institution / University.

16/08/2018

Mumbai

Nishant Natvarlal Patel

August 16, 2018

List of Publications arising from the thesis

Journal

1) High Pressure Melting Curve of Osmium up to 35 GPa
   Nishant N. Patel and Meenakshi Sunder,
   J. Appl. Phys., 125, 055902 (2019).

2) Laser heated diamond anvil cell facility for high temperature high pressure research: Application to material synthesis and melting studies
   Nishant N. Patel, S. Meenakshi and Surinder M. Sharma,
   Ind. J. Phys. 92, 1295 (2018)

3) Pressure-induced polymorphism in hypervalent CsI_3,
   Nishant N. Patel, M. Sunder, A B Garg and H K Poswal,
   Phys. Rev. B, **96**, 174114 (2017).

4) Synthesis of unconventional stoichiometric compounds in the K—Br system at high pressures.
   Nishant N. Patel, Ashok K. Verma, A. K. Mishra, M. Sunder and Surinder M. Sharma,
   Phys. Chem. Chem. Phys., **19**, 7996 (2017).

5) LHDAC Setup for High Temperature and High Pressure Studies
   Nishant N Patel, S. Meenakshi and S. M. Sharma,
   AIP Conference Proceedings, **1591**, 664 (2014).

Conferences

1) LHDAC Setup for High Temperature and High Pressure Studies.
   Nishant N Patel, S. Meenakshi and S. M. Sharma,
   58th DAE Solid State Physics Symposium, Thapar University, Patiala, Punjab, India (2013).

2) Diamond Anvil Cell based Laser Heating facility for High Temperature - High Pressure Research: Some Recent Results.

   Nishant N Patel,

   49th Course: High Pressure Crystallography: Status Artis and Emerging Opportunities, Erice-Sicily, Italy (2016).

3) K-Br System under Pressure: Synthesis of Unconventional Stoichiometric Compounds.

   Nishant N. Patel, Ashok K. Verma, A. K. Mishra, Meenakshi Sunder and Surinder M. Sharma,

   MRSI National Symposium on Advances in Functional and Exotic Materials, Trichy, Tamil Nadu, India (2018).

Patel 16/08/2018

Signature of Student:

Date: 16/08/2018

Dedicated to My Parents,

Sons Vyom and Shlok & My Beloved Wife Purvi

ACKNOWLEDGEMENTS

I would like to thank all the people who have helped and motivated me during my doctoral work. First and foremost I would like to express my gratitude to my advisor Prof. M. N. Deo for his constant support and encouragement during my doctoral work. I would like to express my gratitude to Dr. Meenakshi Sunder for her unconditional support and encouragement throughout my research work. I owe much of the knowledge about high pressure physics from her. She has introduced me to the field of high pressure high temperature experimental physics.

Special thanks to the members of my doctoral committee Prof. N. K. Sahoo (BARC), Prof. T.C. Kaushik (BARC) and Prof. N.V. Chandrashekar (IGCAR) for their critical comments and suggestions. I am thankful to my colleagues Dr. A. K. Verma, Dr. A. B. Garg, Dr. V. Srihari, Dr. S. Karmakar and Dr. H. K. Poswal for their generous help during the Ph.D. work. My special thanks to Dr. S. M. Sharma for sharing his insight into the high pressure physics. I am thankful to Mr. A. Dwivedi, Ms. R. Vasanthi, Mr. R. R. Pokale and Mr. M. M. Tandel for their technical help during the research work.

On this occasion I am deeply grateful to my colleague and friend Dr. Ajay K. Mishra and Dr. Ram Niranjan for spending their valuable time in crucial discussions with me and for stimulating my thinking at every stage of my research work. I also express my sincere gratitude to my parents for their continuous encouragement and support. At the end I would like to thank my beloved wife Purvi for her persistent encouragement and support throughout the tenure of this doctoral work.

Contents

Page No.

SYNOPSIS

Material behaviour at high pressure and high temperature conditions is of significant interest in a wide range of scientific research areas, especially in material science, planetary interiors and geophysics [1-3]. They are pivotal in the understanding and modeling of the earth's interior giving us insight into the melting behavior of elemental materials at high pressure high temperature (HPHT) conditions. Hence *in-situ* HPHT techniques are indispensable for studying physical properties of the minerals forming the Earth's core and mantle. In addition, HPHT studies are important for determination of P-V-T equation of state (EOS), phase transitions and phase stability of materials [1, 4]. Recent research based on experimental investigations and computational approaches provide several exciting examples, where non-ambient conditions result in unexpected phenomena and structural changes [1, 5].

Materials can be subjected to HPHT, in static pressure conditions, using i) piston-cylinder [6], (ii) multi anvils [7], (iii) toroid anvil [8], (iv) Paris-Edinburgh press [9], (v) diamond anvil cell (DAC) based resistive heating [10], (vi) DAC based laser heating [11]. In the case of dynamic pressure studies HPHT is achieved by shock compression [12]. Laser heated diamond anvil cell (LHDAC) and shock compressions are only techniques capable of generating ultrahigh pressure and temperature (*i.e.*, P > 100 GPa, and T of the order of thousands of Kelvin). LHDAC exploits the exclusive physical and optical properties of diamonds *viz.*, hardness/strength, transparency across a broad range of electromagnetic spectrum, electrical insulator *etc.,* and provides a unique opportunity to investigate material properties at extreme thermodynamic conditions wherein the nature of the chemical bonding in atoms change along with modifications in their valence states and electronegativity. This results in an enhanced chemical reactivity thus increasing the feasibility of direct elemental reaction between inert materials, leading to the formation of a plethora of novel and exotic phases with interesting properties [13, 14]. The main advantage of the LHDAC technique over dynamic shock experiments is that it provides a controlled means of achieving pressure and temperature conditions that can be held constant for long periods of time. Hence it can be easily integrated with a variety of diagnostic techniques like X-ray diffraction, Raman scattering, Brillouin scattering, electrical transport and synchrotron based micro-probing techniques thereby facilitating the investigation of a variety of pressure induced phenomena like melting, structural phase transformations, changes in nature of bonding, chemical reactivity, and novel material synthesis [3]. The independent control of pressure and temperature enables us to map the P-T phase space which provides an opportunity to synthesize hitherto unknown unconventional phases that can be quenched and examined at ambient temperature and pressure. In recent times, the synthesis of superhard materials such as novel carbides, nitrides and borides have emerged as one of the frontline problems in the field of HPHT research [15]. The results reported in this thesis illustrate some interesting aspects of HPHT research on some selected materials with exciting properties. The work reported includes the following:

(1) Development of instrumentation for laboratory based single sided LHDAC facility at Purnima Labs, BARC, Mumbai for HPHT experiments.

(2) LHDAC based HPHT melting experiments for determination of high pressure melting curve of osmium and KBr up to 35 and 24 GPa respectively.

(3) LHDAC based HPHT synthesis of gallium nitride (GaN) and molybdenum nitride (Mo_2N).

(4) Synthesis of two new stoichiometric compounds, namely KBr_3 and KBr_5 at high pressures in the K-Br system based on HPHT experiments.

(5) Results of ambient temperature high pressure synchrotron based x-ray diffraction, Raman and electrical resistance study of CsI_3.

The thesis is divided into six chapters. **Chapter 1** gives a brief introduction to the field of HPHT research highlighting its importance in diverse areas of scientific research. A review of the available HPHT generation techniques along with their capabilities and limitations are also reported in this chapter. Justification of our choice of laser heated diamond anvil cell (LHDAC) technique over other techniques in terms of maximum pressure and temperature range achieved and adaptability to various diagnostic techniques has also been described in this chapter.

Chapter 2 presents a detailed technical discussion and description of instrumentation of a single sided LHDAC facility, which has been designed and set up at Purnima Labs, Bhabha Atomic Research Centre (BARC), Mumbai, India. The salient feature of the LHDAC facility is an angular geometry with an off-axis incidence of the NIR laser beam on the sample. The advantage of this geometry over the usual 180° heating geometry is described at length in this chapter. The set up utilizes the excellent features of the Yb doped fibre laser system such as ideal beam quality, high stability, fibre delivery, compactness, selectivity of operating wavelength and a reliability that is superior than the conventional solid state or gas laser. The chapter also gives a detailed discussion on the challenges associated with accurate sample temperature measurement, sample loading method and technical details of spectroradiometric method for temperature determination. The importance of 10X magnification of sample image at spectrometer input slit and use of 30 μm pinhole as the input slit of spectrometer for accurate sample temperature measurements have also been discussed. A brief review of the various melting criteria used in LHDAC based high pressure melting studies and the various methods employed for detection of onset of melting, *viz.*, laser speckle method, flash heating method and temperature plateau method have also been included in the chapter with specific examples. The last part of the chapter reports the results of HPHT synthesis studies and melting experiments at ambient and high pressures to demonstrate the versatility of the LHDAC facility for HPHT investigations. The examples of synthesis experiments include the HPHT synthesis of GaN by direct reaction of Ga metal with N_2 at 9 GPa and 1925 K and the HPHT synthesis of Mo_2N at 7 GPa and 2000 K using Mo metal and N_2 as precursors. The results of high pressure melting experiments on KBr upto 24 GPa by employing laser speckle method for detection of onset of melting establish the suitability of the LHDAC set up for melting studies.

Chapter 3 describes the results of high pressure melting study on Osmium up to 35 GPa. Osmium (Os) is an important refractory metal having the highest density ($\rho \sim 22.59$ g/cc) among all the naturally occurring elements [16]. It has exceptional properties such as, high hardness, a bulk modulus that is almost comparable to that of diamond under ambient temperature and pressure conditions and extremely low thermal expansion and compressibility [17]. Its unique properties make Os, a potentially important element for synthesis of superhard materials. Despite these interesting properties and extensive high pressure theoretical investigations on osmium, there have been no experimental reports to date on the high pressure melting curve $T_m(P)$ of Os. Motivated by these studies, high pressure melting study on Os was carried out up to 35 GPa using the LHDAC facility described in **Chapter 2** in conjunction with Mao Bell type DAC. The pressure measurement and detection of onset of melting was carried out by ruby fluorescence and laser speckle method respectively. The Simon-Glatzel equation was fitted to the experimental data points in T *vs* P plot to get melting slope (dT/dP) at ambient pressure, which was then compared with various reported theoretical melting slopes [18,19]. The fitted parameter deduced from Simon-Glatzel equation was used to extrapolate the melting curve to higher pressures. One of the important parameter of interest is the Grüneisen parameter ($\gamma(\rho)$) as a function of density/volume, which in conjunction with Lindeman melting equation, enable us to compute melting curve at any desired pressure. Hence a parameterized form of $\gamma(\rho)$ based on the method described by Burakovsky *et al* was considered in the present study and the Grüneisen parameter was determined analytically using the experimentally obtained melting slope [18]. The study also leads us to conclude that the Grüneisen parameter is dependent on Z alone at very high compression.

Recent reports of synthesis and stabilization of phases with unconventional stoichiometries, *viz.*, KCl_3, $NaCl_3$, Na_3Cl, lithium polyhydride *etc.*, and the theoretical prediction of many more such exotic compounds have made solid state chemistry under static compression one of the most interesting and active areas of high pressure research [20-22]. **Chapter 4** discusses the results of HPHT study on potassium-bromine (K-Br) system. The study has indicated the synthesis of two new stoichiometric compounds, namely KBr_3 and KBr_5 at high pressures in the K-Br system. A room temperature high pressure chemical reaction between KBr and Br_2 resulted in the formation of an orthorhombic KBr_3 (*SG: Pnma*) at ~ 2.0 GPa. Further compression lead to the formation of a monoclinic KBr_5 (*SG:* $P2_1$) at ~ 6.0 GPa. Raman spectroscopy and x-ray diffraction measurements were employed for detection and characterization of the newly synthesized compounds. This is the first ever experimental synthesis of a 1:5 stoichiometric compound in the alkali halogen system. The most unusual observation accompanying the reaction is an anomalously large increase of sample chamber pressure (> 2GPa) during the KBr_5 formation. This observation and the existence of isothermal conditions in DAC based experiments lead us to conjecture that the change in internal energy is converted directly to mechanical work during formation of KBr_5. Furthermore, the KBr_5 phase remained stable up to the highest pressure (24 GPa) of our study. On decompression, KBr_5 remained stable down to 5.0 GPa. High-pressure laser heating experiments carried out to get further insight into the stability of newly synthesized KBr_5 has revealed that at high pressure (14-20 GPa) and high temperature (~ 1500 K), KBr_5 decomposes into a trigonal KBr_3 (*SG: P-3c1*), instead of orthorhombic KBr_3 (SG: *Pnma*), and Br_2 with a large volume reduction. The bulk modulus (B_0) of KBr5 and KBr3 in orthorhombic and trigonal phase obtained by fitting the 3rd order Birch Murnaghan equation of state (BM EOS) is 11.2, 11.8 and 15.5 GPa respectively. Collaborative first-principles structural searches were carried out to solve the composition and related crystal structures [23-24]. The proposed structures give good description to the experimental Raman spectra and x-ray diffraction data.

Chapter 5 reports the results of high pressure investigations on cesium triiodide (CsI_3). The alkali halides serve as the simplest and model ionic solid for both static and dynamic high-pressure investigations [25, 26]. Research interest in alkali halogen system has been rekindled by the reports of synthesis of new unconventional stoichiometric compounds with unusual bonding and electronic properties. $NaCl_3$ at HPHT reported to be stable between 20 to 48 GPa has a orthorhombic (SG: *Pnma)* structure; at 48 GPa it reportedly undergoes a phase transformation into a metallic cubic (SG: *Pm-3n*) phase [20]. In K-Cl system, KCl_3 has been reported to crystallize in a trigonal (SG: *P-3c1*) structure at HPHT and it reportedly undergoes a structural transition to a cubic (SG: *Pm-3n*) phase at higher pressure [22]. On the other hand, in the K-Br system, as discussed in Chapter 4 of this thesis, KBr_3 was synthesized in orthorhombic

(SG:*Pnma*) phase above 2 GPa and was found to crystallize in the trigonal (*SG: P-3c1*) phase during decomposition of KBr_5 at HPHT [5]. Thus high pressure structural evolution in alkali trihalides is far from clarity due to the absence of trigonal, orthorhombic and cubic phase in $NaCl_3$, KCl_3 and KBr_3 respectively. The high pressure study of CsI_3 was carried out with an aim to understand the structural transition sequence of alkali trihalides. The results of ambient temperature high pressure synchrotron based x-ray diffraction, Raman and electrical resistance study of CsI_3 up to 29, 25 and 8 GPa respectively have been reported in this chapter. Three distinct phase transitions were observed under quasihydrostatic condition. The ambient orthorhombic (*SG:Pnma*) phase of CsI_3 was observed to be stable up to a pressure of ~1.3 GPa beyond which it was found to undergo a phase transition to a trigonal (*SG:P*-3*c*1) phase. The stability region of the trigonal phase was found to be up to 22.6 GPa. Above this pressure the trigonal phase was seen to transform to a cubic (*SG: Pm*-3*n*) phase which remained stable till the maximum pressure of 29 GPa achieved in this study. A third order BM EOS fit to the pressure volume (P-V) data yielded a bulk modulus of 17.7(9) GPa for the trigonal phase. Raman spectroscopic measurements however indicated three phase transitions at ~ 1.3, 4.0 and 22.6 GPa respectively. The electrical resistance measured in the low pressure region up to 8 GPa indicated an electronic transition around 4 GPa confirming the Raman result observed at 4.0 GPa. The P-V data when transformed to the universal equation of state (UEOS) showed a deviation from linearity around 4.0 GPa confirming the electronic transition. The present study has thus revealed a three phase structural transition sequence in alkali trihalides, *viz.*, orthorhombic (*SG: Pnma*) to trigonal (*SG: P*-3*c*1) to a cubic (*SG: Pm*-3*n*) phase.

The thesis is concluded with a brief summary in **Chapter** 6 for a quick glance at the key aspects of the present work as well as a concise discussion on some major areas for future scope of HPHT research. In addition, appendices have been included in the thesis to give a detailed description of the working principles of the various experimental techniques and software packages used for the studies presented in this thesis *viz.*, DAC, x-ray diffraction measurements, Raman spectroscopy, scanning electron microscopy, ruby fluorescence spectroscopy *etc*.

References

[1] H. K. Mao, X. J. Chen, Y. Ding, B. Li and L. Wang, *Rev. Mod. Phys.* **90**, 015007 (2018).

[2] Z. Konôpková, R. S. McWilliams, N. Gómez-Pérez and A. F. Goncharov, *Nature* **534**, 99 (2016).

[3] R. Torchio, O. Mathon and S. Pascarelli, *Coord. Chem. Rev*. **277-278**, 80 (2014).

[4] H. Kojitani, S. Terata, M. Ohsawa, D. Mori, Y. Inaguma and M. Akaogi, *American Minrologist*, **102**, 2032 (2017).

[5] N. N. Patel, A. K. Verma, A. K. Mishra, M. Sunder and S. M. Sharma, *Phys. Chem. Chem. Phys.* **19**, 7996 (2017).

[6] R. Hinrichs and J. A. H. da Jornada, *Rev. Sci. Inst*., **68**, 193 (1997).

[7] S. Zhai and E. Ito, *Geoscience Frontiers* **2**, 101 (2011).

[8] L. G. Khvostantsev, V. N. Slesarev and V. V. Brazhkin, *High Pressure Res*. **24**, 371 (2004).

[9] G. Morard , M. Mezouar , N. Rey , R. Poloni , A. Merlen , S. Le Floch , P. Toulemonde , S. Pascarelli , A. San-Miguel , C. Sanloup and G. Fiquet, *High Pressure Res.* **27**, 223 (2007).

[10] S. Pasternak, G. Aquilanti, S. Pascarelli, R. Poloni, B. Canny, B. V. Coulet and L. Zhang, *Rev Sci Instrum*. **79**, 085103 (2008).

[11] Y. Meng, R. Hrubiak, E. Rod, R. Boehler and G. Shen, *Rev. Sci. Instrum*. **86**, 072201 (2015).

[12] W. J. Nellis in G.L. Chiarotti, M. Bernasconi M & L. Ulivi (Eds) *High Pressure Phenomena*, (Societa Italiana di Fisica), p 109 (2002).

[13] A. F. Young, C. Sanloup, E. Gregoryanz, S. Scandolo, R. J. Hemley and H. K. Mao, *Phys. Rev. Lett*. **96,** 155501 (2006).

[14] A. Friedrich, B. Winkler, E. A. J. Arellano and L. Bayarjargal, *Materials* **4**, 1648 (2011).

[15] A. Salamat, R. A. Fischer, R. Briggs, M. I. McMahon and S. Petitgirard, *Coord. Chem. Rev*. **277-278**, 15 (2014).

[16] J.W. Arblaster, *Johnson Matthey Technol. Rev*. **58**, 137 (2014).

[17] J.W. Arblaster, *Platinum Met. Rev*. **57**, 177 (2013).

[18] L. Burakovsky, N. Burakovsky and D. L. Preston, *Phys. Rev. B,* **92**, 174105 (2015).

[19] K. D. Joshi, S. C. Gupta and S. Banerjee, *J. Phys.: Condens. Matter*, **21**, 415402 (2009).

[20] W. Zhang, A. R. Oganov, A. F. Goncharov, Q. Zhu, S. E.Boulfelfel, A. O. Lyakhov, E. Stavrou, M. Somayazulu, V. B. Prakapenka and Z. Konopkova, *Science*, **342**, 1502 (2013).

[21] C. Pépin, P. Loubeyre, F. Occelli and P. Dumas, *Proc. Nat. Acad. Sci*., **112**, 7672 (2015).

[22] W. Zhang, A. R. Oganov, Q. Zhu, S. S. Lobanov, E. Stavrou and A. F. Goncharov, *Sci. Rep.*, **6**, 26265 (2016).

[23] A. O. Lyakhov, A. R. Oganov, H. T. Stokes and Q. Zhu, *Comput. Phys. Commun.* , **184**, 1172 (2013).

[24] G. Kresse, and D. Joubert, *Phys. Rev. B*, **59**, 1758 (1999).

[25] S. Wei, C. Zhu, Q. Li, Y. Zhou, Q. Li and Y. Ma, Phys. Chem. Chem. Phys.,**16**, 17924, (2014).

[26] Y. Xu, J. S. Tse, A. R. Oganov, T. Cui, H. Wang, Y. Ma, and G. Zou, Phys. Rev B **79**, 144110 (2009).

List of Figures

List of Tables

List of Abbreviations

Abbreviation	**Full form**
ADXRD	Angle dispersive x-ray diffraction
BM EOS	Birch Murnaghan equation of state
CN	Coordination number
COHP	Crystal orbit Hamiltonian populations
CW	Continuous wave
DA	Diamond anvil
DAC	Diamond anvil cell
DOS	Density of states
DPSS	Diode pumped solid state laser
ECXRD	Extreme condition x-ray diffraction
EOS	Equation of state
ELF	Electron-localization function
HPHT	High pressure high temperature
IR	Infrared
LED	Light emitting diode
LHDAC	Laser heated diamond anvil cell
MAA	Multi anvil apparatus
MO	Molecular orbital
MIR	Mid infrared

NIR	Near infrared
NMR	Nuclear magnetic resonance
OCP	One component plasma
P	Pressure
PAW	Projector augmented wave
PBE	Perdew-Burke-Ernzerhof
PEP	Paris–Edinburgh press
PTM	Pressure transmitting medium
PV	Pressure volume
QMD	Quantum molecular dynamic
QTH	Quartz tungsten halogen lamp
SEM	Scanning electron microscope
SG	Space group
T	Temperature
T_c	Superconducting temperature
T_m	Melting temperature
UEOS	Universal equation of state
V	Volume
WC	Tungsten carbide
XAFS	X-ray absorption fine structure
XES	X-ray emission spectroscopy

Chapter 1

Introduction

This chapter gives an overview of the field of high pressure high temperature (HPHT) research. It begins with a discussion on the significance of HPHT research in diverse scientific areas. A summary of some recent developments is followed by a brief discussion on pressure and temperature effects on materials. The last part of the chapter gives a short review of the various HPHT generation techniques and some of the diagnostic techniques, which are currently coupled to diamond anvil cell based laser heating technique.

1.1 Significance of High Pressure High Temperature (HPHT) Research

1.1.1 Geophysics

Material behaviour under combined conditions of extreme high pressure (P) and high temperature (T) was motivated by the curiosity to understand the Earth's composition. Emil Wiecherd was first to propose that the Earth is made up of heavy solid iron core [1]. Further, observations of distant earthquakes by Beno Gutenberg led to the two shell Earth core model with first accurate determination of core radius of ~2900 km [1,2]. Later, many seismologists and geophysicists improved the model of Earth's interior [3]. Even though information about different layers of Earth's interior, like crust, upper mantle, lower mantle, outer core and inner core, as shown in Fig. 1.1, have been established based on density, the composition of these layers are still unknown. For *e.g.*, the density difference of around 10 % has been found between actual density of Earth's outer core and that of pure iron at similar pressure and temperature. Hence, it is believed that outer core is made up of yet unknown composition of iron along with some light elements like silicon, carbon, nitrogen, oxygen and sulfur [4]. Laboratory based HPHT technique capable of simulating extreme high pressures (~ 360 GPa) and high temperature condition (~ 5000-6000 K) equivalent to the pressure and temperature at the center of Earth will be advantageous to resolve Earth core's composition and the crystal structure of iron at the pressure and temperature conditions existing at the inner core. The knowledge of the structure and geochemical composition of Earth's interior would be useful to understand heat flow mechanism and its modeling [5].

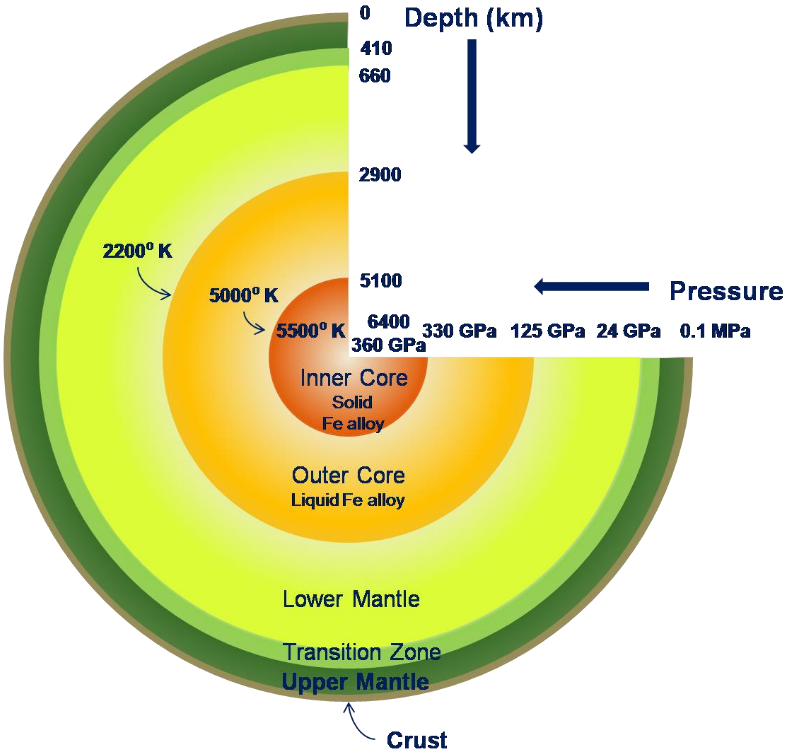

Fig. 1.1: *Cross sectional view of earth's interior with depth, corresponding pressure and temperature range.*

1.1.2 Planetary physics

Apart from geophysicist, planetary physicists have also been fascinated in understanding the composition of the planetary interior with an aim to provide plausible explanation for the perplexing planetary observations. The spectroscopic evidence for the presence of gases like methane (CH_4), nitrogen (N_2), carbon dioxide (CO_2), water/ice (H_2O) *etc.*, in exoplanets, gas giant planets and their satellites by the various outer space missions has motivated several studies on the physical and chemical properties of these gases and their mixtures at HPHT. For *e.g.*, clathrates of CH_4, CO_2 and other gases form the geology of extraterrestrial bodies in our solar system. Clathrates are basically cage structures comprising a host water molecule in which guest gas molecules are trapped. The study of stability of different clathrates under HPHT conditions is important to understand the composition and geology of the outer space bodies. Interestingly, methane clathrate, (also called methane hydrate) not only exists in icy moons and exoplanets but also in Earth's oceanic deposit and polar ice sheets [6, 7]. Release of CH_4 from these deposits into the Earth's atmosphere would be one of the major concern for global warming. Similarly, the detection of strong geomagnetic field associated with Jupiter has puzzled planetary scientists [8]. Unlike Earth, the gas giants lack liquid iron core to generate magnetic field. The explanation put forward to explain the origin of this field is that the pressure and temperature at the centre of Jupiter is sufficient to metallize hydrogen, (Fig. 1.2) which is in superconducting phase and produces the magnetic field [9,10]. This has led to a worldwide research in high pressure laboratories to metallize hydrogen under HPHT.

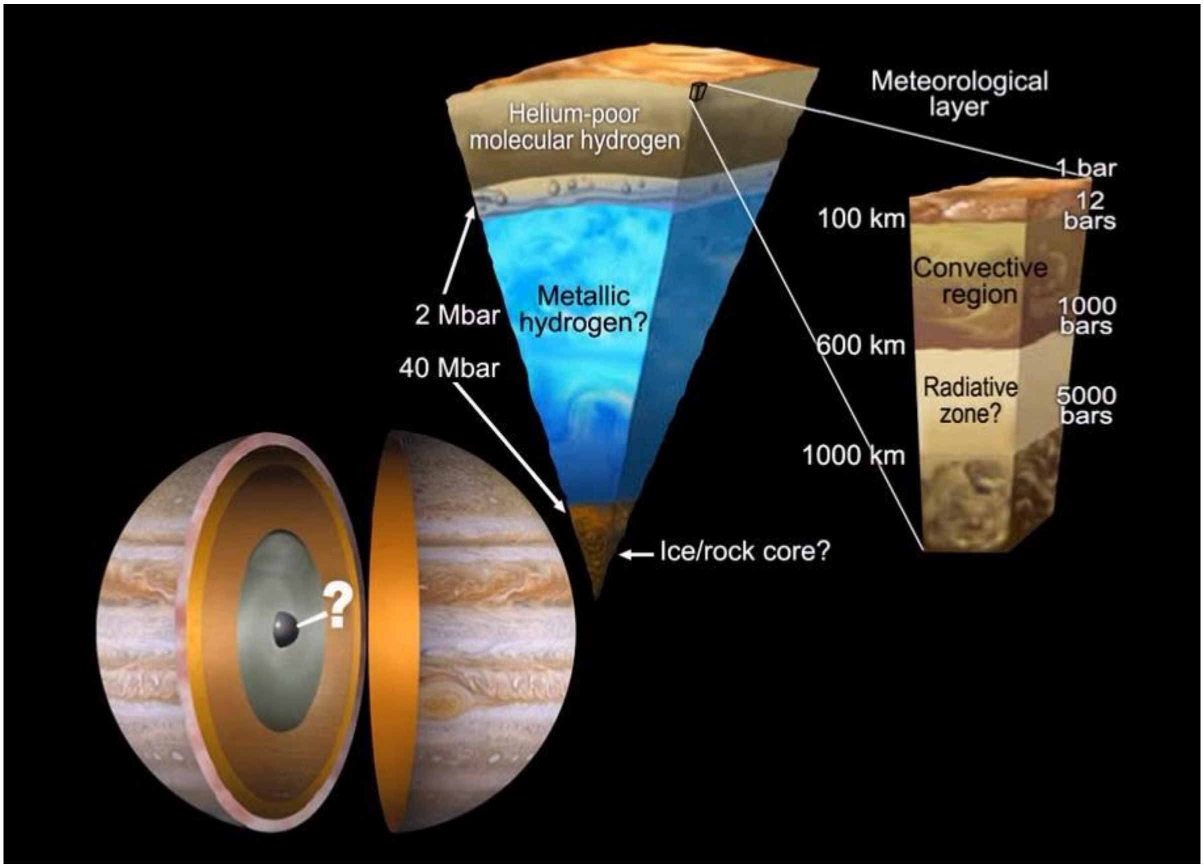

Fig. 1.2: *Interior of Jupiter and the associated pressure range [11].*

1.1.3 High T_c superconductors

The plethora of experimental studies reported in recent times to metallize hydrogen under extreme conditions have been motivated by the theoretical prediction that metallic hydrogen might be a superconductor, up to room temperature (290 K), far higher than any other known candidate material [12]. Till date however, hydrogen, which has been subjected to a maximum pressure of 495 GPa, has not fulfilled the dream of observation of metallic hydrogen [13, 14] and hence the observation of room temperature superconductor. Recent studies have explored the hydrogen rich compounds for observation of high temperature superconductivity [15]. The report of highest recorded superconducting temperature of ~ 203 K at 1.5 Mbar in H_2S [16] has opened up new avenues in the search for high T_c superconductors.

Chemical pre-compression in metal hydride is seen to lower the metallization pressure, compared to pure H_2, in metal hydrides [17]. Moreover, such materials dominated by hydrogen element, high temperature superconductivity can be found after metallization [18]. Concurrently, several metal hydrides have been predicted to be superconducting with high superconducting temperature (T_c) [19]. For *e.g.*, high T_c (~235 K) is predicted for polyhydride of Ca [19]. Similarly, alkali polyhydrides are also predicted to be superconductor [20]. Reaction of alkali hydrides, *i.e.*, LiH, NaH, KH *etc.*, and alkaline earth metals with hydrogen at HPHT could provide possible pathways for the synthesis of some of these novel superconducting polyhydrides.

1.1.4 Synthesis of novel stoichiometric compounds

High pressure and high temperature conditions provide a pathway to unexpected phenomena and stoichiometries in various materials. For instance, alkali halides (CsI), which are prototype ionic compounds and insulator at ambient conditions, show pressure induced metallization [21]. CsI is reported to be superconductor above 180 GPa with T_c ~2 K [22, 23]. The exotic behaviour of these simple compounds at extreme thermodynamic conditions has given impetus to HPHT research in alkali-halogen system. The recent prediction of counter intuitive compounds such as $NaCl_3$, $NaCl_7$, Na_3Cl, Na_2Cl_3 and $NaCl_7$ in (Na-Cl) system at high pressure and successful synthesis of some of these compounds, *i.e.*, $NaCl_3$, $NaCl_7$ and Na_3Cl at HPHT conditions are notable examples of effect of high pressure and high temperature on stoichiometries [24]. Apart from alkali-halogen system, Mg-O, Fe-O, Xe-H *etc.*, are recent examples where novel compounds have been theoretically predicted at high pressures [25-27]. Similarly, $Xe(H_2)_7$ and $Xe(H_2)_8$, in Xe-H system are reported to contain the highest hydrogen content among all the known compounds [27].

1.1.5 Synthesis of superhard materials

The search for superhard materials is driven by the constant industrial demand for new materials with favourable properties like high strength, low compressibility *etc*. Towards this end, HPHT conditions provide a unique opportunity to access chemical reaction pathways that are unachievable by conventional chemical routes for the synthesis of compounds with desirable properties. Among the numerous materials synthesized at HPHT conditions, the ones, which are retrievable in metastable phase at ambient conditions, have proved to be a boon for technological advancement. Diamond, one of the allotrope of carbon, is the most classic example of superhard material synthesized deep inside the earth as well as in laboratories above 1500 K and 7.5 GPa. The kinetic stability and metastable nature of diamond has enabled its retrieval at ambient conditions. It is also noteworthy that the synthesis of amorphous diamond having bulk modulus, hardness and thermal conductivity comparable to diamond has also been recently reported [28]. Another renowned material produced under pressure is cubic boron nitride, c-BN, ranked second after diamond in hardness and finding a great many commercial uses [29]. Other promising superhard binary systems are the C-N and Si-N system [30]. Interestingly, many transition metal nitrides, carbides and borides are also promising candidates for ultrahard materials with superlative properties [31]. Examples of binary transition metal carbides, nitrides and borides with remarkable properties are the extremely high melting points of HfC (4201 K) [31] and TaC (4223 K) [31], the large bulk modulus of OsB (453 GPa) [31], and the ultra-hardness of ReB2

(H_v = 30–48 GPa), WB4 (H_v = 46 GPa) and MoN (H_v = 38.5 GPa) [31]. Bulk modulus and hardness of few binary transition metal nitrides including the nitrides synthesized as a part of this thesis work are summarized in Table 1.1. High bulk modulus values are reported for platinum group (VIII) metal borides and nitrides with stoichiometry MN_2/MB_2 , where M stands for transition metal [32-36]. Structurally unusual features are observed in these nitrides, which contain dinitrogen units within their crystal structures.

Table 1.1: List of transition metal nitrides with bulk modulus and hardness

Group	Compound	Bulk Modulus (GPa)	Hardness (GPa)	Reference
IV	TiN	277-289	18-21	[37-41]
	TiN_2	385	-----	[42]
	δ-ZrN	248	15.8-17.4	[37, 43]
	c-Zr_3N_4	217-223	18	[44, 45]
	δ-HfN	260	16.3-19.5	[37, 43]
	c-Hf_3N_4	227-241	-----	[46, 47]
V	VN	265	6-15	[48, 49]
	δ-NbN	348	13.3-20	[37, 43]
	β-Ta_2N	360	-----	[50]
	ε-TaN	288	24.7	[51]
	η-Ta_2N_3	319	16	[52, 53]

VI	hp-CrN	243	-----	[48]
	Cr_2N	275	15.7	[39, 51]
	δ-MoN	345	38.5	[51, 54, 55]
	γ-Mo_2N	301-304	35.7	[39,55,]
VII	Re_3N	395	-----	[56]
	Re_2N	401	-----	[56]
VIII	ε-Fe_7N_3	168	-----	[57]
	γ-Fe_4N	155	-----	[57]
	ε-Fe_3N	172	7.4	[58]
	OsN_2	358	-----	[32]
	IrN_2	428	-----	[32]
	RhN_2	235	-----	[33]
	RuN_2	330	-----	[34]
	PtN_2	354-372	-----	[35]
IIb	Zn_3N_2	228	-----	[36]
IIIa	**GaN**	188	-----	[59]

1.1.6 Melting under pressure

Melting behaviour of some elementary solids *e.g.*, maxima in melting curve observed in Li and Na have surprised researchers [60, 61]. Also, the nearly zero melting slopes at high pressures reported for some transition metals like Sn [62] and their disagreement with the experimental shock data and theoretically calculated melting temperatures are still debatable. High pressure melting curve of iron is important for understanding the heat convection and modeling of the Earth's core, owing to the fact that, the outer core in made up of iron along with other lighter elements (like C, S, O *etc*.) in molten state. Although several models, starting from Lindemann criteria to Kechin model, have been proposed yet they fail to explain microscopic mechanism of melting [63, 64]. Hence, establishment of high pressure melting curves of various elemental solids will be pivotal to understanding the phenomenon of melting.

1.2 Effect of Pressure and Temperature on Condensed Matter

Pressure (P), volume (V) and temperature (T) are the three thermodynamical variables which decide the state of any matter. The effect of change in these variables is reflected in the form of modification in intermolecular or/and intramolecular potentials in materials leading to many novel and unexpected phase transitions, such as polymorphic transition, amorphization, electronic transitions such as valence transition, metallization and molecular dissociation. Macroscopically, variation in pressure and temperature is manifested in the form of volume change when either of them is kept constant.

1.2.1 Pressure effect

From a microscopic perspective it may be stated that pressure directly affects the equilibrium spacing of nuclei, distorts the electron clouds and modifies the restoring force, *i.e.*, crystal potential. Thermodynamic expression for the change in energy as a result of applied pressure at constant volume and temperature can be expressed as

$$W = V\Delta P \tag{1.1}$$

where W, V and P is the work done, volume and pressure respectively. Application of pressure of the 100 GPa on solid leads to a change in free energy of 1 eV. This energy is sufficient to alter the bond lengths and the bond angles, which in turn govern the electronic and magnetic properties of solids. Application of pressure of a few GPa results in a volume change as high as 50% or more in case of soft solids like hydrogen [65]. Thus Pressure can induce myriad changes in the electronic properties of material as dicussed in the following subsection.

1.2.1.1 Hybridization

Pressure can drastically alter the nature of bonding, *i.e.*, π and σ bond, ionic and covalent nature of bonds *etc*. The hybridization of crystal orbitals is dramatically influenced by pressure. The sp^2 hybridization, which is fundamental in B, C and N, becomes unstable and is converted to sp^3 hybridization under pressure. For instance, in graphite, half of the π bonds (sp^2 hybridization) get converted into σ bond (sp^3 hybridization) above 17 GPa, resulting in a new phase of carbon. This new monoclinic phase of carbon is found to be superhard [66, 67]. The recent report of superhard amorphous diamond, with a near complete conversion of π to σ bond is another example of pressure effect on orbital hybridization [68, 69].

1.2.1.2 Hydrogen bond symmetrization

In the solid phase, each molecule of water (H_2O) is attached to other water molecules by forming a hydrogen bond between oxygen and hydrogen atom of different molecules. This open geometry of water molecule exhibits an unusually rich pressure–temperature phase diagram. Under pressure, the distance between donor (proton) and acceptor oxygen atoms reduces leading to degenerate single well proton potential, wherein hydrogen atom is located midway between two neighboring oxygen atoms, resulting in symmetrization of hydrogen bond. Infrared (IR), Raman, and X-ray measurements [70-72] have provided evidence for transition of ice VII phase to ice X phase having symmetric hydrogen bonds, when the distance between acceptor and donor oxygen atoms decreases below 2.3 Å, *i.e.,* 60 GPa pressure.

1.2.1.3 Reactivity

Pressure alters the reactivity and chemical affinity by bringing about changes in ionic radii, electronic structure and bonding characters. Notable examples of reactivity change under pressure are Van der Waal's compounds formed by inert gas 'argon' with hydrogen [73], which is stable up to 358 GPa, and other inert gas compounds formed by xenon with hydrogen [27], fluorine [74] and oxygen [75]. Similarly, noble metals no longer remain noble but form nitrides [76], when laser heated with molecular nitrogen under pressure. The reverse effect of pressure on reactivity is also true *e.g.,* reactive molecules like H_2 and O_2 become inert with respect to each other and coexist in same crystal [77] under pressure.

1.2.1.4 Electronic configuration

The energy of *s, p, d* and *f* orbitals varies differently under compression. It is also known that orbital with high angular momentum is favored at higher compressions thus leading to *s* to *p* and *s* to *d* transitions. For instance, the synthesis of KAg_2 under pressure is made possible by the transition of electron from *s* to *d* orbital in potassium [78].

1.2.1.5 Electronegativity

Electronegativity determines the distribution of bonding electrons between two atoms [79]. It is a quantitative measure of the effectiveness of nuclear charge as sensed within an outer orbital vacancy. Application of pressure leads to a change in effective electronic configuration, which in turn results in a change in electronegativity of atoms thus leading to different oxidation states. Recent experimental and theoretical studies have reported the stabilization of higher oxidation states of xenon (Xe^0 – Xe^2 – Xe^4 – Xe^6) under pressure [75, 80]. Higher oxidation states have also been predicted for cesium in cesium polyfluoride compounds under compression [81, 82]. It is also predicted that at high pressures, cesium, which has the least electronegativity at ambient condition, could become *p*-block element and form compounds with fluorine, which has the highest electronegativity.

1.2.1.6 Chemical hardness

Chemical hardness is defined as resistance of an atom to change its electronic configuration [83]. Pressure affects the spatial distribution of electrons, which result in change in the kinetic and potential energies and enthalpy of atoms thus leading to a change in chemical hardness of atoms. Theoretically calculated trend in chemical hardness with pressure for selected elements is shown in Fig. 1.3 [84].

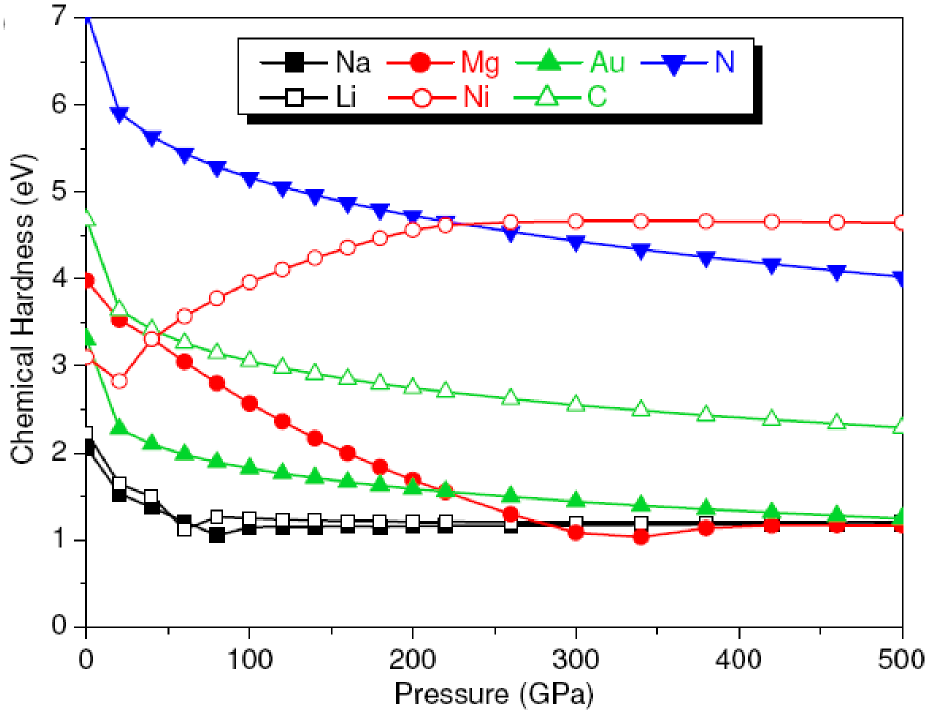

Fig. 1.3: *Pressure variation of chemical hardness in sodium (Na), Magnesium (Mg), Gold (Au), Lithium (Li), Nickel (Ni), Carbon (C), and Nitrogen (N) [84].*

1.2.1.7 Coordination

Pressure induced coordination change have been reported in liquids, solids and amorphous/glasses. For instance, Liquid fayalite exhibits an average Fe–O coordination number (CN) of 4.8 at ambient pressure which arises from the co-existence of approximately 60% FeO_4 and 40% FeO_6 units [85]. With increasing pressure up to 7.5 GPa, the average Fe–O CN increases to 7.2 [86]. The CN change from 8 to 10 for platinum and 4 to 5 for indium in intermetallic compound $PtIn_2$ during CaF_2 type to Fe_2B type structural phase transition, is an example of pressure induced change of coordination in solids [87].

1.2.2 Temperature effect

The primary effect of temperature is to induce diffusion and reduce kinetic barriers in solids. Temperature also affects the population of different vibrational levels of each normal mode, *i.e.,* it induces high energy phonons in crystals. Non-equidistant energy of these vibrational levels leads to a change in equilibrium distances between atoms [88]. It is noteworthy that the volume change ($\Delta V/V_0$) observed from ambient temperature to the melting of solid is typically ~ 6%.

According to Debye model, the thermal energy of a solid due to change in temperature is given by

$$E_{th} = \frac{9nRT}{\left(\theta_D/T\right)^3} \int_0^{\theta_D/T} \frac{\xi^3}{e^{\xi} - 1} d\xi \tag{1.2}$$

where E_{th}, n, R, θ_D and ξ are thermal vibrational energy, number of atoms per formula unit, gas constant, Debye temperature and ($\hbar\omega/kT$) respectively. The change in free energy of solids due to temperature variation of 10^4 K is 1 eV, which is orders of magnitude smaller than the energy associated with pressure variation [89].

1.3 High Pressure High Temperature (HPHT) Techniques

Pressure and temperature both lead to change in lattice parameters of materials. However, pressure and temperature complement each other owing to the different microscopic mechanism by which they alter the lattice parameters. In this sense the field of HPHT research opens up novel phases in materials, enabling one to obtain P-V-T equation of state (EOS) and investigate the phase diagram of important materials including their phase transitions and phase stability.

The available HPHT devices can be broadly classified into two major types *viz.*, static compression and dynamic compression based techiques. In the case of static compression techniques, the time required to apply pressure is much longer than time required by the system to reach thermal equilibrium. Hence all static compression methods are isothermal and require external heating source to increase the sample temperature. In the case of dynamic pressure studies, HPHT is achieved by shock compression using an explosive, laser or a projectile. The following subsection gives a brief review of available HPHT techniques elucidating their capabilities and limitations.

1.3.1 Static high pressure technique for HPHT research

The static compression techniques can be divided into large volume apparatus and diamond anvil cell based techniques, which are briefly described in the following subsection.

1.3.1.1 Large volume apparatus

The major large volume techniques for generation of HPHT are the piston-cylinder, Bridgman anvil apparatus, belt apparatus, Toroidal anvil, Paris–Edinburg cell and Multi-anvil apparatus (MAA). As the name suggests, the sample volume subjected to HPHT in large volume apparatus, ranges from few cm^3 to mm^3 [90]. The principal advantage of large volume apparatus is the retrieval of a relatively large quantity of sample (volume of the order of mm^3) for post experimental analysis.

The piston-cylinder is the simplest of all the high pressure devices. Figure 1.4 shows a schematic of cross-sectional view of a piston cylinder press. The sample pressure is generated by moving the master ram upwards using a hydraulic press. In order to keep the whole system in equilibrium and prevent deformation, one should apply pressure also from the top in the end loaded type piston-cylinder apparatus. In non end-loaded apparatus, the mechanism to apply pressure from the top is absent and hence it cannot be used to very high pressures. Pressure and temperature range achieved in piston-cylinder apparatus is around 4 GPa and 2000 K [91]. It is noteworthy that piston-cylinder is the only device which is capable of generation of hydrostatic pressure.

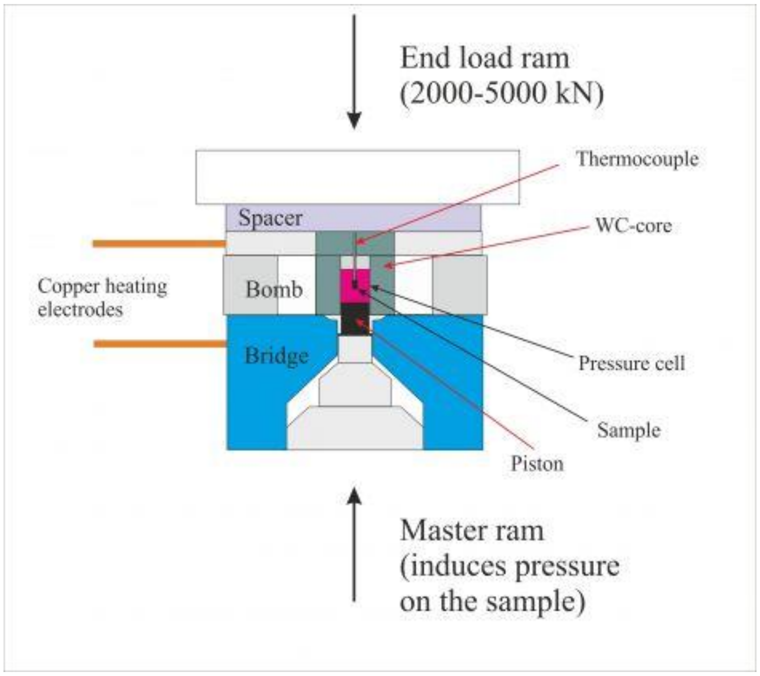

Fig. 1.4: *Schematic of cross-sectional view of a piston cylinder press [92]*

All the other large volume apparatus are opposed anvil high pressure devices working on the principle of massive support which states that if high pressure is generated on a small area of a much larger body, it can support two or three times the compressive yield stress because of its attachment to the surrounding material. Figure 1.5 shows a schematic of a tungsten carbide (WC) anvil based Bridgman anvil apparatus capable of achieving a pressure up to 10 GPa. The use of sintered diamond increases the pressure limit to 20.5 GPa [93]. A maximum temperature of 1400 K, using graphite disc heater, has been achieved in Bridgman anvil apparatus [93].

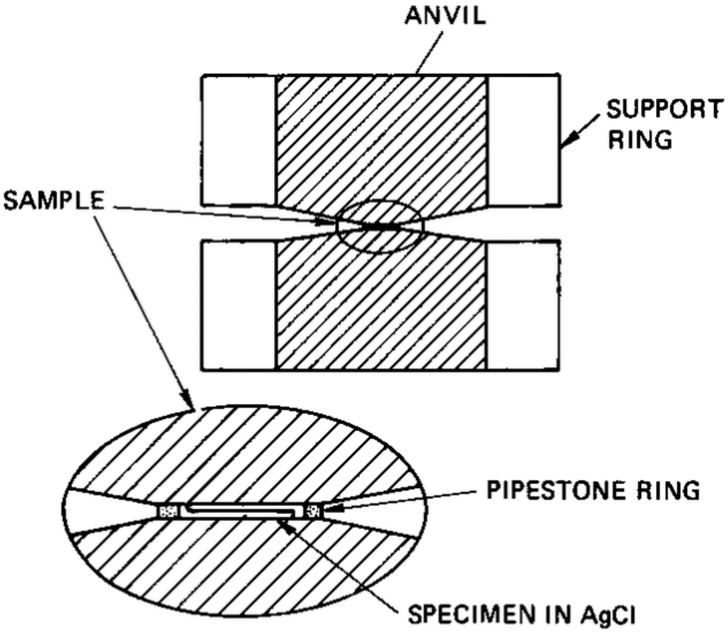

Fig. 1.5: *Schematic of Bridgman anvil apparatus [94]*

The belt apparatus (Fig. 1.6a) is another HPHT device capable of generating higher pressure compared to piston-cylinder. This apparatus has two opposed anvils and a belt-type die, that consist of a cylinder and several supporting rings, as shown in Fig. 1.6b. The belt-type die made up of tungsten carbide limits the pressure bearing capacity of the belt apparatus. Recently, a novel high pressure belt-type die with a split cylinder has been developed to increase pressure bearing capability of the belt apparatus [95]. Typical pressures and temperatures achieved using the belt apparatus is ~10 GPa and ~1700 K [96].

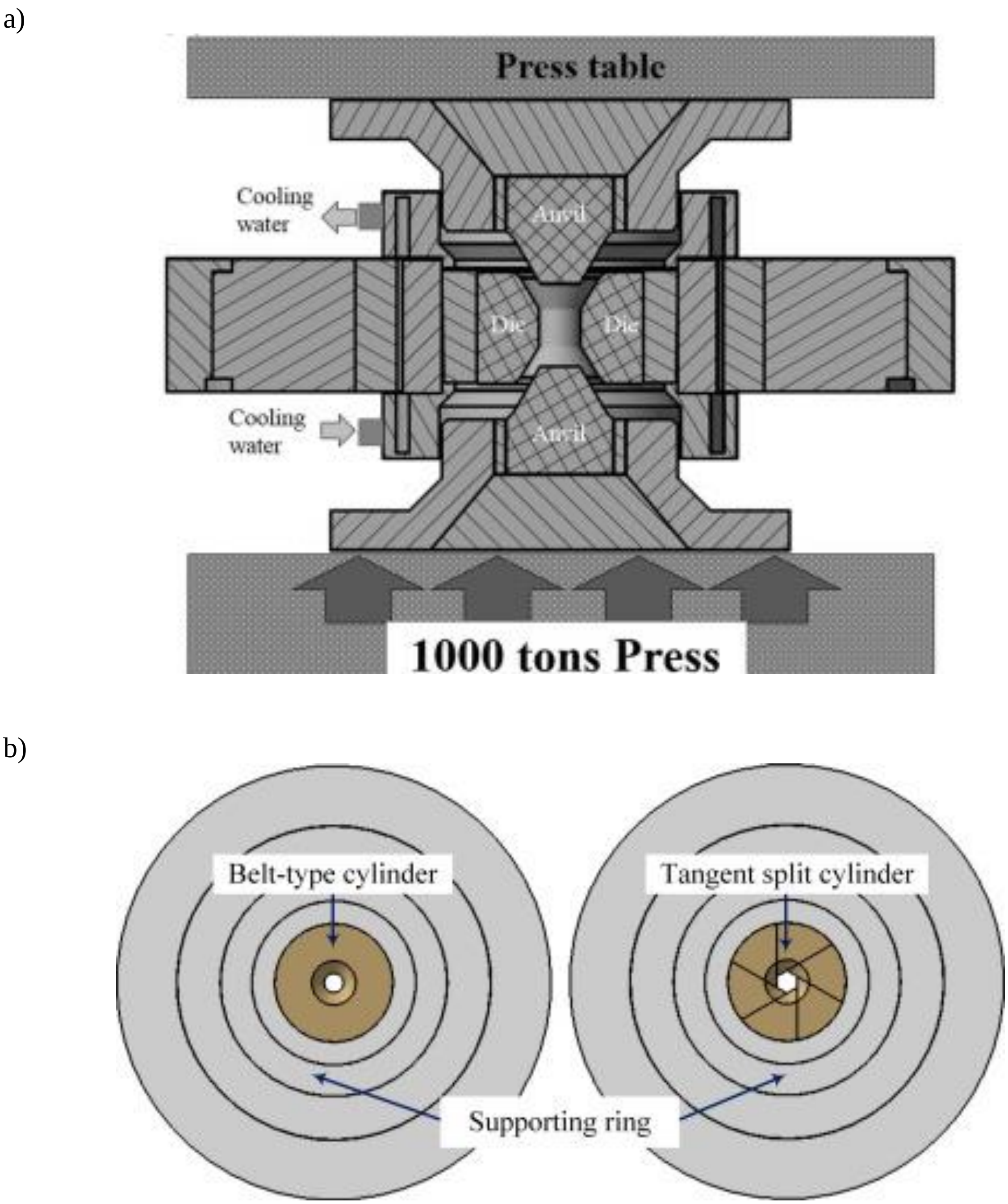

Fig. 1.6: *a) Belt apparatus assembly [97] and b) schematic of belt-type and split cylinder [98].*

Toroidal anvil, developed by USSR physicist L. G. Khvostantsev in 1969, pushed the pressure and temperature limits to ~16 GPa and 2500 K [99, 100]. As shown in Fig. 1.7, the sample in toroidal anvil apparatus is encapsulated in BN or alumina cylinder, which serves as the sample crucible. This crucible is surrounded by graphite cylinder and graphite caps, which act as a heater when electrical current is passed through it and raises the sample temperature. This assembly is then placed at the central hole of toroidal shaped pyrophyllite gasket. High pressure is generated by applying load to the gasket placed between two toroidal shaped anvils using a hydraulic press. Toroidal anvil apparatus is one of the preferred choice for chemical synthesis, single crystal synthesis, electrical resistance measurements, Hall resistance measurements and equation of state studies [100-102]. The high pressure capability of toroidal anvil apparatus is limited by the WC anvils. The use of synthetic polycrystalline diamond in toroidal anvil has however enabled a pressure ~35 GPa to be achieved [100].

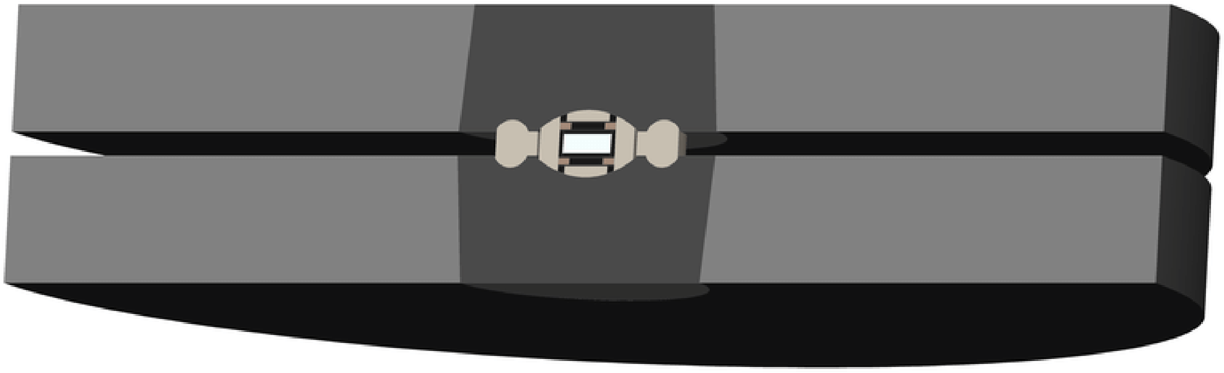

Fig. 1.7: *Cross-sectional view of toroidal anvils with pyrophyllite gasket at the middle [103].*

Paris–Edinburgh press (PEP) is another large volume apparatus capable of generating a maximum pressure and temperature of 11 GPa and 1800 K respectively. Figure 1.8a shows a typical gasket assembly used for PEP experiments. Pressure is generated by applying load to the sample assembly using a hydraulic press as shown in Fig. 1.8b. The use of sintered diamond in PEP has further increased the pressure limit up to 16.5 GPa [104]. The main advantage of Paris–Edinburgh press is that it can be coupled with synchrotron based XRD and neutron diffraction measurements [104].

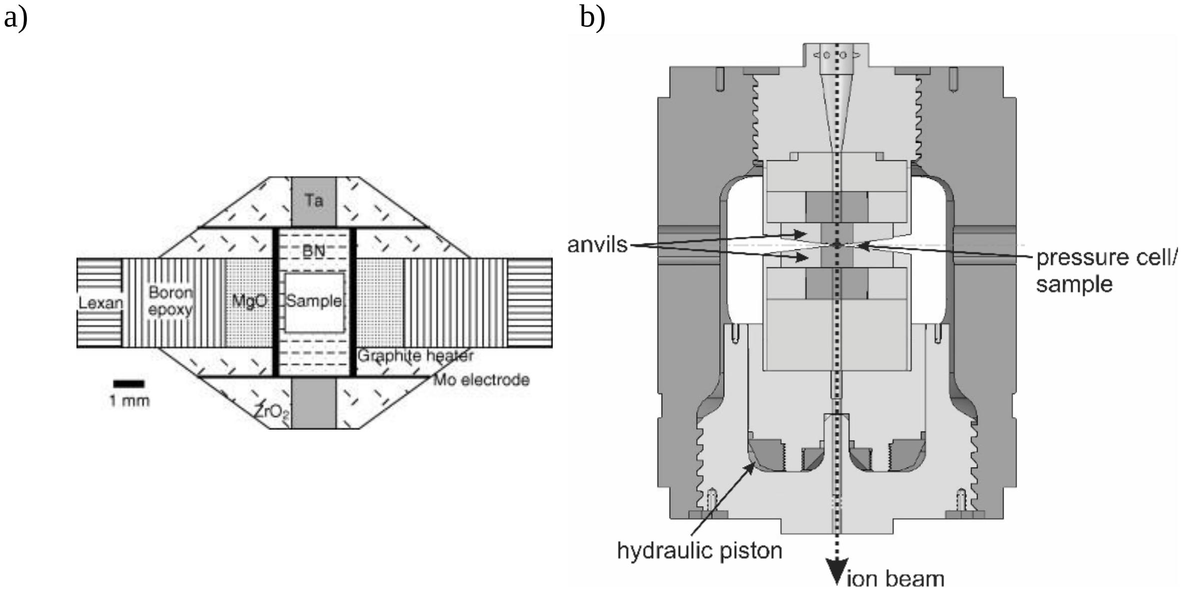

Fig. 1.8: *a) Cross section of gasket assembly used in Paris–Edinburgh press [105]. b) Schematic diagram of Paris–Edinburgh press [106].*

In recent times multianvil apparatus has emerged as a popular large volume device for HPHT studies. Multi-anvil (MAA) as shown in Fig. 1.9 can be defined as a high pressure apparatus with more than one axis of loading with four or more anvils compressing the sample. The first multi-anvil device with a tetrahedral anvils geometry, generated pressure of 10 GPa and temperature in access of 3000 K [107]. In the past decade, the pressure limit of MAA has been raised to 27 GPa [108]. It has been reported that MAA can generate pressures up to 1 Mbar using nano-polycrystalline diamonds in conjunction with WC anvils [109]. The MAA, coupled with *in situ* X-ray diffraction techniques, has proven to be ideal for HPHT structural studies in Earth and planetary research [107].

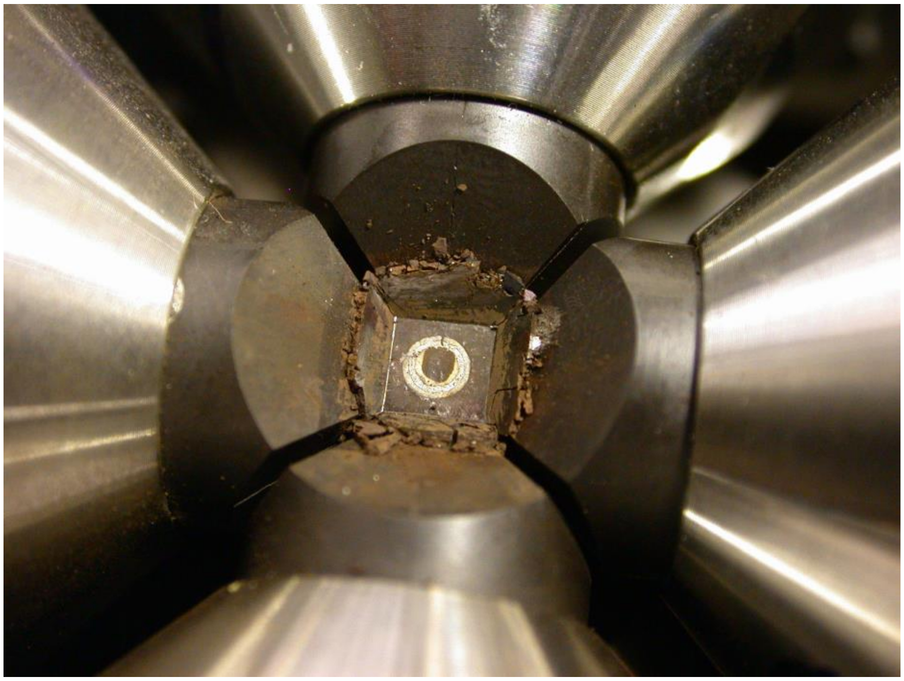

Fig. 1.9: *Photograph of MAA with sample assembly of recovered sample [110].*

1.3.1.2 Diamond anvil cell (DAC) based HPHT techniques

The DAC is a device par excellence, which exploits the remarkable properties of diamonds, such as high hardness and optical transparency to a wide range of electromagnetic spectrum. It is noteworthy that DAC also enables an *in-situ* visual observation of the pressurized sample. The additional advantage of DAC is that it can be easily integrated with a variety of diagnostics like X-ray diffraction, Raman, Brillouin and synchrotron based micro-probing techniques giving it an edge over large volume apparatus for materials research. In recent times, the highest static pressure of 1.0 TPa has been achieved using a novel two stage DAC [111]. The development of DAC has reduced the size of high pressure device substantially thus facilitating easy transportation. The alternative anvil material used for high pressure experiments are moissanite (SiC) [112], cubic Zirconia (ZrO_2) [113] and Sapphire (Al_2O_3) [114, 115]. Table 1.2 summarizes the maximum pressure achieved with different anvil materials in comparison to diamond.

Table 1.2: Comparison of maximum pressure achieved with different anvil materials.

Anvil material	Diamond [111]	SiC [112]	Al_2O_3 [114,115]	ZrO_2 [113]
Maximum Pressure (GPa)	1065	59	26	17

The DAC also offers a powerful and versatile means of investigating the properties of materials at sustained high temperatures and pressures by two techniques *viz.*, resistive heating and laser heating. Resistive heating in a DAC can be carried out by either internal heating or external heating. In external heating method, a coil heater surrounding the anvils or a band heater around DAC is used [116]. The maximum temperature attained by this technique is limited to 1300 K owing to graphitization and oxidation of the diamond anvils above this temperature as well as mechanical instability of different parts of the DAC at elevated temperatures [116]. The principle advantage of the DAC based resistive heating technique is the nearly uniform sample temperature and the ease of sample temperature measurement using thermocouple while the main disadvantage is the existence of large pressure inhomogeneity (gradient) across the sample. The temperature limitation of external heating technique can be partially overcome by internal resistively heated DAC technique. In this case, the electrical current is passed through the sample itself and the temperature is measured by an optical pyrometer. The main limitation of this technique is however the requirement of a metallic sample and the pressure gradient induced deformation and failure of heating circuit at very high pressures. A maximum sample temperature up to 3000K has been achieved by this technique [117]. The development of designer diamond anvils overcomes this problem. In these anvils, the heating elements and the measuring probes are fabricated on the culets by lithographic fabrication. These have been tested up to 21 GPa and 2000K [118].

In recent times, laser heated diamond anvil cell (LHDAC) technique has emerged as a valuable and versatile tool for achieving high pressures ($P > 100$ GPa) and temperatures ($T \sim 6000$K) thus providing a unique opportunity to investigate material properties at these extreme conditions. The optical transparency of diamond in the infrared (IR) region allows the use of continuous wave (CW) near infrared (NIR) lasers such as neodymium doped yttrium aluminium garnet ($Nd^{3+:}$YAG), neodymium doped yttrium lithium fluoride ($Nd^{3+:}$YLF), ytterbium (Yb) doped fibre laser or MIR CO_2 laser, the choice being driven by sample absorptivity. Advancement in laser technology have made IR lasers more compact, stable (in terms of power as well as pointing stability) and a maximum power reaching over more than 200 W . This has facilitated a myriad of HPHT *in-situ* diagnostic techniques like Raman and Brillouin spectroscopy, x-ray diffraction, x-ray absorption fine structure (XAFS), electrical transport, NMR *etc* [119- 127]. A detailed discussion on LHDAC is presented in **Chapter 2** of this thesis.

Materials subjected to HPHT conditions in LHDAC experiments with IR laser in the CW mode are vulnerable to chemical reaction with surroundings, *i.e.*, pressure transmitting medium, pressure calibrant, diamond *etc*. Very recently, DAC based pulsed laser heating technique has been developed to address these problems. The short heating duration, ~ μs, in pulsed laser heating helps in suppressing thermally activated chemical diffusion and reaction. In addition, it enables one to achieve higher sample temperature compared to CW laser heating; as the same energy is delivered in much shorter period of time. This technique is useful for time resolved measurements [128]. For instance, XRD measurements could be made possible, during pulsed laser heating, when coupled with synchrotron x-ray sources having time resolved high brilliance x-ray pulses of the order of femtosecond to nanosecond [128]. The measurement of the peak sample temperature in case of pulsed laser heating however necessitates more complex electronics.

1.3.2 Dynamic high pressure technique for HPHT measurements

In dynamic method, HPHT is achieved by launching a dynamic compression wave or shock wave in the material. Shock is defined as a discontinuity in thermodynamic variables, which propagates with supersonic velocity with respect to the material ahead of it and with subsonic velocity with respect to the material behind it. A pressure wave which travels with a speed higher than the system response time generates a shock in the system. Shock experiment is an irreversible adiabatic process since the material does not have enough time to achieve thermal equilibrium with the surrounding. Dynamic pressures are normally created by depositing high energy densities over small time durations on the target materials by impacting with a flyer plate moving at high velocity, or by a rapid deposition of energy using explosives [129], lasers [130], particle beams *etc.,* [131]. The shock experiment enables one to achieve extremely high pressures of the order of TPa in the laboratory. During shock experiment, the system jumps from one thermodynamic state to another thermodynamic state. Also, since the increase in temperature is as a result of adiabatic process during shock compression, it does not necessarily require any external heating mechanism to generate HPHT condition, which limits the independent control over final pressure and temperature. The time duration involved in shock compression however demands ultrafast diagnostic techniques. The sample characterization is also much more involved and limited to fewer probes as compared to static high pressure techniques.

Recently, a new approach combining static and dynamic compression techniques has been reported wherein strong shockwave is launched in precompressed samples. This allows one to explore extreme conditions of matter, such as molecular fluid to the plasma state transition and the superionic states of molecular solids [132]. This technique is quite promising since a few GPa precompression can induce significant density increase in compressible fluids. The locus of shock states (Hugoniot) accessible by the subsequent multiple shock compressions with same precompressed state or series of shock compressions are reached at moderately lower temperatures (~10^3-10^4 K) and higher densities (~ few Mbar), which is the advantageous over conventional laser shock experiments, for planetary studies [89].

1.4 Review of Diagnostic Techniques Coupled to LHDAC

Diamond is transparent to a wide electromagnetic spectrum ranging from hard x-rays to far IR. The use of diamond anvil in LHDAC thus enables the integration of many diagnostic techniques for *in situ* investigation of materials at extreme conditions. Synchrotron based

ADXRD measurements are the most widely used diagnostic technique coupled to LHDAC. Nearly all leading synchrotron facilities across the world, like PETRA III, APS, Spring8, ESRF *etc.,* have a dedicated beamline for LHDAC based ADXRD measurements for HPHT structural and material synthesis studies [119, 120]. In addition, it also enables determination of the phase diagram and high pressure melting curve of important materials.

Another popular diagnostic technique coupled to LHDAC is Raman spectroscopy, which provides molecular and vibrational information of materials at HPHT conditions. For *e.g.,* HPHT Raman study of CO_2 has been reported up to 65 GPa and 1600 K for its obvious importance in planetary studies [121]. Similarly, N_2 has been studied up to 120 GPa and 2500K using LHDAC based Raman spectroscopy and a maxima in melting line at ~ 70 GPa has been observed [122].

LHDAC based Brillouin spectroscopy is an ideal technique for the study of elastic properties of materials at HPHT condition. Recently this technique has been used to study elastic properties of single crystal olivine up to 13 GPa and 1300K [123] and water – ice (H_2O) system up to 2500 K and several GPa pressure [123].

Resistivity measurement has also been recently coupled to LHDAC to study the melting curve of Fe up to 1 Mbar and 3200K [124]. In this technique, sample in the form of wires, were heated with an ytterbium fiber laser (λ = 1070 nm, TEM_{00} mode, CW). The change in the electrical resistance of the sample wire is measured by the two-terminal method using sourcemeter under a constant DC current [124].

Iron is one of the most important geophysical material and the accuracy of high pressure melting curve of Fe with different melting criteria is still debatable. Recently, the melting line of Fe has been reported up to 103 GPa by integrating synchrotron based XAS to LHDAC [125].

Similarly, synchrotron-based X-ray emission spectroscopy (XES) is well suited to probe the local electronic structure of 3*d* transition metals such as Fe and Mn in their host phases. Laser heated XES experiment on the crystal, magnesiowustite ($Mg_{0.75}Fe_{0.25}$)O, has been carried out to study the spin state of ferrous iron up to 47 GPa and 1300 K [126].

Other spectroscopic techniques which have been successfully coupled to LHDAC are nuclear resonant inelastic X-ray scattering and synchrotron based Mossbauer spectroscopy [127]. HPHT studies up to 100 GPa and 2500 K on iron containing minerals have been reported using these methods [127].

1.5 Organization of the Present Thesis

The present thesis is organized in to six chapters. The introductory **Chapter 1** gives a brief overview and some recent development in the area of HPHT research followed by a summary of the various available HPHT techniques highlighting the importance of LHDAC. The design aspect and setting up of a Yb fibre laser based LHDAC facility forms the instrumentation part of the thesis. The details of development of this facility and its successful application for carrying out high pressure melting and HPHT synthesis experiments are described in **Chapter 2.** The LHDAC facility has been employed for experimental determination of melting curve, up to 35 GPa, of elemental osmium, which has some remarkable properties like highest density among elements and a bulk modulus that is almost comparable to that of diamond under ambient temperature and pressure conditions. The details of the study are described in **Chapter 3**. The synthesis of counterintuitive compounds in K-Br system *viz.,* KBr_3 and KBr_5 at HPHT and their ambient temperature high pressure study *i.e.,* stoichiometry, crystal structure, vibrational properties and theoretical calculation of bonding and electronic band structure have been described in **Chapter 4**. Recent reports on the synthesis of alkali trihalide compounds in Na-Cl, K-Br and K-Cl at extreme conditions have rekindled the interest in this new class of compounds with unknown chemical and physical properties. Furthermore, the advent of bright synchrotron source has made it possible to carry out high pressure ADXRD measurements with greater resolution, accuracy and precision. **Chapter 5** of this thesis describes the results of high pressure structural, vibrational and transport measurements on the alkai trihalide "CsI_3". A brief summary of the research work discussed in this thesis and some future extension of the present work are highlighted in **Chapter 6.**

References:

[1] B. Gutenberg, *Physikalische Zeitschrift* ,**14,** 1217 (1913).

[2] B. Gutenberg, Ueber Erdbebenwellen. VII A. Beobachtungen an Registrierungen von Fernbeben in Göttingen und Folgerungen über die Konstitution des Erdkörpers. Nachrichten von der Königlichen Gesellschaft der Wissenschaften zu Göttingen. *Mathematisch-physikalische Klasse*, 125-177 (1914).

[3] A. M. Dziewonski and D. L. Anderson, *Phys. Earth Planet. Inter.*, **25**, 297 (1981).

[4] D. C. Rubie , D. J. Frost, U. Mann, Y. Asahara, F. Nimmo, K. Tsuno, P. Kegler, A. Holzheid and H. Palme, *Earth Planet. Sci. Lett.* **301**, 31 (2011).

[5] D. Gubbins, B. Sreenivasan, J. Mound and S. Rost, *Nature* **473**, 361(2011).

[6] A. Biastoch, T. Treude, L. H. Rüpke, U. Riebesell, C. Roth, E. B. Burwicz, W. Park, M. Latif, C. W. Böning, G. Madec and K. Wallmann, Geophys. Res. Lett. **38**, L08602 (2011).

[7] C. D. Ruppel, *Nature Education Knowledge*, **3,** 29 (2011).

[8] S.W.H. Cowley and E.J. Bunce, *Planetary and Space Science*, **49**,1067 (2001).

[9] R. Smoluchowski, *The Astrophysical Journal*, **200**, L119 (1975).

[10] Bolton et al., *Science* **356**, 821 (2017).

[11] https://www.tes.com/lessons/tg5Pp-QE-JVZwQ/jupiter

[12] N.W. Ashcroft, *Phys. Rev. Lett.* **21**, 1748 (1968).

[13] N.W. Ashcroft, *Phys. Rev. Lett.* **92**, 187002 (2004).

[14] Z. M. Geballe, H. Liu, A. K. Mishra, M. Ahart, M. Somayazulu, Y. Meng, M. Baldini and R. J. Hemley, *Angew. Chem. Int. Ed.* **57**, 688 (2018).

[15] R. P. Dias and I. F. Silvera, *Science* **355**, 715 (2017).

[16] A. P. Drozdov, M. I. Eremets, I. A. Troyan, V. Ksenofontov and S. I. Shylin, *Nature* **525**, 73 (2015).

[17] V. V. Struzhkin, D. Y. Kim, E. Stavrou, T. Muramatsu, H. K. Mao, C. J. Pickard, R. J. Needs, V. B. Prakapenka and A. F. Goncharov, *Nature Comm.* **7**, 12267 (2016).

[18] X. Feng, J. Zhang, G. Gao, H. Liu and H. Wang, *RSC Adv.* **5**, 59292 (2015).

[19] H. Wang, J. S. Tse, K. Tanaka, T. Iitaka and Y. Ma, *Proc.Natl. Acad. Sci.* **109**, 6463 (2012).

[20] P. Baettig and E. Zurek, *Phys. Rev. Latt.* **106**, 237002 (2011).

[21] M. I. Eremets, K. Shimizu, T. C. Kobayashi and K. Amaya, *Science* **281**, 1333 (1998).

[22] Y. Xu, J. S. Tse, A. R. Oganov, T. Cui, H. Wang, Y. Ma and G. Zuo, *Phys. Rev. B* **79**, 144110 (2009).

[23] M. I. Eremets, K. Shimizu, T. C. Kobayashi and K. Amaya, *J. Phys.: Condens. Matter* **10,** 11519 (1998).

[24] W. Zhang, A. R. Oganov, A. F. Goncharov, Q. Zhu, S. E.Boulfelfel, A. O. Lyakhov, E. Stavrou, M. Somayazulu, V. B. Prakapenka and Z. Konopkova, *Science,* **342**, 1502 (2013).

[25] Q. Zhu, A. R. Oganov and A. O. Lyaknov, *Phys. Chem. Chem. Phys.***15**, 7696 (2013).

[26] H. Niu, A. R. Oganov, X. Q. Chen and D. Li, *Sci. Rep.* **5**, 18347 (2015).

[27] M. Somayazulu, P. Dera, A. F. Goncharov, S. A. Gramsch, P. Liermann, W. Yang, Z. Liu, H. K. Mao and R. J. Hemley, *Nat. Chem.* **2**, 50 (2010).

[28] Z. Zeng, L. Yang, Q. Zeng, H. Lou, H. Sheng, J. Wen, D. J. Miller, Y. Meng, W. Yang, W. L. Mao and H. K. Mao, *Nat. Commun.* **8**, 322 (2017).

[29] G. Demazeau, *Diamond and Related Materials* **4,** 284 (1995).

[30] O. O. Kurakevych, *J. Superhard Mater.* **31**, 139 (2009).

[31] A. Friedrich, B. Winkler, E. A. Juarez-Arellano and L. Bayarjargal, *Materials*, **4**, 648 (2011).

[32] H.O. Pierson, *Handbook of Refractory Carbides and Nitrides*; Noyes Publication: Park Ridge, UT, USA, (1996).

[33] A. F. Young, C. Sanloup, E. Gregoryanz, S. Scandolo, R. J. Hemley and H. K. Mao, *Phys. Rev. Lett.*, **96**, 155501:1 (2006).

[34] K. Niwa, D. Dzivenko, K. Suzuki, R. Riedel, I. Troyan, M. I. Eremets and M. Hasegawa, *Inorg. Chem.*, **53**, 697 (2014).

[35] K. Niwa, K. Suzuki, S. Muto, K. Tatsumi, K. Soda, T. Kikegawa and M. Hasegawa, *Chem. Eur. J.*, **20**, 13885 (2014).

[36] E. Gregoryanz, C. Sanloup, M. Somayazulu, J. Badro, G. Fiquet, H. K. Mao and R. J. Hemley, *Nat. Mater.*, **3**, 294 (2004).

[37] S. J. Sedlmaier, M. Eberspächer and W. Schnick, *Z. Anorg. Allg. Chem.*, **637**, 362 (2011).

[38] Q. Yang, W. Lengauer, T. Koch, M. Scheerer and I. Smid, *J. Alloy. Compd.*, **309,** L5 (2000).

[39] O. Shebanova, E. Soignard and P. F. McMillan, *High Pressure Res.*, **26**, 87 (2006).

[40] H. Chen, F. Peng, H. K. Mao, G. Shen, H. P. Liermann, Z. Li and J. Shu, *J. Appl. Phys.*, **107**, 113503:1 (2010).

[41] J. Musil, *Surf. Coat. Tech.*, **125**, 322 (2000).

[42] V. S. Bhadram, D. Y. Kim and T. A. Strobel, *Chem. Mater.*, **28**, 1616 (2016).

[43] X. J. Chen, V. V. Struzhkin, Z. Wu, M. Somayazulu, J. Qian, S. Kung, A. N. Christensen, Y. Zhao, R. E. Cohen, H. K. Mao and R. J. Hemley, *Proc. Natl. Acad. Sci.*, **102**, 3198 (2005).

[44] D. A. Dzivenko, A. Zerr, E. Schweitzer, M. Goken, R. Boehler and R. Riedel, *Appl. Phys. Lett.*, **90**, 191910:1 (2007).

[45] A. Zerr, N. Chigarev, R. Brenner, D. A. Dzivenko and V. Gusev, *Phys. Status Solidi-r*, **4**, 353 (2010).

[46] D. A. Dzivenko, A. Zerr, R. Boehler and R. Riedel, *Solid State Commun.*, **139**, 255 (2006).

[47] M. Mattesini, R. Ahuja and B. Johansson, *Phys. Rev. B*, **68**, 184108:1 (2003).

[48] F. Rivadulla, M. Banobre-Lopez, C. X. Quintela, A. Pineiro, V. Pardo, D. Baldomir, M. A. Lopez-Quintela, J. Rivas, C. A. Ramos, H. Salva, J. S. Zhou and J. B. Goodenough, *Nat. Mater.*, **8**, 947 (2009).

[49] K. E. Davies, B. K. Gan, D. R. McKenzie, M. M. M. Bilek, M. B. Taylor, D. G. McCulloch and B. A. Latella, *J. Phys.-Condens. Mat.*, **16**, 7947 (2004).

[50] W. W. Lei, D. Liu, X. F. Li, J. Zhang, Q. Zhou, Q. L. Cui and G. T. Zou, *J. Phys. Condens. Mat.*, **19**, 425233:1 (2007).

[51] E. Soignard, O. Shebanova and P. F. McMillan, *Phys. Rev. B*, **75**, 014104:1 (2007).

[52] A. Friedrich, B. Winkler, L Bayarjargal, E. A. Juarez-Arellano, W. Morgenroth, J. Biehler, F. Schroder, J. Yan and S. M. Clark, *J. Alloy Compd.*, **502**, 5 (2010).

[53] A. Zerr, G. Miehe, J. Li, D. A. Dzivenko, V. K. Bulatov, H. Hofer, N. B. Casanova, M. Fialin, G. Brey, T. Watanabe and M. Yoshimura, *Adv. Funct. Mater.*, **19**, 2282 (2009).

[54] M. Urgen, O. L. Eryilmaz, A. F. Cakir, E. S. Kayali, B. Nilufer and Y. Isik, *Surf. Coat. Tech.*, **94–95**, 501 (1997).

[55] E. Soignard, P.F. McMillan, T. D. Chaplin, S. M. Farag, C. L. Bull, M. Somayazulu and K. Leinenweber, *Phys. Rev. B*, **68**, 132101:1 (2003).

[56] A. Friedrich, B. Winkler, L. Bayarjargal, W. Morgenroth, E. A. Juarez-Arellano, V.Milman, K. Refson, M. Kunz and K. Chen, *Phys. Rev. Lett.*, **105**, 085504:1 (2010).

[57] J. F. Adler and Q. Williams, *J. Geophys. Res.*, **110**, B01203:1 (2005).

[58] R. Niewa, D. Rau, A. Wosylus, K. Meier, M. Hanfland, M. Wessel, R. Dronskowski, D. A. Dzivenko, R. Riedel and U. Schwarz, *Chem. Mater.*, **21**, 392 (2009).

[59] H. Xia, Q. Xia, and A. L. Ruoff, *Phys. Rev. B* **47**, 12925 (1993).

[60] E. Gregoryanz, O. Degtyareva, M. Somayazulu, R. J. Hemley and H. K. Mao, *Phys. Rev. Lett.* **94**, 185502 (2005).

[61] C. L. Guillaume, E. Gregoryanz, O. Degtyareva, M. I. McMahon, S. Evans, M. Hanfland, M. Guthrie, S. V. Sinogeikin and H. K. Mao, *Nat. Phys.* **7**, 211(2011).

[62] R. Hrubiak, Y. Meng and G. Shen, *Nat. Comm.* **8**, 14562 (2017).

[63] F. D. Stacey and R. D. Irvine, *Aust. J. Phys.* **30**, 631 (1977).

[64] V.V. Kechin, *Phys. Rev. B* **65,** 052102 (2001).

[65] H. K. Mao and R. J. Hemley, *Rev. Mod. Phys.* **66**, 671 (1994).

[66] W. L. Mao, H. K. Mao, P. Eng, T. Trainor, M. Newville, C. C. Kao, D. L. Heinz, J. Shu, Y. Meng and R. J. Hemley, *Science* **302**,425 (2003).

[67] Q. Li, Y. Ma, A. R. Oganov, H.Wang, H.Wang, Y. Xu, T. Cui, H. K. Mao and G. Zou, *Phys. Rev. Lett.* **102**, 175506 (2009).

[68] Y. Lin, L. Zhang, H.-k. Mao, P. Chow, Y. Xiao, M. Baldini, J. Shu and W. L. Mao, *Phys. Rev. Lett.* **107**, 175504 (2011).

[69] H. Niu, X. Q. Chen, S. Wang, D. Li, W. L. Mao and Y. Li, *Phys. Rev. Lett.* **108**, 135501 (2012).

[70] E. Sugimura, T. Iitaka, K. Hirose, K. Kawamura, N. Sata and Y. Ohishi, *Phys. Rev. B* **77**, 214103 (2008).

[71] A. F. Goncharov, V. V. Struzhkin, H. K. Mao and R. J. Hemley, *Phys. Rev. Lett.* **83,** 1998 (1999).

[72] K. Aoki, H. Yamawaki, M. Sakashita and H. Fujihisa, *Phys. Rev. B* **54,** 15673 (1996).

[73] C. Ji, A. F. Goncharov, V. Shukla, N. K. Jena, D. Popov, B. Li, J. Wang, Y. Meng, V. B. Prakapenka, J. S. Smith, R. Ahuja, W. Yang and H. K. Mao., *Proc. Natl. Acad. Sci.* **114**,3596 (2017).

[74] M. Kim, M. Debessai and C. S. Yoo, *Nat. Chem.* **2**, 784 (2010).

[75] A. Dewaele, N. Worth, C. J. Pickard, R. J. Needs, S. Pascarelli, O. Mathon, M. Mezouar and T. Irifune, *Nat. Chem.* **8**, 784 (2016).

[76] J. C. Crowhurst, A. F. Goncharov, B. Sadigh, C. L. Evans, P. G. Morrall, J. L. Ferreira and A. J. Nelson, *Science*, **311**, 1275 (2006).

[77] W. L. Mao, H. K. Mao, Y. Meng, P. Eng, M. Y. Hu, P. Chow, Y. Q. Cai, J. Shu and R. J. Hemley, *Science* **314**, 636 (2006).

[78] L.J. Parker, T. Atou and J.V. Badding, *Science* **273**, 95 (1996).

[79] R. T. Sanderson, *J. Chem. Edu.* **65**, 112 (1988).

[80] Q. Zhu, D. Y. Jung, A. R. Oganov, C. W. Glass, C. Gatti and A. O. Lyakhov, *Nat. Chem.* **5**, 61 (2013).

[81] M. S. Miao, *Nat. Chem*. **5**, 846 (2013).

[82] Q. Zhu, A. R. Oganov and Q. Zeng, *Sci. Rep*. **5**, 7875 (2015).

[83] G. Makov, *J. Phys. Chem.* **99**, 9337 (1995).

[84] X. Dong, A. R. Oganov, G. Qian, X. F. Zhou, Q. Zhu and H. T. Wang, *arXiv:1503.00230* [cond-mat.mtrl-sci].

[85] J. W. E. Drewitt, C. Sanloup, A. Bytchkov, S. Brassamin and L. Hennet, *Phys. Rev. B*, **87**, 224201 (2013).

[86] H. Spice, C. Sanloup, B. Cochain, C. de Grouchy and Y. Kono, *Geochimica et Cosmochimica Acta*, **148**, 219 (2015).

[87] P. Modak and A. K. Verma, *Inorg. Chem*. **56,** 14643 (2017).

[88] G. Lucazeau, *J. Raman Spectroscopy*, **34** , 478 (2003).

[89] R. Jeanloz, P. M. Celliers, G. W. Collins, J. H. Eggert, K. K. M. Lee, R. S. McWilliams, S. Brygoo and P. Loubeyre, *Proc. Nat. Acad. Sci.*, **104**, 9172 (2007).

[90] M. I. Eremets, *High Pressure Experimental Methods*, Oxford University Press UK (1999).

[91] M. Masotta, C. Freda, T. A. Paul, G. M. Moore, M. Gaeta, P. Scarlato and V. R. Troll, *Chem. Geol.* **312–313** 74 (2012).

[92] http://enikobali.hupont.hu/6/high-pressure-and-temperature-experiments-pressure

[93] M. Akaogi and T. Yamazaki, *Proc. Japan Acad.*, **67(B)**, 61 (1991).

[94] P.W. Bridgmann, *Proc. Am. Acad. Arts. Sci.*, **74**, 425 (1942).

[95] L. Zhao, M. Li, L. Wang, E. Qu and Z. Yi, *Rev. Sci. Instrum.* **89**, 035106 (2018).

[96] C. Venkateswaran, K. Anbukumaran, N. Victor Jaya and S. Natarajan, *Rev. Sci. instrum.* **68**, 189 (1997).

[97] F. Balima, F. Bellin, D. Michau, O. Viraphong, A. Poulon-Quintin, U. C. Chung, A. Dourfaye and A. Largeteau, *Materials and Design* **139** ,541 (2018).

[98] Y. Yang, M. Li and B. Wang, *Diamond & Related Materials* **58** , 180 (2015).

[99] L. G. Khvostantsev, *Report of the Institute or High Pressure Physics of the USSR Academy of Sciences* (1969).

[100] L. G. Khvostantsev, V. N. Slesarev and V. V. Brazhkin, *High Press. Res.* **24**, 371 (2004).

[101] L. G. Khvostantsev and V. A. Sidorov, *Phys. Stat. Sol. (a)*, **82**, 389 (1984).

[102] L. F. Vereshchagin, L. G. Khvostantsev and V. A. Sidorov, *High Temp. High Press.*, **9**, 629 (1977).

[103] https://www.researchgate.net/publication/271021637_Modeling_the_effect_of_ resistivity_of_the_heating_element_on_temperature_distribution_in_the_ Bridgman - type _ Toroidal_Anvil.

[104] G. Morard , M. Mezouar , N. Rey , R. Poloni , A. Merlen , S. Le Floch , P. Toulemonde , S. Pascarelli , A. San-Miguel , C. Sanloup and G. Fiquet, *High Press. Res.* **27**, 223 (2007).

[105] Y. Kono, C. Park, C. Kenney-Benson, G. Shen and Y. Wang, *Phys. Ear. Planet. Inter.* **228** , 269 (2014).

[106] M. Burchard, C. Weikusat, U.A. Glasmacher, S. Klotz, R. Miletich, C. Trautmann and R. Neumann, pp 345, *GSI Scientific Report* (2008).

[107] R. C. Liebermann, *High Press. Res.* **31,** 493 (2011).

[108] A. Kubo and M. Akaogi, *Phys. Earth Planet. Inter.* **121**,85 (2000).

[109] S. Zhai and E. Ito, *Geosci. Front.* **2**, 101 (2011).

[110] https://d32ogoqmya1dw8.cloudfront.net/images/NAGTWorkshops/mineralogy/ mineral_ physics/crunched_multi_anvil_cell.jpg.

[111] N. Dubrovinskaia, L. Dubrovinsky, N. A. Solopova, A. Abakumov, S. Turner, M. Hanfland, E. Bykova, M. Bykov, C. Prescher, V. B. Prakapenka, S. Petitgirard, I. Chuvashova, B. Gasharova, Y. L. Mathis, P. Ershov, I. Snigireva and A. Snigirev, *Sci. Adv.* **2,** e160034 (2016).

[112] J. Xu, J. Yen, Y.Wang and E. Huang, *High Press. Res.* **15**, 127 (1996).

[113] K. Furuno, A. Onodera and S. Kume, *Jap. J. Appl. Phys.* **25**, L646 (1986).

[114] J. Xu and H. K. Mao, *Science* **290**, 783 (2000).

[115] J. Xu, H. K. Mao, R. J. Hemley and E. Hines, *J. Phys. Cond. Matt.* **14**, 11543 (2002).

[116] N. Dubrovinskaia and L. Dubrovinsky, *Rev. Sci. Instrum.* **74**, 3433 (2003).

[117] C. Zha and W. Bassett, *Rev. Sci. Instrum.* **74**, 1255 (2003).

[118] S. T. Weir, D. D. Jackson, S. Falabella, G. Samudrala and Y. K. Vohra, *Rev. Sci. Instrum.* **80**, 013905 (2009).

[119] H. P. Liermann, Z. Konopkova, W. Morgenroth, K. Glazyrin, J. Bednarcik, E. E. McBride, S. Petitgirard, J. T. Delitz, M. Wendt, Y. Bican, A. Ehnes, I. Schwark, A. Rothkirch, M. Tischer, J. Heuer, H. Schulte-Schrepping, T. Kracht and H. Franz, *J. Synchrotron Radiat.* **22**, 908 (2015).

[120] M. Mezouar, W. A. Crichton, S. Bauchau, F. Thurel, H. Witsch, F. Torrecillas, G. Blattmann, P. Marion, Y. Dabin, J. Chavanne, O. Hignette, C. Morawe and C. Borel, *J. Synchrotron Radiat.* **12**, 659 (2005).

[121] J.F. Lin, M. Santoro, V. V. Struzhkin, H. K. Mao and R. J. Hemley, *Rev. Sci. Instrum.*, **75**, 3302 (2004).

[122] A. F. Goncharov, J. C. Crowhurst, V. V. Struzhkin and R. J. Hemley, *Phys. Rev. Lett.* **101**, 095502 (2008).

[123] J. S. Zhang, J. D. Bass and G. Zhu, *Rev. Sci. Instrum.* **86**, 063905 (2015).

[124] A. Basu and R. Boehler, Conference, *APS March Meeting* (2017).

[125] G. Aquilanti, A. Trapananti, A. Karandikar, I. Kantor, C. Marini, O Mathon, S. Pascarelli and R. Boehler, *Proc. Nat. Acd. Sci.*, **112**, 12042 (2015).

[126] J. F. Lin, V. V. Struzhkin, S. D. Jacobsen, G. Shen, V. B. Prakapenka, H. K. Mao and R. J. Hemley, *J. Synchrotron Rad.* **12**, 637 (2005).

[127] J. Zhao, W. Sturhahn, J. F. Lin, G. Shen, E. E. Alp and H. K. Mao, *High Press. Res.* **24**, 447 (2004).

[128] G. Aprilis, C. Strohm, I. Kupenko, S. Linhardt, A. Laskin, D. M. Vasiukov, V. Cerantola, E. G. Koemets, C. McCammon, A. Kurnosov, A. I. Chumakov, R. Rüffer, N. Dubrovinskaia and L. Dubrovinsky, Rev. Sci. Instrum. **88**, 084501 (2017).

[129] S. Watson, W.N. MacPherson, J.S. Barton, J.D.C. Jones, A. Tyas, A.V. Pichugin, A. Hindle, W. Parkes, C. Dunare and T..Stevenson, *J. Phys.: Conf. Ser.* **15,** 226 (2005).

[130] K. Shigemori, Y. Hironaka, H. Nagatomo, S. Fujioka, A. Sunahara, T. Kadono, H. Azechi and K. Shimizu, *Appl. Phys. Lett.* **102**, 183501 (2013).

[131] A. Shyam and R. Shukla, *J. Phys.: Conf. Ser.* **377**, 012112 (2012).

[132] S. Brygoo, M. Millot, P. Loubeyre, A. E. Lazicki, S. Hamel, T. Qi, P. M. Celliers, F. Coppari, J. H. Eggert, D. E. Fratanduono, D. G. Hicks, J. R. Rygg, R. F. Smith, D. C. Swift, G. W. Collins and R. Jeanloz, *J. Appl. Phys.* **118**, 195901 (2015).

Chapter 2

Laser Heated Diamond Anvil Cell (LHDAC) Facility for HPHT Research

Diamond anvil cell based laser heating technique has emerged as a powerful and versatile experimental tool, in recent times, for achieving ultrahigh pressures ($P > 100$ GPa) and temperatures ($T \sim 6000$K) thus enabling the study of phase behaviour of materials at thermodynamic conditions comparable to the Earth's deep interior. Currently, single sided as well as double sided laser heating techniques are widely used in synchrotron beam lines and laboratories, making it a vital technique to bridge the gap between the pressure achieved by shock experiments and static high pressures achieved by other large volume devices like toroidal and multi-anvils described in **Chapter 1** [1].

This chapter discusses the instrumentation details of the state of the art LHDAC facility developed at the High Pressure and Synchrotron Radiation Physics Division (HP&SRPD), Bhabha Atomic Research Centre (BARC) for accurate determination of thermodynamic properties like pressure dependent melting and synthesis of novel materials at HPHT. The first part of the chapter describes the design aspect and mode of operation of the LHDAC facility. The results of HPHT synthesis of gallium nitride (GaN) [2] and molybdenum nitride (γ-Mo_2N) and high pressure melting curve of KBr are also presented in the chapter with an aim to highlight the capabilities of the facility.

2.1 DAC Based Laser Heating

The principal requirement for laser heating is a stable high power laser of appropriate wavelength *viz*., near infrared (NIR) or mid infrared (MIR) laser that couples with the sample directly [3, 4]. The transparency of diamond in the infrared (IR) region allows the use of continuous wave (CW) NIR lasers such as neodymium doped yttrium aluminium garnet (Nd^{3+}:YAG), neodymium doped yttrium lithium fluoride (Nd^{3+}:YLF), ytterbium (Yb) doped fibre laser or MIR CO_2 laser, the choice being driven by the sample absorbance [5-7]. The NIR laser is usually used to heat metallic materials. In this case, the thermal energy results from the collision of the excited electrons, created by photon-electron interaction, with the lattice phonons. The MIR CO_2 laser, on the other hand, is more suitable to heat minerals and transparent oxides, exploiting the absorption of IR radiation by the lattice phonons. Alternatively, it is also possible to heat the optically transparent minerals and oxides with the NIR laser using certain laser absorber, like W, Pt, Ir *etc*., which absorb the NIR laser radiation and transfer the thermal energy to the sample [8, 9]. The different emission wavelength of the laser also necessitates the use of different optics. Thus BK7 glass is used with the NIR laser source whereas ZnSe or CaF_2 optics are necessary when MIR CO_2 laser is used.

2.2 Experimental Details

2.2.1 Design of single sided laser heated diamond anvil cell facility

The major components of the LHDAC facility are a continuous wave (CW) air cooled ytterbium (Yb) doped fibre laser (λ = 1.07 µm, 100 W, TEM_{00}, SP-100C-A-S6-A-A), an indigenously developed Mao-Bell type DAC mounted on a high precision motorized XYZ stage

(Kohzu YA 10A-R1 and ZA07A-VIF) and a 163 mm spectrograph with a 300 line grating (Shamrock SR-163) coupled with a Peltier cooled CCD (Andor-DV 420-OE). The photograph of the single sided LHDAC facility is shown in Fig. 2.1.

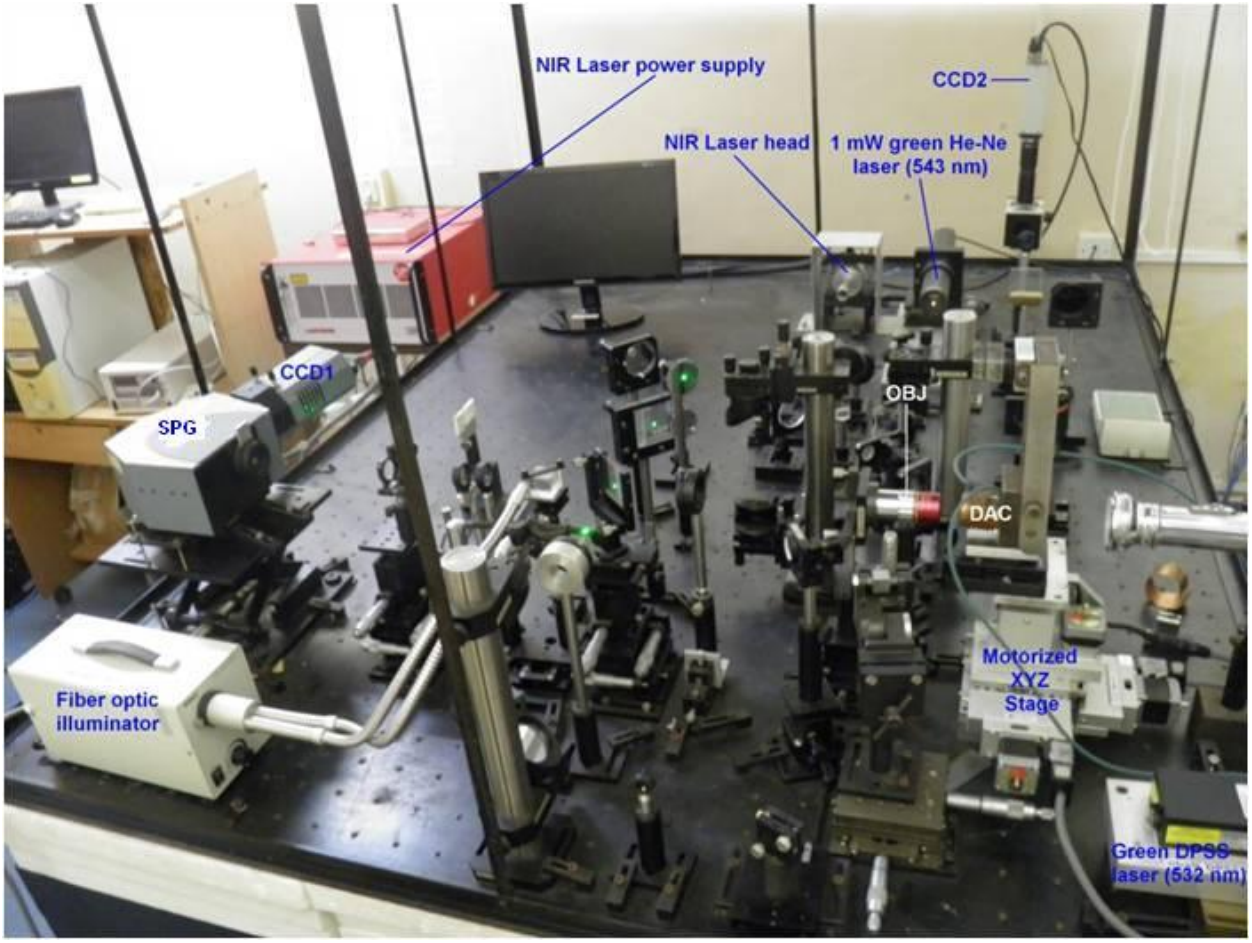

Fig. 2.1: *Photograph of the single sided LHDAC facility.*

The Yb doped fibre laser system serves as an excellent alternative to the Nd:YAG laser with a remarkable combination of high power, ideal beam quality, high stability, fibre delivery, compactness, selectivity of operating wavelength and a reliability that is superior than the conventional solid state or gas laser. These attributes, coupled with its low weight, make it most suitable for its ease of setting up and portability of the system [10]. The laser power control is achieved by a simple dc power supply and is computer controlled. Its high power and a near perfect Gaussian beam profile is well suited to heat the sample in a DAC. The distribution of the IR laser intensity has a Gaussian shape with a beam diameter of ~ 5 mm which increases to ~10 mm when a 2X beam expander is used. The optical arrangement of the LHDAC facility is shown schematically in Fig. 2.2. The laser beam is focussed on the sample with the help of beam steerer (BS1) and a 75 mm focal length plano-convex lens (L1). An NIR infinity corrected long working distance (30 mm) apochromatic objective (OBJ) with 10X magnification facilitates the observation of the sample in the DAC by illumination of white light. It also enables collection of thermal radiation from the hotspot, which is then fed into the spectrograph (SPG), thus giving access to multiwavelength spectroradiometry. The infinity corrected apochromatic objective also minimizes the spherical and chromatic aberration upon insertion of auxiliary devices into the data collection optical path. The aperture (A), which is an iris, reduces the beam diameter and hence minimizes the aberration introduced by OBJ and the achromatic lens (L2) in the collection path. The combination of OBJ and L2 is used to form an image of the sample at the spectrograph input with 10X optical magnification. The standard rectangular spectrograph input slot is replaced with a 30 µm diameter mirror polished pinhole (PH) to ensure collection of thermal radiation from only a 3 µm circular area within the hotspot.

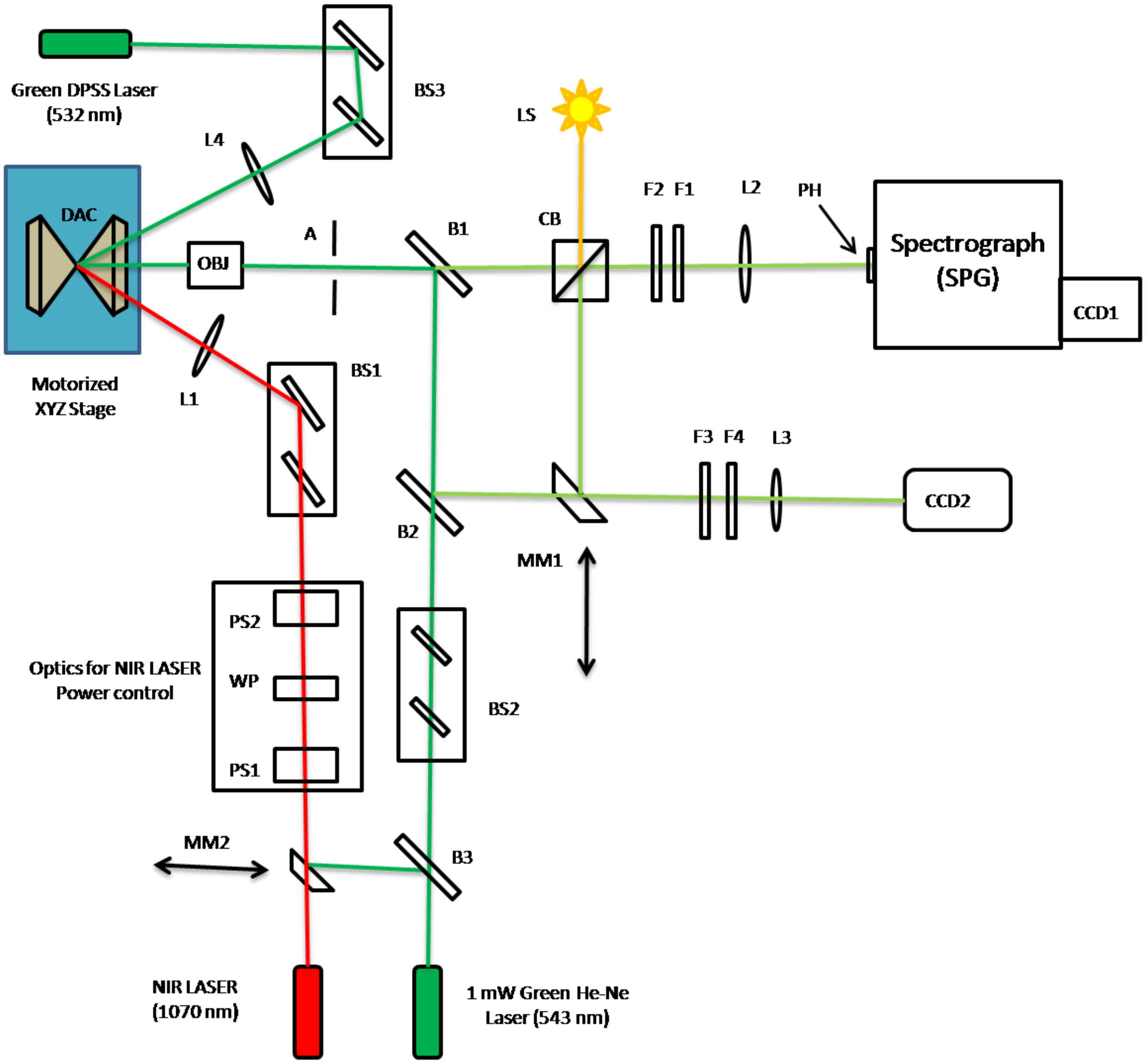

Fig. 2.2: *Simplified schematic layout of the LHDAC facility. OBJ: infinity corrected long working distance apochromatic objective; L1, L3, L4: plano-convex lenses; L2: achromatic lens; SPG: spectrograph (Shamrock SR-163); PH: 30µm pinhole; BS1, BS2, BS3: beam steerers; PS1, PS2: polarizing beam splitters; WP: λ/2 wave plate; MM1, MM2: movable mirrors; B1, B2, B3: 50:50 beam splitters; CB: cubic beam splitter; F1, F3: low pass filters; F2, F4: neutral density filters; A: aperture (iris); LS: fibre optic illuminator; DAC: diamond anvil cell. CCD1: Peltier cooled CCD (Andor-DV 420-OE) for spectroradiometry; CCD2: visual CCD for sample imaging.*

For accurate temperature determination, it is very crucial to centre the hotspot around the spectrograph pinhole (PH) as shown in Fig. 2.3. This is achieved by incorporating an imaging system consisting of a high resolution visual CCD (CCD2). In addition, CCD2 also facilitates a real-time imaging of the sample inside the DAC. To achieve perfect alignment of the hotspot, the non-polarising cubic beam splitter (CB) is aligned so as to reflect half of the backscattered radiation from the PH, which is then focused by a 20 mm focal length planoconvex lens (L3) onto CCD2. The image of the sample at the spectrograph input (PH) and the DAC sample chamber is observed using CCD2 by sliding the mirror (MM1) into and out of the optical path respectively.

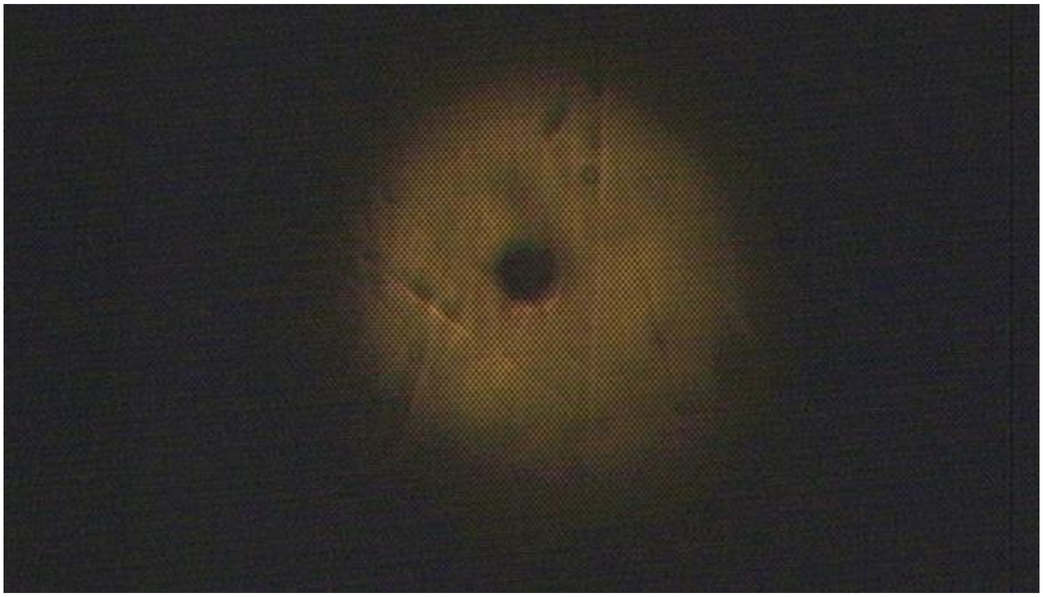

Fig. 2.3: *Photograph of the centrally aligned hotspot around the spectrograph pinhole (PH) during laser heating.*

It may be noted that a critical aspect of the LHDAC facility is to ensure that the focus of thermal radiation collection optics coincides with that of the heating NIR laser. Hence a 1 mW green He-Ne laser is used as an aligning laser. Optical alignment is achieved by coinciding the optical path of NIR and the aligning laser using beamsplitter (B3) and movable mirror MM2. The optical path of the NIR laser also includes two crossed polarizer beam splitter cube combination (PS1 and PS2) with a λ/2 waveplate (WP) between them. The laser power incident on the sample could be precisely controlled, keeping the beam profile unchanged, by rotating WP, which is mounted on a motorized rotation stage, thereby enabling precise and fine control of the incident IR laser power. This is imperative for accurate determination of melting temperature. A 300 mW green diode pumped solid state (DPSS) laser (Cobolt Samba, λ = 532 nm) has also been incorporated in the set up. This laser serves as the probe laser for speckle method, the details of which are described in the **Section {2.2.5.2}**. The precise positioning of NIR laser on the sample inside the DAC is another critical requirement in laser heating experiments. There is a danger of damaging the diamond anvils in case of incorrect positioning. Hence a high precision motorized XYZ stage is incorporated in the set up to achieve fine and reproducible positional control of the sample with respect to the focussed laser spot. Furthermore, in order to avoid sample defocusing during laser heating, it is essential to maintain the DAC body at near ambient conditions. This is achieved with the help of an in-house fabricated water-cooling jacket for the DAC as shown in Fig. 2.4.

The salient feature of the LHDAC facility is an angular geometry with an off-axis incidence of the NIR laser beam on the sample. The advantage of off-axis angular geometry over the conventional on-axis heating geometry is that the optical components for laser focusing and for collection of incandescent light are aligned and optimized for their different wavelengths separately.

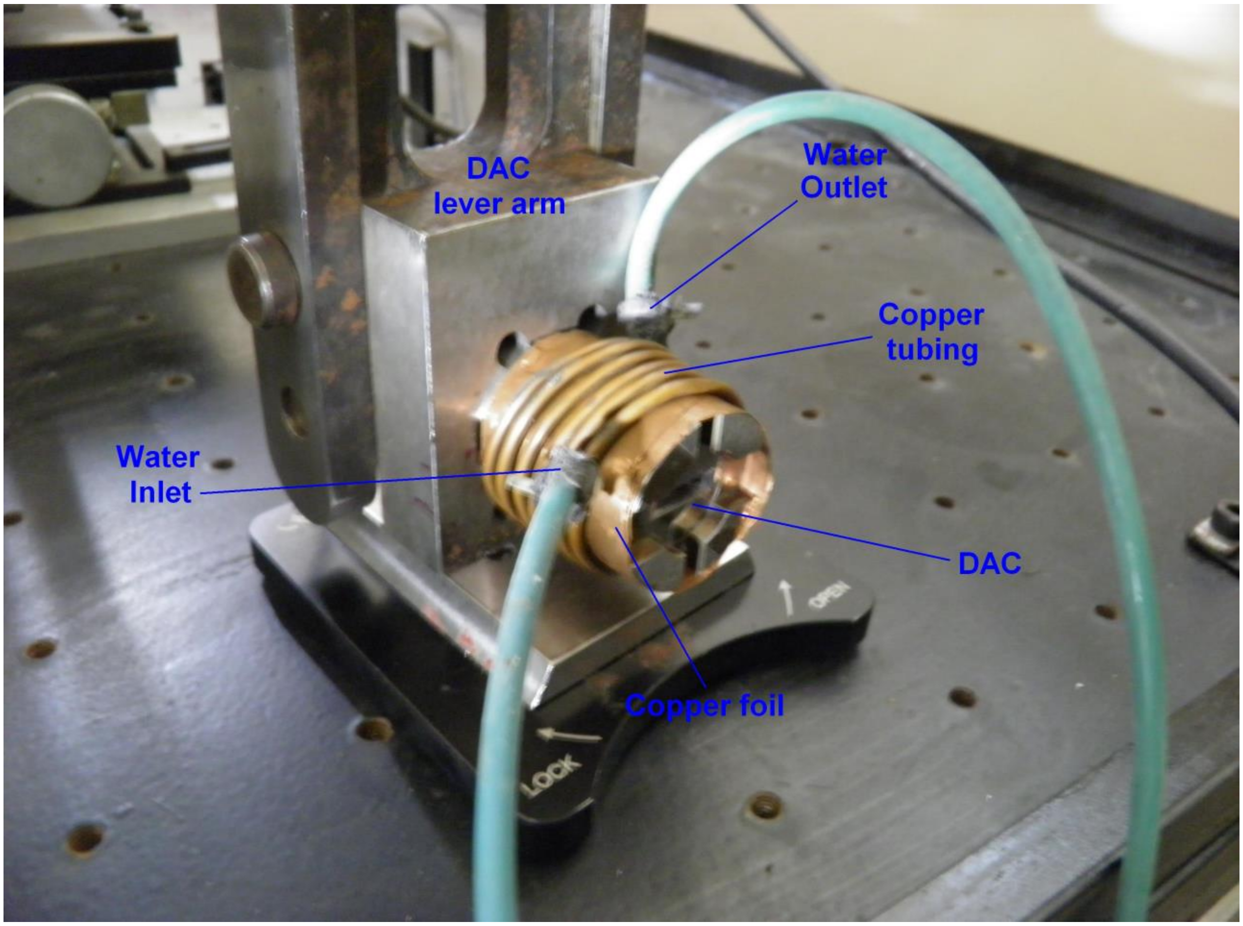

Fig. 2.4: *Photograph of the water cooling jacket for the Mao Bell type DAC.*

This facilitates an independent control over the heating laser spot size, which in turn defines the sample hot spot size during heating. Thus with a larger hotspot, the radial temperature gradient at the sample, as described in **Section {2.2.4}**, is reduced resulting in a nearly flat temperature profile within the central 3 µm probed sample region. In addition, the off-axis geometry prevents obstruction of the diffracted beam by any optical component in LHDAC based *in situ* spectroscopic measurements.

2.2.2 Sample loading in diamond anvil cell

The sample loading forms a crucial aspect of the laser heating experiments. The studies in this thesis have been carried out using a Mao-Bell type of DAC, with diamonds of ~ 400 µm culet size. Stainless steel, tungsten, or rhenium gasket with ~ 200 µm diameter hole served as the sample chamber. Prior to the experiment, the gasket with a starting thickness of ~ 250 µm was preindented between the diamond anvils to a thickness of ~ 50 µm. For all high pressure experiments, the sample along with a few ruby balls and a pressure transmitting medium (PTM) was loaded inside the sample chamber. The schematic arrangement of the sample chamber and its image are shown in Fig. 2.5 (a and b) respectively.

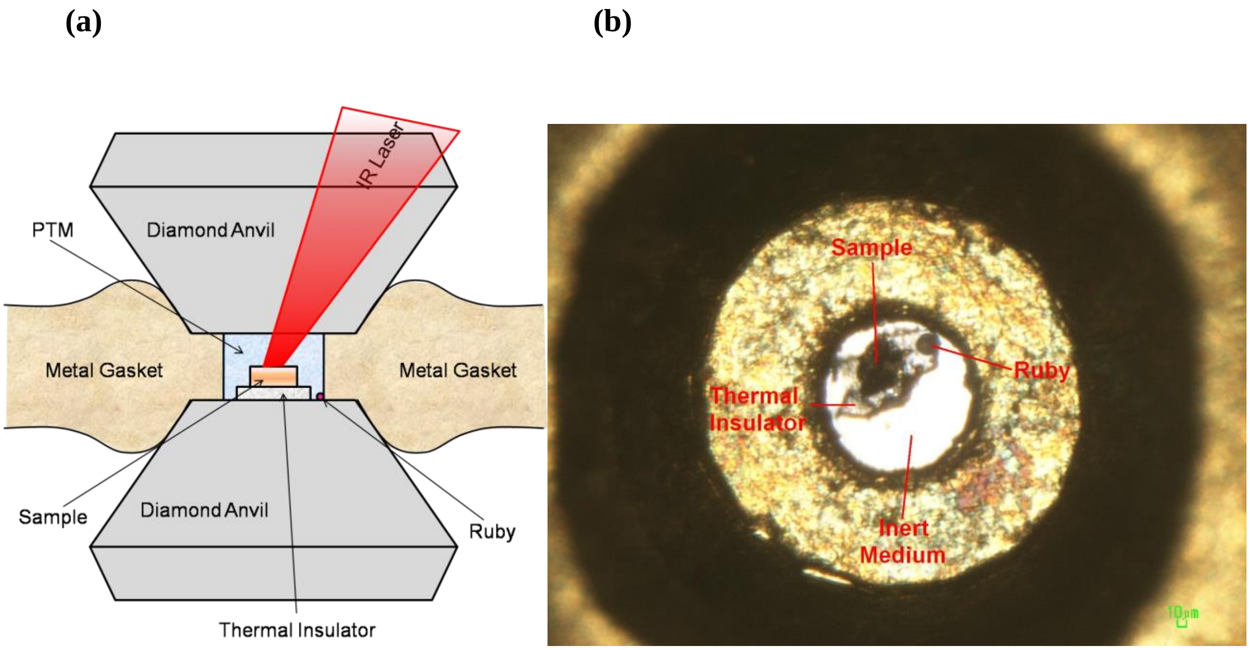

Fig. 2.5: *(a) Schematic diagram and (b) image of a typical sample assembly used for LHDAC experiment.*

The role of PTM, which is usually a material of low shear strength, is to minimize the deviatoric stresses in the sample and to create a hydrostatic pressure from a uniaxial compression. In addition, the PTM also acts as a chemical barrier and prevents any reaction of the sample with the gasket or diamond culets. Furthermore, since diamond, due to its high thermal conductivity, acts as an extremely efficient heat sink, the PTM also serves as a thermal insulator in laser heating experiments, preventing the conduction of heat from the sample to the diamond. Soft solids with low thermal conductivity like CsI, KBr, NaCl are the commonly used PTM. Alternatively, hard solids such as MgO and Al_2O_3 are also used owing to their chemical inertness, high melting point and low thermal conductivity even though they provide a nonhydrostatic media. In certain laser heating experiments, solid PTM are not suitable due to their chemical reactivity at HPHT. In such cases, noble gases like Ar, He and Ne are the suitable PTM. The benefits of noble gas PTM in laser heating experiments include its chemical inertness, near-hydrostatic pressure conditions around the heated sample due to its low melting temperature and good thermal insulation from the diamonds due to its low thermal conductivity. In our laser heating experiments we have used either NaCl, KBr, Al_2O_3 as solid PTM and thermal insulator. Alternatively, we have loaded liquefied argon inside the sample chamber by immersion technique, using a cryogenic apparatus, as shown in Fig. 2.6. For this, the piston-cylinder of the DAC, with sample loaded, is placed inside the cryogenic apparatus. The entire cryogenic apparatus is then lowered inside a thermocol box into which liquid nitrogen is poured. Argon gas is then let inside the cryogenic apparatus through the copper tubing welded around it. The liquefaction of argon gas (boiling point 87.2 K) is achieved by cooling, using liquid nitrogen (boiling point 77.2 K). The piston cylinder is then clamped and then transferred to the lever arm for carrying out high pressure measurements.

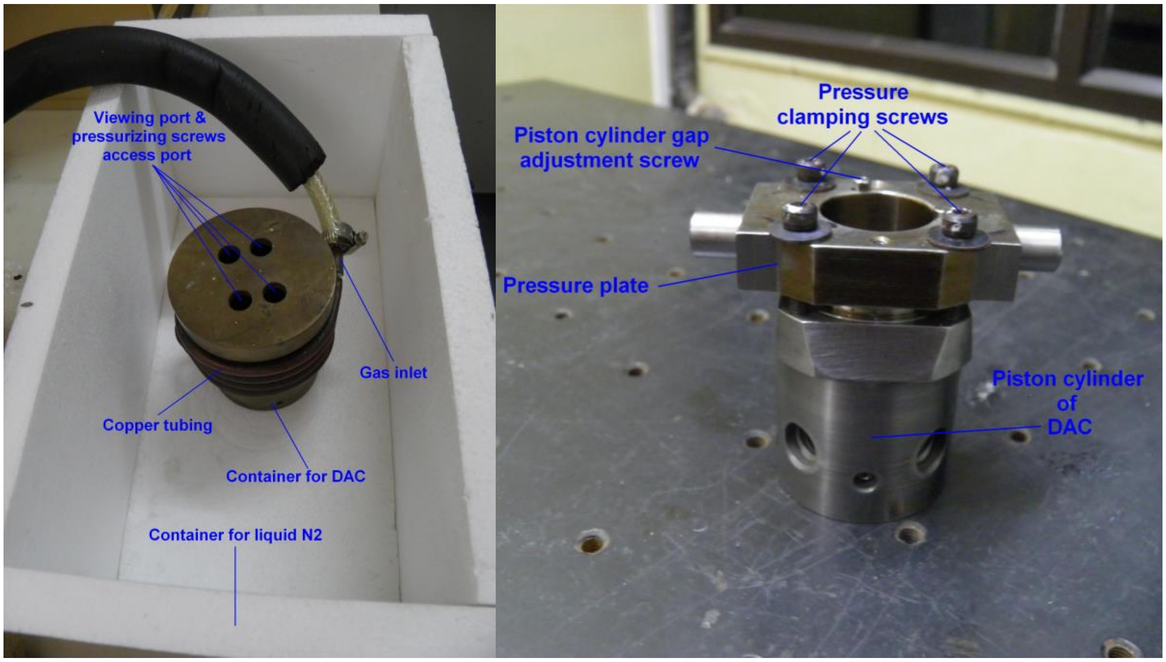

Fig. 2.6: *Cryogenic apparatus for loading liquefied argon inside the DAC sample chamber.*

2.2.3 Pressure measurement

The sample pressure was determined by *in situ* ruby fluorescence method by measuring the pressure shift of the R1 flourescence line (λ = 694.22 nm) of the ruby ball, loaded inside the sample chamber of the DAC, with the green DPSS laser (λ= 532 nm) [11]. Alternatively, the pressure was measured using a standalone ruby fluorescence set up. The pressure was determined both before and after the laser heating experiment at room temperature.

2.2.4 System calibration and temperature measurement

The accurate and precise temperature determination of the heated sample is of utmost importance in LHDAC experiments. A critical issue in this case is the presence of radial and axial temperature gradients [12]. The radial temperature gradients in LHDAC arise from variation in laser intensity in the plane of the diamond culet and gasket hole, perpendicular to the incoming laser beam whereas the axial temperature gradients arise from the flow of heat away from the hotspot due to the high thermal conductivity of diamonds. While the axial temperature gradients can be minimized by double sided heating of the sample, the radial temperature gradients can be minimized by increasing the size of incident IR laser spot formed on the sample [13]. A well known technique to achieve this is by using a pi shaper, which produces a flat top temperature profile at the sample position [14]. Alternatively, the angular incidence geometry, adapted in our set up, facilitates this by providing an independent control over the hot spot size. In particular, for a typical 40 µm diameter hotspot of the incident IR laser, the central 3-4 µm heated region has a nearly flat temperature profile. Hence in the present setup, with the help of a pinhole (PH), we allow incandescent light only from a 3 µm central hotspot, into the spectrograph for temperature measurement.

The sample temperature is measured by spectroradiometric technique wherein incandescent light emitted by the heated sample is collected by the spectrograph (SPG) in a 400 nm spectral width (500 nm to 900 nm). The emitted thermal radiation is governed by the Planck's blackbody radiation law as given in Eq. 2.1 [15, 16].

$$I_v(\lambda,T)=\varepsilon(\lambda,T)\left(\frac{1}{\lambda^5}\right)\frac{2\pi c^2 h}{\left(\exp\left(\frac{hc}{KT\lambda}\right)-1\right)} \tag{2.1}$$

where $I_\upsilon(\lambda,T)$, $\varepsilon(\lambda,T)$, h, k and c are the observed spectral intensity, emissivity, Planck's constant, Boltzmann constant and speed of light respectively. Emissivity described in Eq. 2.1 is a function of pressure, temperature and wavelength. It is the ratio of radiation emitted from a real body to the radiation from a black body at the same temperature in thermal equilibrium. Thus it has a value of 1 for an ideal black body and between 0 and 1 for a real body. However the knowledge of wavelength dependent emissivity of materials at HPHT conditions is not known. To overcome this problem one has to parameterize emissivity along with temperature. The parameterization of emissivity is made feasible by assuming a gray body approximation *i.e.*, invariance of emissivity over measured wavelength range [17]. Furthermore, in a LHDAC facility, the optical elements and their alignment have a crucial effect on the temperature measurement and hence the incandescent radiation collected from the heated sample by the LHDAC optics is given by

$$I_S(\lambda,T) = R(\lambda)\varepsilon(\lambda,T)\left(\frac{1}{\lambda^5}\right)\frac{2\pi c^2 h}{\left(\exp\left(\frac{hc}{KT\lambda}\right)-1\right)} \tag{2.2}$$

where R(λ) is the instrument spectral response function of the optical set up used for collecting thermal radiation. The instrument spectral response function R(λ) of the optical set up is prerequisite for carrying out temperature measurement. In order to determine R(λ), the incandescent spectrum emitted by a standard calibration lamp (I_{std}) at a known temperature (T_{std}) is measured with the same optics as used in the actual experiment. The spectral intensity (I_{std}) is mathematically divided by the spectral intensity calculated from Planck's equation at T_{std} in the same wavelength range. The resulting quotient is the instrument spectral response function (R(λ)). The raw spectrum collected in an experimental run at an unknown temperature (T) is then divided by R(λ) to yield a corrected spectrum, which is subsequently fitted with the Planck function to extract the temperature. In the present study, the temperature calibration was carried out using a quartz tungsten halogen (QTH) calibration lamp (Sciencetech, 24W, 250 V). Figure 2.7(a and b) shows the instrument response function R(λ) and the typical emission spectra of the LHDAC set up respectively.

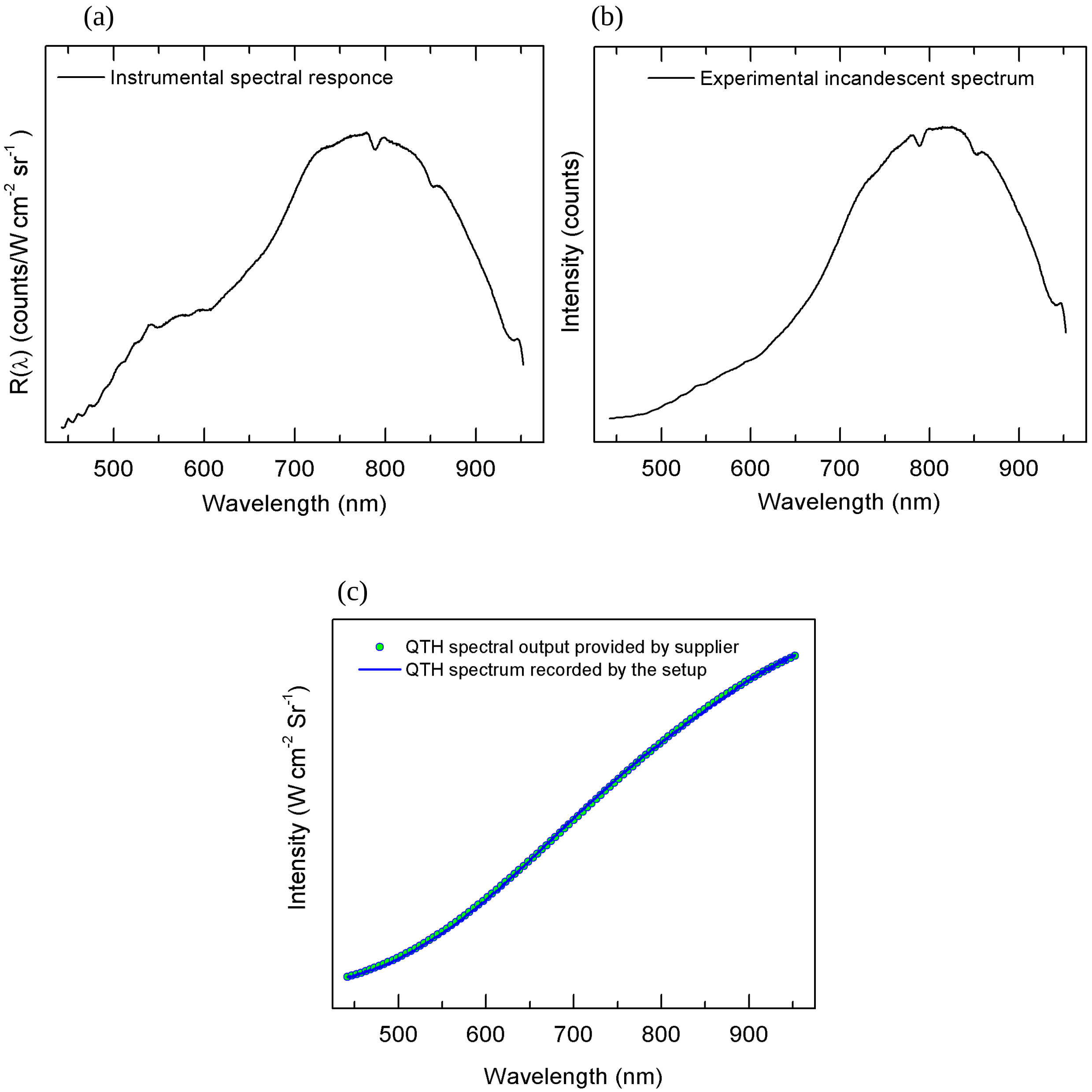

Fig. 2.7: *(a) instrument spectral response (b) Typical observed experimental incandescent spectrum and (c) comparison of QTH calibration lamp spectrum obsereved in our setup with spectrum provided by the supplier.*

2.2.5. Melting study

2.2.5.1 Phenomenon of melting

The study of melting curve of materials under HPHT is of fundamental importance for basic science as well as for geophysical reasons. Thermodynamically, a material is said to melt when the Gibbs free energy of solid and liquid phase becomes equal for given pressure. The temperature at which the Gibbs free energies become equal is called its melting temperature at that pressure. At the melting temperature, the solid and liquid phase coexists in equilibrium. The fraction of solid and liquid phase depends on the amount of heat energy supplied, called latent heat.

$$G_{solid}\ (P,T_m) = G_{liquid}\ (P,T_m) \qquad (2.3)$$

where G_{solid} and G_{liquid} are Gibbs free energy of solid and liquid phase respectively. P is pressure and T_m is melting temperature at pressure P. Gibbs free energy is defined as

$$G = U + PV - TS \qquad (2.4)$$

where U is internal energy, P is pressure, V is volume, T is temperature and S is entropy.

The Gibbs free energy of the material changes with pressure and results in variation of the melting temperature of material with pressure.

Several melt criteria have been proposed in order to measure the melting temperature. Instability caused by vibrational motion of two simple rigid sublattices against each other [18], diminishing of the second derivative of lattice energy with respect to lattice spacing [19], minimization of pressure with volume change [20], structural order-disorder transition [21] and failure of elastic resistance against a shearing stress [22] are the important melt criteria based on atomic properties. Although most of these criteria are used for determination of melting temperature in theoretical methods, they cannot be directly implemented for experimental determination of melting temperature unless they are manifested in the form of observable properties of solids. Hence several other criteria have been proposed for detection of onset of melting in experimental measurements.

2.2.5.2 Detection of onset of melting in high pressure LHDAC experiments

There is a lack of agreement among the various HPHT studies on the measured melting temperature. This reflects the experimental difficulty in precise identification of onset of melting and its accurate measurement. The various criteria for detection of melting in high pressure LHDAC experiments are listed below:

i. Visual observation of the heated sample. This method however suffers from large errors [23].
ii. Slope change in the plot of laser power as a function of temperature resulting from the different optical properties of the new phase formed upon melting [24].
iii. Distinct change in reflectivity detected by a sharp change in the intensity of the reflected signal measured by a photo diode [24].
iv. Flash heating method in which distinct areas of the pressurized sample are subjected to short single laser pulses of a few milliseconds duration with ascending/descending input laser power. This results in a gradual change in temperature of these areas [25]. Scanning

electron microscope (SEM) measurement is carried out on the post heated retrieved sample wherein onset of melting is indicated by the first observation of bead formation due to recrystallization. The corresponding incandescent spectrum is then used to determine the melting temperature.

v. *In situ* x-ray diffraction to look out for a signature of diffuse scattering from the liquid phase [13,14].

vi. Sharp jump in the resistance of the sample upon melting [26].

vii. Laser speckle method wherein a defocused visible laser incident on the heated sample surface creates a speckle interference pattern, as shown in Fig. 2.8, due to its surface roughness [27, 28]. The onset of a continuous motion of this speckle pattern is inferred as the melting point. The laser-speckle method enables one to distinguish between a solid-liquid transition in which a continuous speckle motion is observed and a solid-solid transition that shows up as an abrupt, discontinuous change in laser speckle pattern [29].

viii. Temperature plateau method wherein the incident IR laser power is increased/decreased in very fine steps leading to a corresponding change in the sample temperature. The plot of sample temperature *vs* incident laser power shows a plateau that corresponds to a small range of incident laser power for which sample temperature remains stable. This plateau is attributed to the latent heat associated with solid to liquid phase transition.

In the present thesis work, flash heating, laser speckle and temperature plateau methods have been adapted for determination of melting temperature. All the three methods have their own advantages and limitations. It may be noted that the flash heating method, which is performed in the millisecond time scale prevents any chemical reactions.

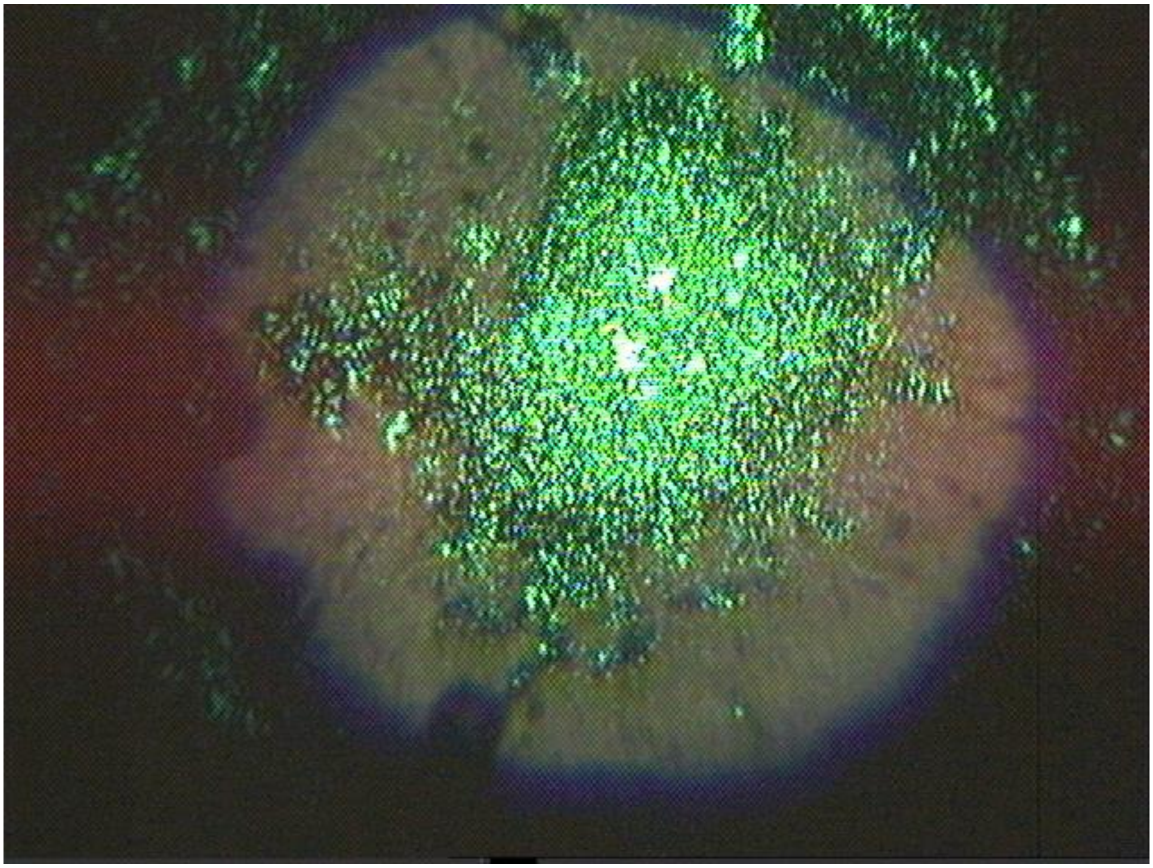

Fig. 2.8*: In situ photograph of laser speckle pattern form on solid sample inside DAC.*

In addition, SEM analysis of the post heated sample distinguishes between pre-melting and bulk melting of the sample unambiguously thus bracketing the melting temperatures within ±100 K. However the limitation of this technique is the necessity of multiple flash heating runs at each pressure, each requiring fresh identical sample and the time consuming *ex-situ* sample analysis techniques. Furthermore, it is not suitable for substances such as solid forms of gases and liquids, which are irretrievable at ambient conditions, for SEM analysis. The speckle method, on the other hand, attributes onset of melting to the motion of laser speckle due to changes in surface texture of the sample during melting. However, surface modification during pre-melting could also result in changes in speckle pattern. Hence this method can result in underestimation of the melting temperature in some cases. The advantage of this method however is its suitability for all materials and the relative ease of measurement, since a single sample loading is adequate to carry out melting temperature measurements at various pressures. Although the temperature plateau method does not distinguish between solid-solid and solid-liquid transition, it is useful in resolving the underestimation of the melting temperature due to pre-melting. Furthermore, the simultaneous implementation of laser speckle and temperature plateau method in determination of onset of melting has also been successfully adapted in the present LHDAC facility.

The melting temperatures at ambient pressure of known elements like iron, tungsten, tantalum *etc.*, were determined in order to standardize the experimental set up. Figure 2.9 (a and b) shows the SEM images of post heated iron sample by flash heating method. It may be noted that the observed ambient melting temperature of 1747(75) K is in reasonable agreement with the reported melting temperature of 1811 K for iron [30]. Melting temperature of gadolinium metal (Gd) at ambient pressure using temperature plateau method has been determined as 1536 K as shown in Fig. 2.10 which is in good agreement with reported melting temperature 1585 K [31].

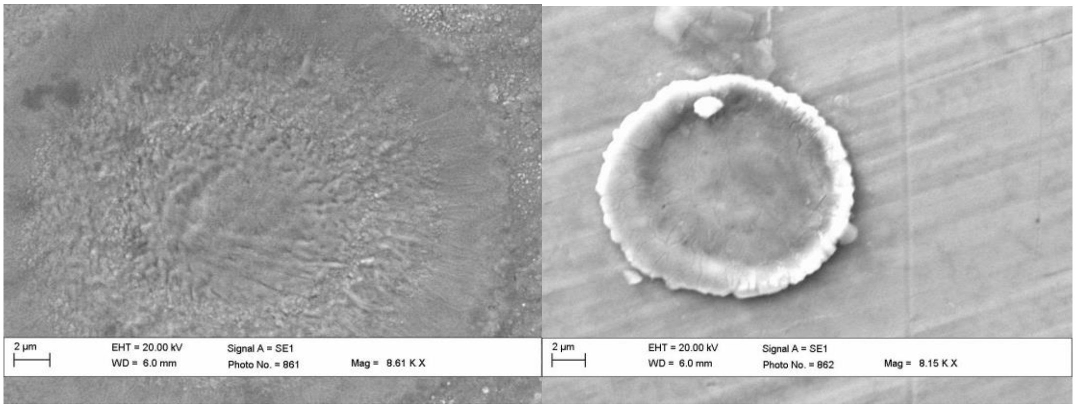

Fig. 2.9: *SEM image of post laser heated iron sample using flash heating method depicting (a) emergence of textural changes (b) bead formation upon recrystallization.*

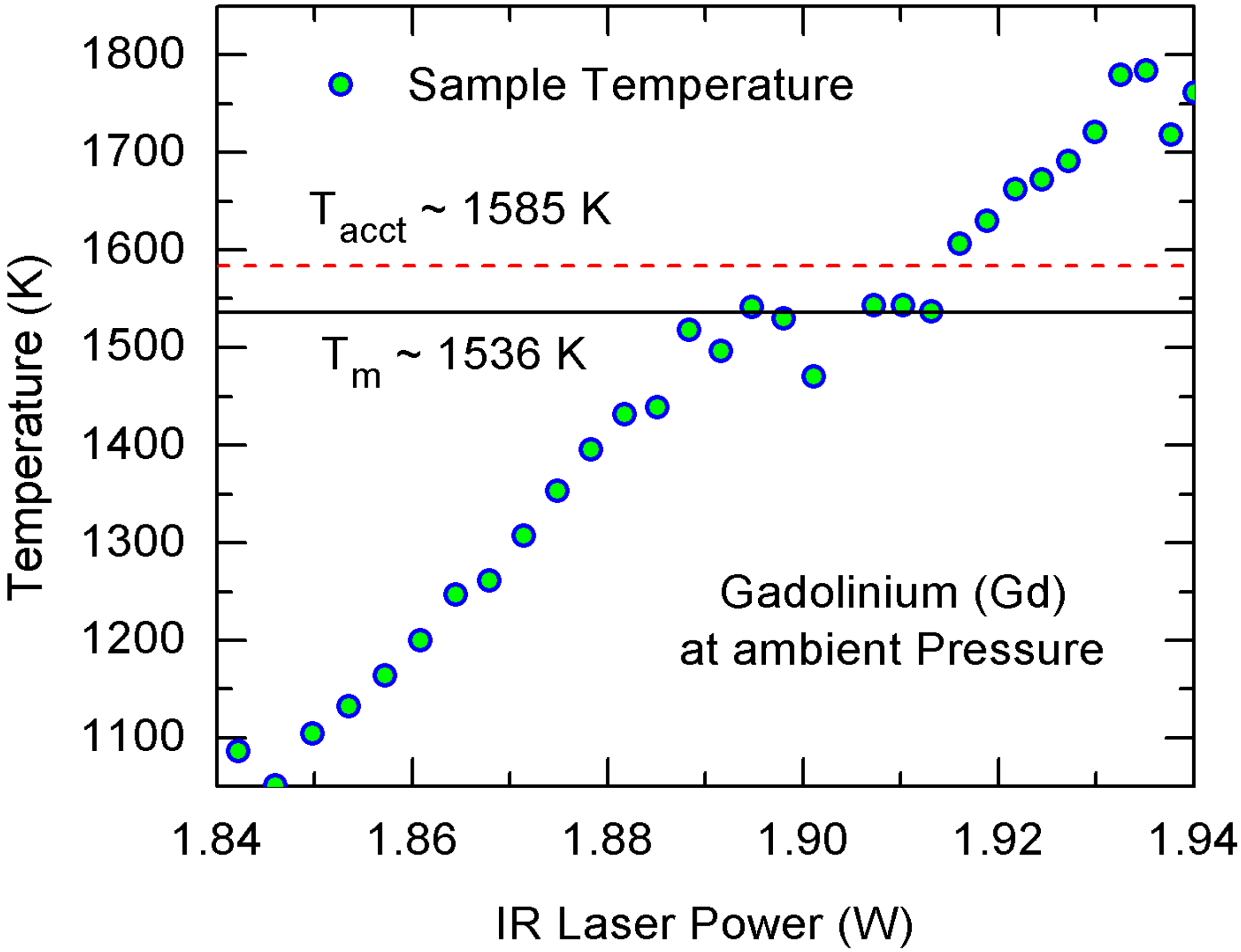

Fig. 2.10*: Melting temperature determination of gadolinium (Gd) using temperature plateau method.*

2.3. Results and Discussion

The laser heating facility has been employed for material synthesis and melting experiments under HPHT. The performance evaluation of this facility was carried out with several benchmarking melting experiments on standard samples such as Fe, Pt, W *etc*. A few recent material synthesis and melting studies carried out on materials at high pressures are discussed in the next subsections.

2.3.1 HPHT synthesis of metal nitride

Transition metal nitrides have received considerable attention in recent years due to their remarkable physical properties, such as high melting point, low compressibility and high hardness as compared to pure metal [32, 33]. Hence they are promising candidates in the search for superhard materials. Among them, GaN with direct band gap of 3.4 eV is extensively used for light emitting diode (LED), optoelectronic application, laser diode, high power and low frequency device applications *etc*. GaN has been reported to crystallize in the wurtzite structure. Gallium metal does not react with nitrogen at ambient conditions. Hence reaction of gallium metal or gallium oxide (Ga_2O_3) with ammonia is commonly used for synthesis of GaN. Similarly, prediction of superconductivity in molybdenum nitride has led to an extensive study of its synthesis [34]. Molybdenum nitride has been reported to crystallize as δ-MoN in hexagonal structure (SG: *P63/mmc*) and γ-Mo_2N in ordered NaCl structure (SG: *Fm-3m*) [35]. Both these compounds possess high bulk modulus and show superconductivity at low temperatures. These results motivated us to carry out HPHT synthesis of GaN and γ-Mo_2N by direct chemical reaction between elemental gallium and molybdenum with molecular nitrogen at HPHT.

2.3.1.1 HPHT Synthesis of GaN

Mao-Bell type DAC in conjunction with LHDAC facility was employed for synthesis of GaN. Gallium metal foil of thickness ~10 μm and diameter ~80 μm, along with a few ruby balls (~10 μm), was loaded into a 125 μm diameter hole of a hardened stainless steel gasket preindented to a thickness of 50 μm. Liquid nitrogen was loaded in the DAC by cryogenic immersion method. It acted as the PTM as well as reactant for the nitride synthesis. The DAC was then pressurized to 9 GPa. Pressure measurement was carried out by ruby fluorescence method. On focusing the NIR laser on the gallium foil, bright thermal radiation, emitted by the heated sample, was observed on the visual CCD (CCD2) indicating good coupling of the sample with the laser. The sample was laser heated at 35 W input laser power for 90 minutes. A water-cooling jacket arrangement for the piston cylinder of the DAC prevented the DAC body from heating up. The sample temperature was recorded in time interval of 10 minutes by spectroradiometry. As is evident from Fig. 2.11 the sample temperature decreased with time up to 60 minutes from its initial value of 1925 K and thereafter became constant.

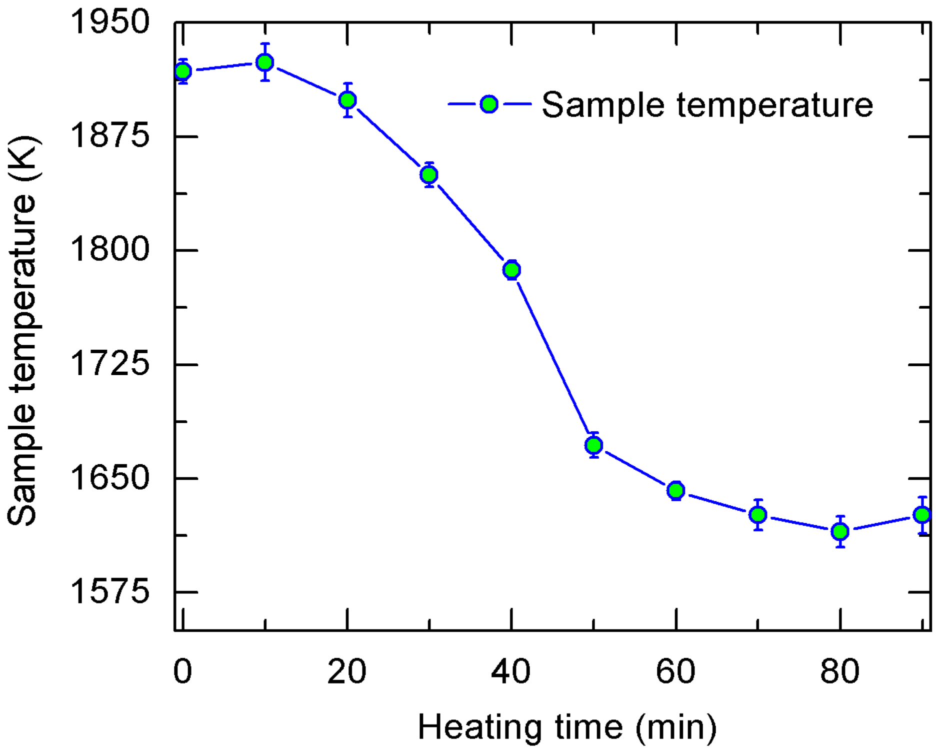

Fig. 2.11*: Sample temperature as a function of time.*

This indicates a change in the IR laser coupling with the sample and could be an indirect indication of completion of chemical reaction of Ga with N_2. This is also evident from *in situ* photographs of incandescent light emitted by the sample at time t=0 and t=30 minutes as shown in Fig. 2.12 (a and b) respectively.

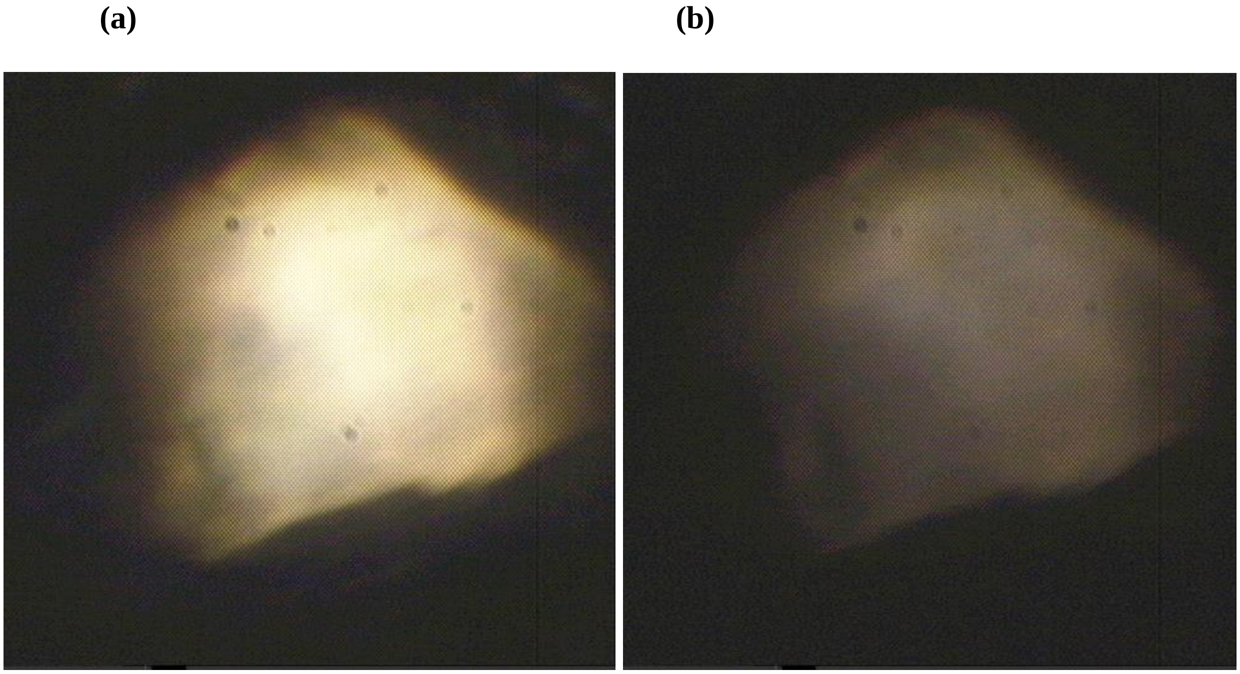

Fig. 2.12: *In situ photograph of incandescent light emitted by sample at a) time t=0 and b) t=30 minutes.*

Raman spectrum of the pressurized sample was recorded both before and after heating. Raman measurements prior to heating as depicted in Fig. 2.13a shows only nitrogen modes. Raman spectrum of the post laser heated sample as shown in Fig. 2.13b is in good agreement with that of Raman modes of GaN in wurtzite phase indicating the synthesis of GaN. ADXRD measurements on the post heated sample was performed at BL 11 beamline of INDUS 2 synchrotron, Indore, India. Le bail refinement of ADXRD data as shown in Fig. 2.14 confirms the synthesis of GaN in wurtzite phase [36].

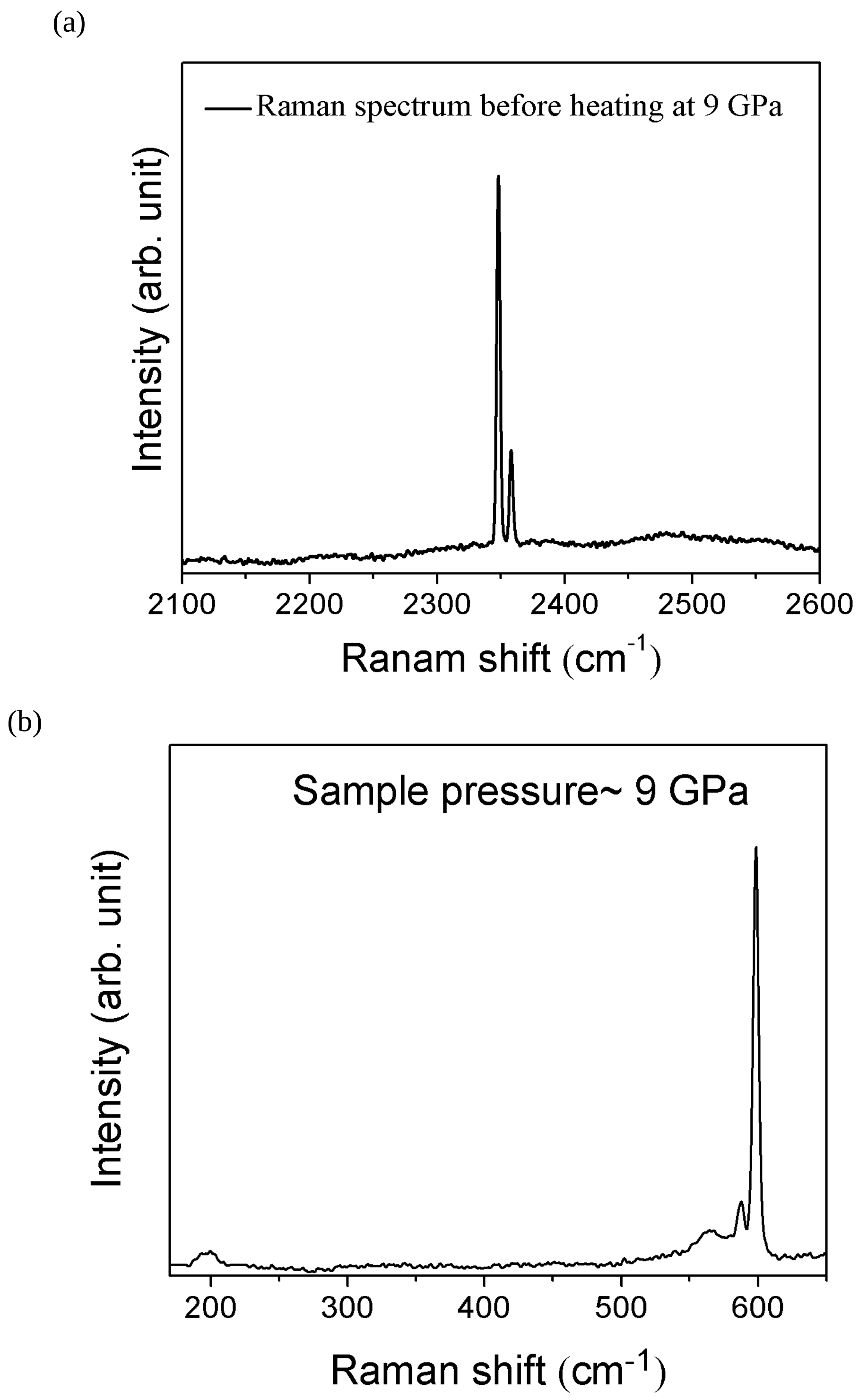

***Fig. 2.13**: a) Raman spectra of (a) Ga +N_2 system before laser heating at 9 GPa at ambient temperature shows the Raman active nitrogen modes and (b) Temperature quenched heated sample after laser heating at 9 GPa and 1925 K.*

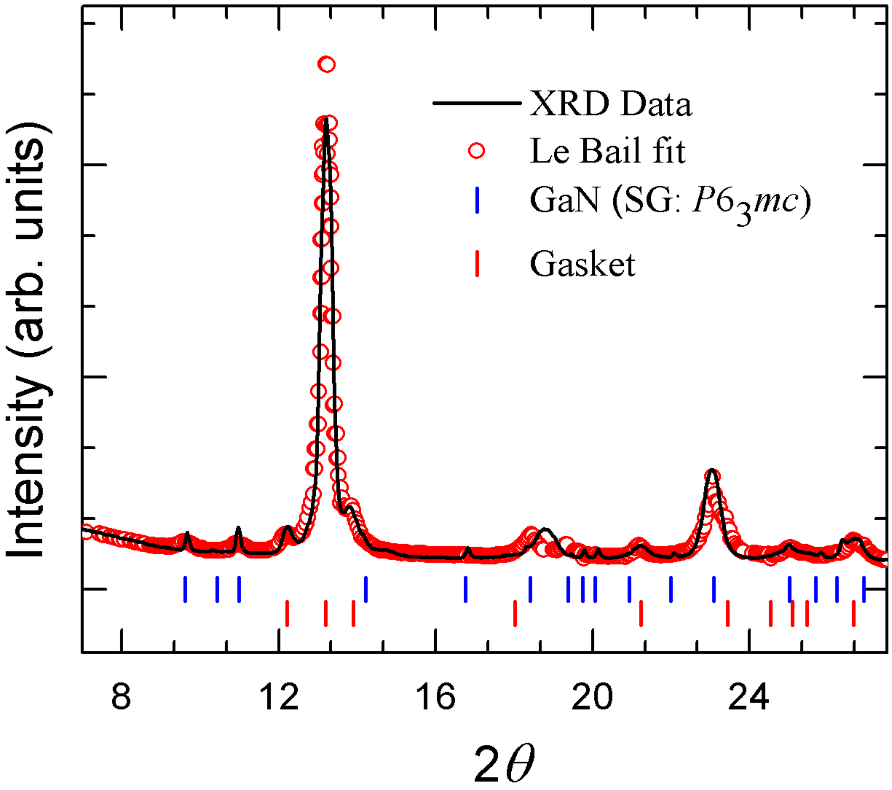

Fig. 2.14: *Le Bail fit ADXRD pattern of the retrieved sample after laser heating.*

2.3.1.2 HPHT Synthesis of γ-Mo_2N

Mao-Bell type DAC in conjunction with LHDAC facility was employed for synthesis of γ-Mo_2N. A molybdenum foil of thickness ~10 µm and diameter ~100 µm, along with a few ruby balls (~10 µm), was loaded into a 150 µm diameter hole of a hardened stainless steel gasket preindented to a thickness of 60 µm. Liquid nitrogen was loaded in the DAC by cryogenic immersion method. It acted as the PTM as well as reactant for the nitride synthesis. The DAC was pressurized to 7 GPa. Pressure measurement was carried out using ruby fluorescence method. On focusing the NIR laser on the molybdenum foil, bright thermal radiation, emitted by the heated sample, was observed on the visual CCD (CCD2) indicating good coupling of the sample with the laser. The sample was laser heated at 30 W input laser power for 600 sec. A water-cooling jacket arrangement for the piston cylinder of the DAC prevented the DAC body from heating up. The sample temperature was determined to be 2000 K by spectroradiometry. Raman spectrum of the pressurized sample was recorded both before and after heating. Raman measurements prior to heating as depicted in Fig. 2.15a shows only nitrogen modes. Raman spectrum of the post laser heated sample as shown in Fig. 2.15b is in good agreement with that of Bull *et al* [37] indicating the synthesis of γ-Mo_2N. Although ADXRD measurements could not be carried out on the post heated sample, the synthesis of γ-Mo_2N is clearly inferred from the Raman data.

(a)

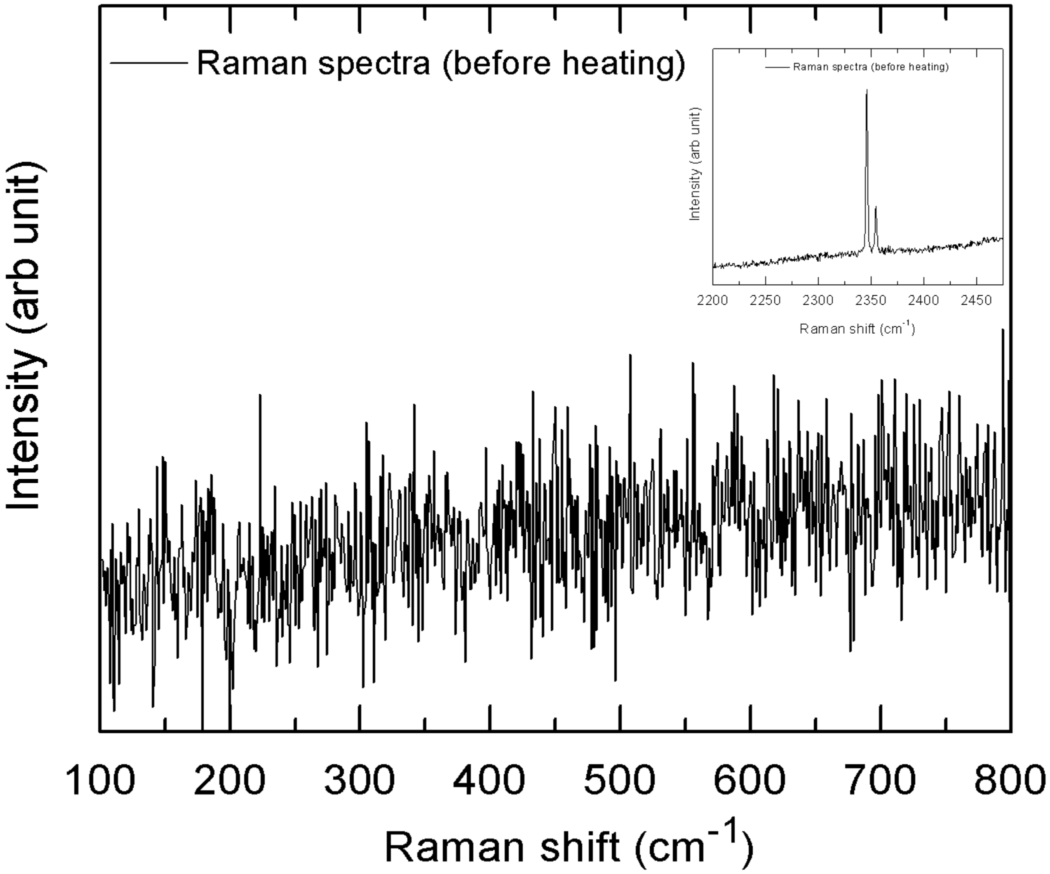

(b)

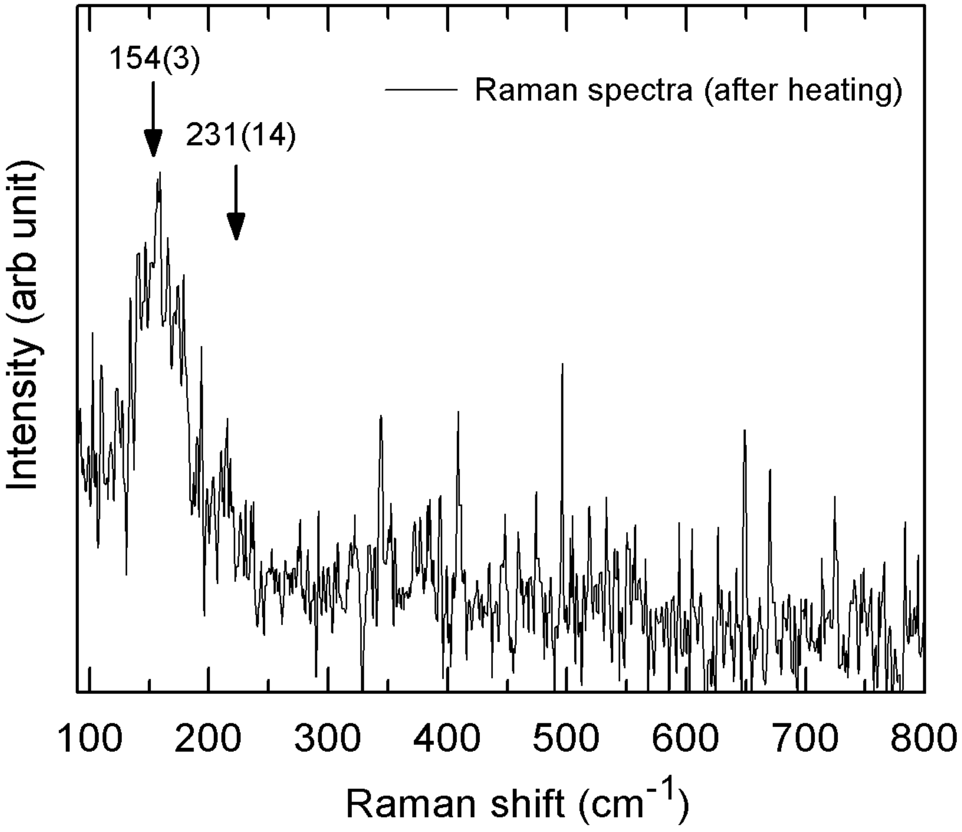

Fig. 2.15: *Raman spectra of (a) Mo +N_2 system before laser heating at 7 GPa at ambient temperature. Inset shows the Raman active nitrogen modes and (b) recovered heated sample after laser heating at 7 GPa and 2000 K.*

2.3.2 Melting curve of KBr up to 24 GPa

The determination of melting curve of material under compression is technically difficult and challenging both for experimentalists and theorists. There have been significant discrepancies among the various reported studies on the melting curves of important materials [38]. Furthermore, the high pressure melting behaviours of compounds are relatively unexplored. Hence knowledge of the atomic bond dependent melting behaviour of solids can provide vital inputs for future theoretical models.

In the present study we have carried out high pressure melting experiments on the alkali halide "KBr". The high pressure behaviour of KBr is fairly simple with only two known phases *viz.*, B1 phase (*SG: Fm-3m*) in the pressure range of ambient to 2.3 GPa and a B2 phase (*SG: Pm-3m*) at higher pressures [39]. The high pressure melting behaviour of KBr upto 4.0 GPa has been reported using piston cylinder apparatus and Pt/Pt10%Rh thermocouple for temperature measurements [40]. Boehler *et al* have reported high pressure melting study of KBr using LHDAC up to 35 GPa wherein the onset of melting was detected by an abrupt change in the IR laser absorption by the sample [41]. However the limitation of this technique is that it does not distinguish between solid-solid and solid-liquid transition, as the sample absorption may also change upon solid-solid transition. Hence in the present study, laser speckle method, which distinguishes between solid-solid and solid-liquid transition, has been employed to investigate the high pressure melting behaviour of KBr [29].

High pressure LHDAC based melting experiments on KBr was carried out using a Mao-Bell type DAC with a 400 µm culet. A tungsten gasket preindented to 50 µm with a 150 µm central hole formed the sample chamber and KBr itself served as the PTM as well as the buffer medium for thermal insulation. A tungsten (W) foil (~ 80 µm diameter, ~ 10 µm thickness) loaded along with the sample acted as the NIR laser coupler. Pressure measurement was carried out by ruby fluorescence method at ambient temperature. Thermal emission spectra was collected in fine steps of input laser power using the crossed polarizers (PBS1 and PBS2) and λ/2 waveplate (WP) assembly together with a video recording of the speckle pattern to determine the onset of melting. Temperature measurement was carried out by spectroradiometry. For accurate results, temperature was measured at the onset of laser speckle motion during melting while increasing the laser power and at the disappearance of laser speckle motion during freezing while decreasing the laser power. The reported melting temperature is the mean value of temperatures measured for multiple melting and freezing cycles at a given pressure. Figure 2.16 shows a typical Planck fit to the collected incandescent spectrum. The variation of melting temperature with pressure as shown in Fig. 2.17 is in good agreement with the previously reported result [41]. The present work thus provides the melting curve of KBr using a complimentary melting temperature detection method and hence the results provide a standardized melting curve of KBr that can be used for validation of theoretical models for ionic compounds.

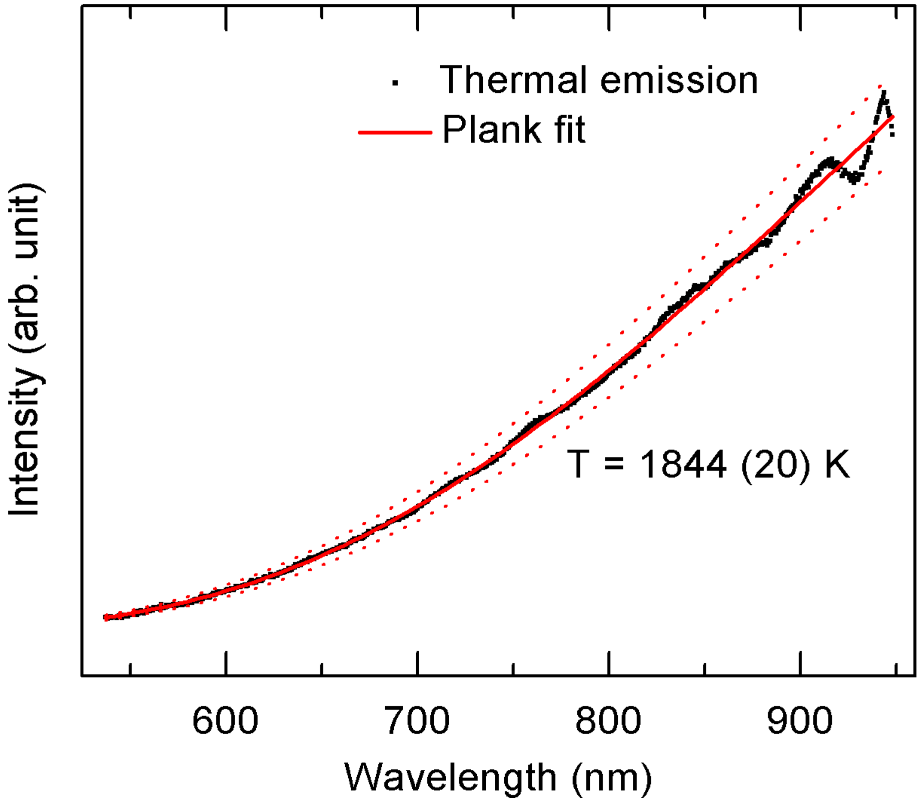

Fig. 2.16: *Planck fit to a typical incandescent spectrum of laser heated KBr corrected for instrument spectral response. The fitted gray body curve (solid red line) yields a temperature of 1844 K. The red dotted curves indicate the confidence interval yielding a temperature uncertainty of 20 K.*

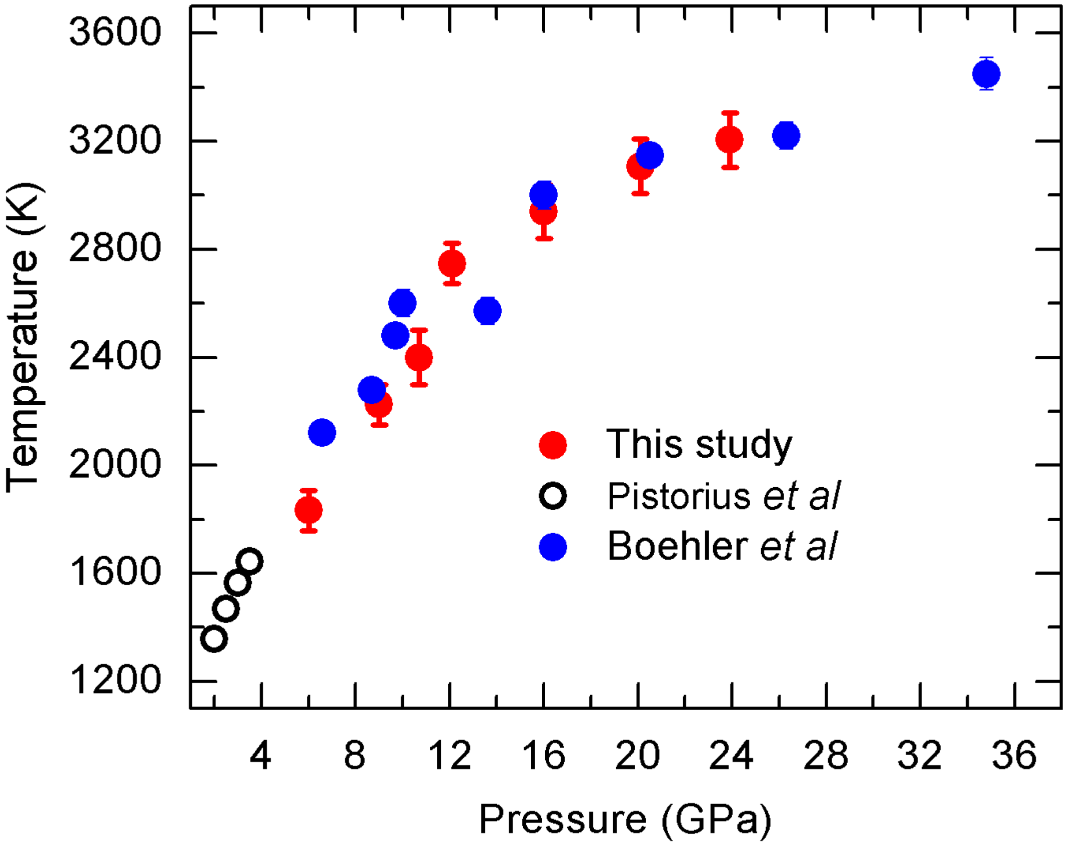

Fig. 2.17: *Experimental melting curve of KBr upto 24 GPa. The available literature data are shown in the figure for comparison.*

2.4. Conclusions

A state of the art laser heated diamond anvil cell facility has been commissioned at High Pressure & Synchrotron Radiation Physics Division, Bhabha Atomic Research Centre and optimized for carrying out material synthesis and melting studies on materials at high pressures.

References

[1] Y. Meng, G. Shen and H. K. Mao, *J. Phys.: Condens. Matter* **18,** S1097 (2006).

[2] N. N. Patel, S. Meenakshi and S. M. Sharma, *AIP Conf. Proc*. **1591**, 664 (2014).

[3] R. Boehler, *Hyperfine Interactions* **128**, 307 (2000).

[4] D. Errandonea, *J. Phys. Chem. Solids* **67**, 2017 (2006).

[5] S. Meenakshi, V. Vijayakumar and B. K. Godwal, *Indian J. of Pure Appl. Phys.* **44**, 440 (2006).

[6] S. Petitgirard, A. Salamat, P. Beck, G. Weck and P. Bouvie, *J. Synchrotron Rad.* **21**, 89 (2014).

[7] N. Subramanian, N. V. Chandra Shekar, N. R. Sanjay Kumar and P. Ch. Sahu, *Current Science* **91**, 175 (2006).

[8] J. F. Lin, M. Santoro, V. V. Struzhkin, H. K. Mao and R. J. Hemley, *Rev. Sci. Instrum*.**75**, 3302 (2004a).

[9] A. F. Goncharov and J. C. Crowhurst, *Rev. Sci. Instrum*. **76**, 063905 (2005).

[10] R. Boehler, H. G. Musshoff, R. Ditz, G. Aquilanti and A. Trapananti, *Rev. Sci. Instrum*. **80**, 045103 (2009).

[11] J. D. Barnett, S. Block and G. J. Piermarini, *Rev. Sci. Instrum*. **44**, 1(1973).

[12] G. Shen, M. L. Rivers, Y. Wang, S. R. Sutton, *Rev. Sci. Instrum*. **72**, 1273(2001).

[13] S. Anzellini, A. Dewaele, M. Mezouar, P. Loubeyre and G. Morard, *Science* **340**, 464 (2013).

[14] V. B. Prakapenka, A. Kubo, A. Kuznetsov, A. Laskin, O. Skurikhin, P. Dera, M. L. Rivers and S. R. Sutton, *High Press. Res*. **28**, 225 (2008).

[15] R. Jeanloz and D. L. Heinz, *J De Physique* **C8** 83 (1984).

[16] R. Boehler, *Geophys. Rev. Lett.* **13**, 1153 (1986).

[17] J. Deng, Z. Du, L. R. Benedetti and K. K. M. Lee, *J. Appl. Phys*. **121**, 025901(2017).

[18] J. Gilvarry, *Phys. Rev. Lett*. **16**, 1089 (1966).

[19] N. Raschevsky, *Z. Physik* **40**, 214 (1927).

[20] K. Herzfeld and M. Mayer, *Phys. Rev*. **46**, 995 (1934).

[21] J. Lennard-Jones and A. Devonshire, *Proc. Natl. Acad. Sci.* **169**, 317 (1938).

[22] L. Brillouin, *Phys. Rev*. **54**, 916 (1938).

[23] P. Lazor, G. Shen and S. K. Saxena, *Phys. Chem. Minerals* **20**, 86 (1993).

[24] R. Boehler, N. V. Bargen and A. Chopelas, *J. Geophys. Res*. **95**, 21731(1990).

[25] L. Yang, A. Karandikar and R. Boehler, *Rev. Sci. Instrum*. **83**, 063905 (2012).

[26] K. Ohta, Y. Kuwayama, K. Hirose, K. Shimizu and Y. Ohishi, *Nature* **534**, 95(2016).

[27] R. Boehler, *Nature* **363**, 534(1993).

[28] D. Errandonea, B. Schwager, R. Ditz, C. Gessmann, R. Boehler and M. Ross, *Phys. Rev. B* **63** 132104 (2001).

[29] M. Ross LLNL-TR-406604, https://e-reports-ext.llnl.gov/pdf/364495.pdf (2008).

[30] L. J. Swartzendruber, *Bull. Alloy Phase Diagrams* **3**, 161(1982).

[31] W. M. Haynes, ed., *CRC Handbook of Chemistry and Physics*, CRC Press/Taylor and Francis, Boca Raton, FL, 95th Edition (2015).

[32] A. Friedrich, B. Winkler, E. A. J. Arellano and L. Bayarjargal, *Materials* **4**, 1648 (2011).

[33] E. H. Bordon, R. Riedel, A. Zerr, P. F. McMillan, G. Auffermann, Y. Ports, W. Bronger, R. Kniep and P. Kroll, C*hem. Soc. Rev*. **35**, 987 (2006).

[34] X. Zhao and K. J. Range, *J. Alloys Comp.* **296**, 72 (2000).

[35] E. Soignard, P. F. McMillan, T. D. Chaplin, S. M. Farag, C. L. Bull, M. S. Somayazulu and K. Leinenweber, *Phys. Rev. B* **68**, 132101 (2006).

[36] H. D. Xiao, H. L. Ma, C. S. Xue, J. Ma, F. J. Zong, X. J. Zhang, F. Ji and W. R. Hu, *Materials Chemistry and Physics* **88**, 180–184 (2004).

[37] C. L. Bull, T. Kawashima, P. F. McMillan, D. Machon, O. Shebanova, D. Daisenberger, E. Soignard, E.T. Muromachi and L. C. Chapon, *J. Solid. Stat. Chem.* **179**, 1762 (2006).

[38] J. R. Fuertes, A. Karandikar, R. Boehler and D. Errandonea, *Phys. Earth and Planetary Interiors* **181**, 69 (2010).

[39] A. Dewaele, A. B. Belonoshko, G. Garbarino, F. Occelli, P. Bouvier, M. Hanfland and M. Mezouar, *Phys. Rev.* ***B*** **85**, 214105 (2012).

[40] C. W. F. T. Pistorius, *J. Phys. Chem. Solids* **26**, 1543 (1965).

[41] R. Boehler, M. Ross and D. B. Boercker, *Phys. Rev. B* **53**, 556 (1996).

Chapter 3

High Pressure Melting Curve of Osmium

Osmium (Os), which adopts a hexagonal closed packed structure, is one of the unique element of the periodic table with exceptional properties, such as highest density among elements, very high cohesive energy, high melting temperature and a bulk modulus that is almost comparable to that of diamond under ambient temperature and pressure conditions [1-10]. These superlative properties of osmium render it suitable for a variety of applications where durability is the foremost requirement *e.g.,* electrical contacts, wear-resistant machine components, tips for high-quality ink pens, medical devices and armor-piercing weapon shells. Its extraordinarily high bulk modulus and low thermal expansion also make osmium a potential candidate for the synthesis of promising superhard materials [11].

The bulk modulus of Os was reported experimentally by Cynn *et al* to be 462 GPa, which is higher than that of diamond (B_0 = 446 GPa) [3]. However first principles calculations and reanalysis of the experimental data of Cynn *et al* by Joshi *et al* dismissed this claim and showed that the bulk modulus of Os is comparable with, but not more than that of diamond [3, 12]. Subsequent experimental and theoretical studies have reported a bulk modulus for Os ranging from 392 to 476 GPa suggesting that the bulk modulus of Os is large, but still smaller than that of diamond [4-7, 12-14]. The interest in Os has been further impelled by the observation of a discontinuity in the pressure derivative of the axial ratio *(c/a)* around 25 GPa, which has been attributed to a pressure-induced isostructural Lifshitz transition [4, 15, 16]. A recent experimental and theoretical study however reports that Os retains its hexagonal close-packed structure to over 770 GPa with anomalies in the axial ratio at 150 and 440 GPa [2]. These anomalies have been attributed to a topological change in the Fermi surface for valence electrons and to an electronic transition associated with the pressure induced interaction between core electrons respectively [2]. Subsequent synchrotron based angle dispersive x-ray diffraction (ADXRD) study up to 207 GPa however do not indicate any anomaly in c/a ratio at 25 and 150 GPa [1].

Despite these interesting observations and extensive high pressure investigations on Os, to the best of our knowledge, there have been no experimental report till date on the high pressure melting curve $T_m(P)$ of Os. It may be noted that the ambient pressure experimental melting temperature of Os with 99.5 % and 99.7% purity was reported to be 3283 +/- 10 K and 3318 +/- 30 K respectively [17, 18]. Using available literature values of melting temperature as a function of purity, Arblaster estimated the ambient pressure melting temperature of Os with 100% purity to be 3400 +/- 50 K [19]. Theoretical studies have also been reported to establish the melting curve of Os at high pressures and to obtain its melting slope using various approaches [13, 20-24]. Among them, the most recent *ab initio* quantum molecular dynamic (QMD) simulations using Z method have computed its melting point at eight different pressure points up to 500 GPa. [13]. Theoretical melting curve of Os up to 800 GPa has been reported using first-principles calculations with a prediction of the shock melting around 450 GPa and 9200 K [22]. This value is much smaller than the calculated melting temperature of 13400 K reported by Z method [13].

Establishment of an experimental melting curve for osmium would resolve the observed discrepancies in the various reported theoretical melting studies. The present chapter reports the experimental melting curve of osmium up to 35 GPa using an air cooled Yb fibre laser based laser heated diamond anvil cell (LHDAC) facility [25].

3.1 Experimental Details

High pressure LHDAC based melting experiments were performed using an indigenously developed Mao-Bell type DAC having 400 µm culet [25]. Sample of thickness ~10 µm was obtained by pressing a small flake of Os foil (purity 99.8%) between the two culets of DAC. The sample chamber, which is a tungsten gasket with pre-indentation thickness of 50 µm with a 150 µm diameter hole, was completely filled with Al_2O_3 powder (purity, 99.9%), which was dried in a furnace at 400 ^oC for 24 hrs prior to loading. The DAC was then pressed for compaction. A shallow pit was then scooped in the Al_2O_3 layer into which Os foil of size ~100 µm was loaded (as seen in Fig. 3.1). A thin layer of Al_2O_3 was placed over the sample to ensure thermal insulation of the sample from the diamond. A few ruby balls of ~10 µm in diameter were also placed in the sample chamber for pressure calibration. Pressure measurement was carried out using ruby fluorescence method at room temperature. Temperature measurement was carried out by spectroradiometry in the 500-900 nm wavelength range, by fitting the spectral intensity, collected from a ~3 µm area in the centre of the hot spot, to the Planck's blackbody radiation law, as given in Eq. 2.1 of Section 2.2.4, assuming a gray body approximation *i.e.*, invariance of emissivity over the measured wavelength range.

The melting temperature at each pressure was determined using laser speckle method by illuminating the laser heated spot with a defocused green laser [25]. The onset of melting is indicated by the motion in laser speckle pattern, resulting from local changes in the refractive index. The accurate melting temperature was determined by collecting the thermal emission spectra in fine steps of input laser power using two crossed polarizers and a λ/2 waveplate assembly along with a video recording of the speckle pattern [25]. The reported melting temperature at each pressure is the arithmetic mean of melting temperatures measured for multiple heating and cooling cycles. Raman measurement was carried out on the post heated sample to ensure the chemical inertness of the Al_2O_3 at HPHT.

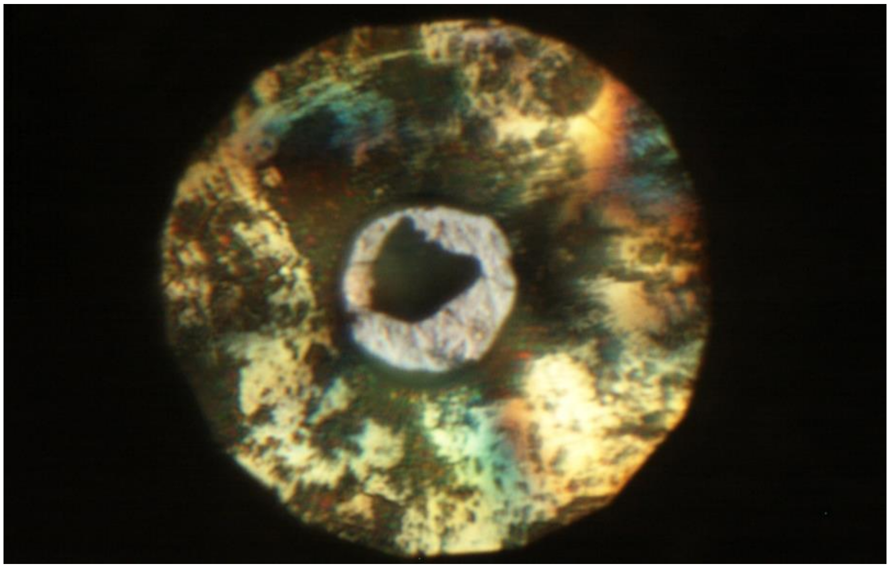

Fig. 3.1: *Image of sample chamber containing osmium, ruby ball and PTM.*

3.2 Results and Discussion

Figure 3.2 shows pressure dependent melting curve of Os obtained from the present measurements together with the available theoretical melting curves for comparison [13, 22]. The ambient melting temperature (T_0) for the present measurements was considered as 3400 +/- 50 K [19]. Simon-Glatzel equation as described in Eq. (3.1) was used to fit the experimental melting data.

$$T_m = T_0\left(1+\left(\frac{P-P_0}{A}\right)\right)^{\left(\frac{1}{C}\right)} \qquad (3.1)$$

where T_m and T_0 are melting temperatures at the experimental pressure point (P) and at ambient pressure (P_0) respectively and A and C are the Simon-Glatzel fitting constants. The fitting constants (A and C) and ambient melting temperature (T_0) obtained for the present measurements are tabulated in Table 3.1 along with the fitting parameters of reported theoretical melting curves [13, 22].

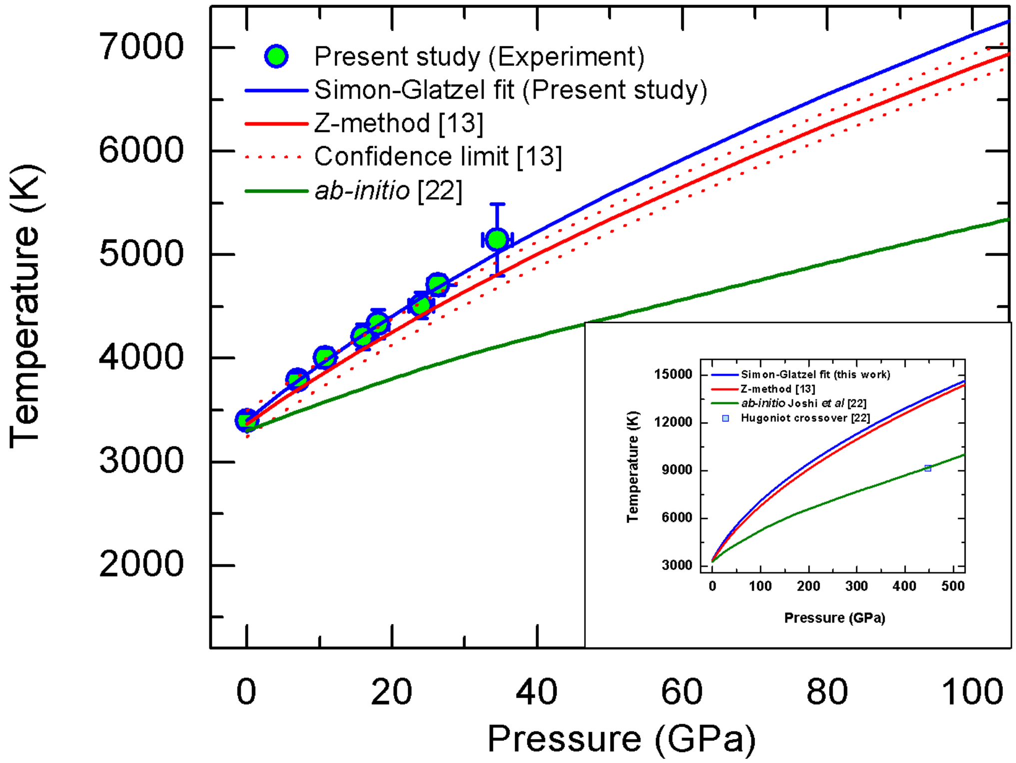

***Fig. 3.2**: Comparison of the experimental melting curve of Os and the corresponding Simon-Glatzel fit in pressure-temperature coordinates with the various theoretical formalisms described in the text. The inset shows the corresponding melting curve up to 500 GPa showing the Hugoniot melting point of Ref. [22].*

Table 3.1: Comparison of the Simon-Glatzel fit parameters obtained in the present study with that reported by various theoretical formalisms described in the text.

	T_0 in (K)	Simon-Glatzel Fit Parameters		T_m at 450 GPa (K)
		A in (GPa)	C	
Present study	3405(26)	29.2(113)	2.01(56)	13700
Z- Method Ref.[13]	3370(75)	36.065	1.89	13400
Ab-initio Ref. [22]	3463(67)	101.9(107)	1.67(6)	9200

It may be noted that the smooth behaviour of the experimental curve rules out any solid-solid transition in the sample. Furthermore, the laser speckle technique employed for detecting the onset of melting reiterates the absence of any solid-solid transition in osmium up to the melting temperature. Interestingly, as evident from Fig. 3.3, the melting line of Os is seen to cross that of W around 6 GPa making it the most refractory metal [27, 28]. Table 3.2 compares the melting slope of Os with that of some reported hcp phase metals [28-31]. The melting slope obtained in the present study has been tabulated and compared with the available theoretical melting slopes in Table 3.3 [13, 20-24]. It may be noted that Kulyamina *et al* have extrapolated the available experimental isobaric heating data on Os and obtained their melting slope [20, 21]. In view of the fact that experimental values of ΔV_m and ΔS_m are not available, their usage of estimated values could be the possible reason for deviation of their melting slope from the present study.

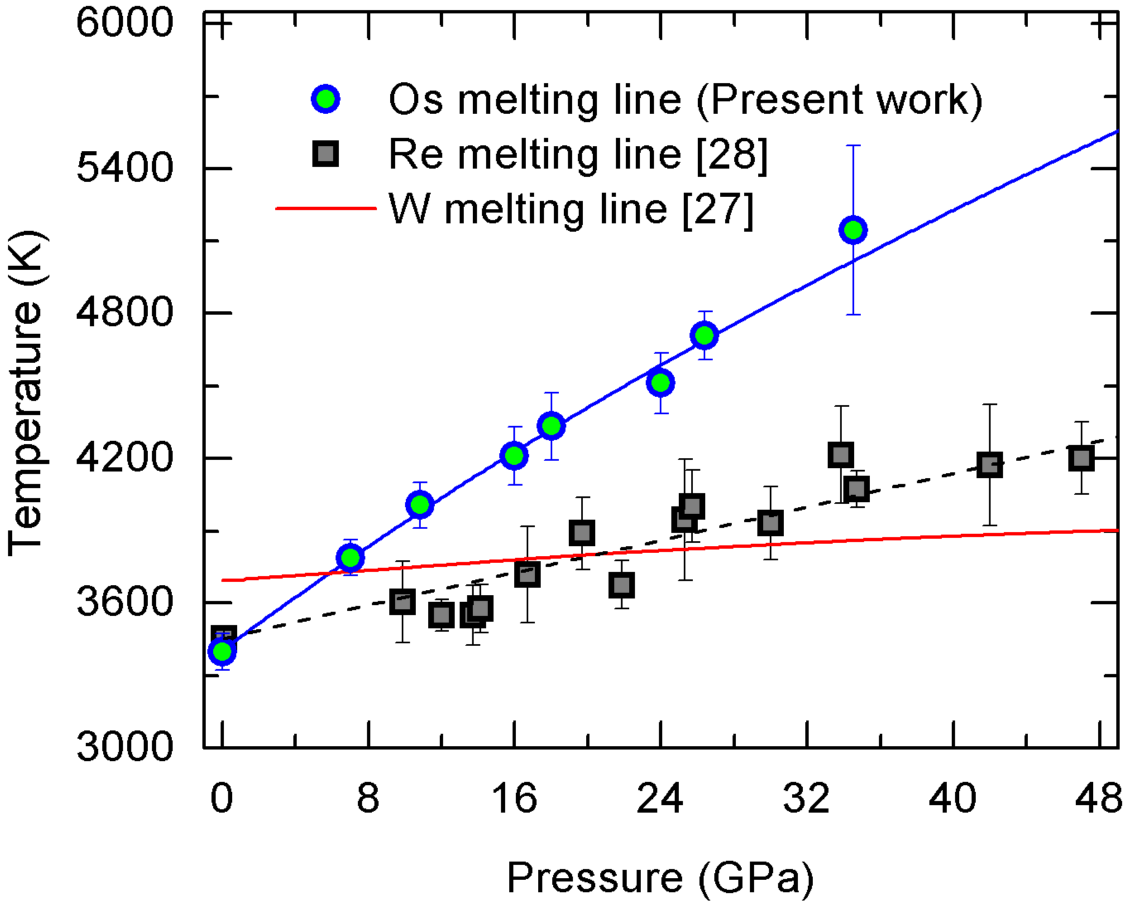

***Fig. 3.3:** Comparison of melting curve of Os with Re [28] and W [27].*

Table 3.2: Comparison of ambient pressure melting temperature and melting slope of some hcp phase metals: Os [present study], Re [28], Mg [29], Zn [30] and Cd [31].

	Os	Re	Mg	Zn	Cd
Melting point (K)	3400	3453	923	690	594
Melting slope (K GPa^{-1})	58	17	6	50	45

Table 3.3: Experimental melting slope compared with that reported by various theoretical formalisms described in the text.

	Present study	Ref. [13]	Ref. [22]	Ref. [21]	Ref. [23]	Ref. [24]
$\left(\frac{\partial T_m}{\partial P}\right)_{P=0}$ (K GPa^{-1})	58	49.5	20.3	40.4	65	53.4

It is evident from Fig. 3.2 that the melting curve determined by Z method shows good agreement within theoretical and experimental errors with that obtained in the present study. However, the *ab initio* melting curve of Joshi *et al,* when compared with the extrapolated Simon-Glatzel fit of the present study, is seen to underestimate the melting temperature [22]. The extrapolated melting temperature at 450 GPa, described as the Hugoniot melting point, is listed in Table 3.1. It may be noted that Burakovsky *et al* have attributed the underestimation of the melting temperatures by Joshi *et al* to their unphysical choice for the density dependence of the Grüneisen parameter [13, 22].

This implies that the determination of Grüneisen parameter ($\gamma(\rho)$) is important to get an insight into the melting phenomenon. Dongquan and Wanxing have reported an analytical model $\gamma(\rho) = \gamma_0 (\rho_0/\rho) + (2/3)(1- \rho_0/\rho)^{\delta}$, where $\gamma(\rho)$ approaches the value (2/3) at very large compression and the equation reduces to $\gamma\rho \sim$ constant at small compression [32]. Recently Burakovsky *et al* [33] proposed an analytical model given as

$$\gamma(\rho) = \frac{1}{2} + \frac{\gamma_1}{\rho^{1/3}} + \frac{\gamma_2}{\rho^{q}} \tag{3.2}$$

which asymptotically reduces to (1/2) as ρ→∞. The value of (1/2) for γ(ρ), at very large compression, is obtained on the assumption that crystal reduces to one component plasma (OCP) when density increase, upon compression, reaches 10 fold or higher. Using this model, γ(ρ) was computed by considering three limiting case of γ(ρ) and using Lindemann melting criteria as given in Eq. (3.3).

$$\gamma(\rho) = \frac{1}{2}\frac{d\ln T_m(\rho)}{d\ln\rho} + \frac{1}{3} \tag{3.3}$$

Based on the analytical model described in Eq. 3.2, γ(ρ) has been determined using two approaches in the present study. In the first approach, model parameters (γ_1, γ_2 and q) were calculated using the experimental melting slope (dT_m/dP), as determined by the Simon- Glatzel fit, by imposing the following three conditions *viz.,*

Condition 1: For ρ→∞, γ(ρ) → OCP limit and Lindemann melting criteria reduces to

$$\exp\left\{\frac{6\gamma_1}{\rho_m^{(1/3)}} + \frac{\gamma_2}{q\rho_m^{(q)}}\right\} = \left(\frac{4\pi}{3V_m}\right)^{1/3}\left(\frac{e^2Z^2}{KT_m}\right)\frac{1}{\Gamma_m} \tag{3.4}$$

where V_m, ρ_m T_m, K, e, Z and Γ_m are unit cell volume at melt, density at melt, melting temperature of Os, Boltzmann constant, electron charge, atomic number and OCP coupling parameter of Os at melt respectively. The value of the OCP coupling parameter at melt (Γ_m) for Os was considered as 175 in the present study [34, 35].

Condition 2: At ambient pressure and temperature, the experimental value of γ(ρ) is 2.12 [36]. Thus Eq. (3.2) reduces to

$$\frac{1}{2}+\frac{\gamma_1}{\rho_0^{1/3}}+\frac{\gamma_2}{\rho_0^{\,q}}=2.12 \tag{3.5}$$

where (ρ_0 = 22.59 g/cm^3) is the density of Os at ambient condition [19]

Condition 3: Equating γ (ρ) from Eqs. (3.2) and (3.3) at melting point, we get

$$\frac{1}{2}+\frac{\gamma_1}{\rho_m^{1/3}}+\frac{\gamma_2}{\rho_m^{\,q}}=\frac{1}{2}\left(\frac{\rho_m}{T_m}\right)\left(\frac{dT_m}{d\rho_m}\right)+\frac{1}{3} \tag{3.6}$$

where ρ_0, ρ_m, T_m are the density of Os at ambient temperature, density of Os at melting point and melting temperature of Os respectively. The melting slope ($dT_m/d\rho_m$) was determined from Eq. (3.7) using the experimental melting slope (dT_m/dP) as determined from the Simon- Glatzel fit

$$\frac{dT_m}{d\rho_m}=\left(\frac{B_m}{\rho_m}\right)\left(\frac{dT_m}{dP}\right) \tag{3.7}$$

where B_m and dT_m/dP are ambient pressure bulk modulus at melt and the experimental melting slope of 58 K/GPa respectively. The value of ρ_m and B_m were determined from temperature modified values of V_0 and B_0 from Eqs. (3.8) and (3.9) respectively

$$V(T)=V_0\exp\left(\alpha_0 T+\frac{\alpha_1}{2}T^2\right) \tag{3.8}$$

$$B(T)=B_0+\frac{dB_0}{dT}(T-300) \tag{3.9}$$

where α_0 is the ambient pressure thermal expansion coefficient, α_1 is the first temperature derivative of thermal expansion coefficient, B_0 is the ambient temperature bulk modulus and dB_0/dT is the temperature derivative of the bulk modulus. The values of α_0, α_1, B_0 and dB_0/dT were considered as 1.48×10^{-5} K^{-1}, 5.2×10^{-9} K^{-2}, 421 GPa and -0.054 GPa K^{-1} respectively [6]. The values of model parameters (γ_1, γ_2 and q) determined by solving Eqs. (3.4), (3.5) and (3.6) simultaneously are tabulated in Table 3.4.

In this context it may be noted that, in absence of any report for experimental melting slope for Os, Burakovsky *et al* had assumed that γ_1 satisfies the $\gamma_1 = \gamma_1$ (Z) systematic, where Z is the atomic number, and hence fixed the value of γ_1 as 3.06 $(g/cm^3)^{1/3}$ for solving the Eqs. (3.4) and (3.5) simultaneously [33]. This essentially implies that the computation of their model parameters (γ_1, γ_2 and q) were based on *Condition 1* and *Condition 2* only. In order to eliminate the OCP dependence on the model parameters, as a second approach, we have applied *Condition 2* and *Condition 3* together with the assumption of γ_1 as 3.06 $(g/cm^3)^{1/3}$. This essentially implies that, except for γ_1, the computation of the other two model parameters *viz.*, γ_2 and q, as tabulated in Table 3.4, are based on experimental data. The variation of $\gamma(\rho)$ as a function of ρ_0/ρ is shown in Fig. 3.4 wherein two regions have been marked. In region I, it is observed that the curves obtained from both the approaches considered in present study (curves (a) and (b)) overlap. They are however deviated from the theoretically calculated curve (c) in the ρ_0/ρ range of 0.5 to 1.0 [13]. In view of the fact that the value of γ_1 computed in the present study is same as that considered by Burakovsky *et al* we conclude that the variation of $\gamma(\rho)$ in this region is predominantly dependent on (γ_2/ρ^q), which is the third term of Eq. (3.2) [13]. It may also be noted that the value of (γ_2/ρ^q) in the present study differs from that obtained by Z method by ~22 % at ambient density ($\rho_0/\rho = 1$) [13].

Table 3.4: Comparison of the model parameters obtained in the present study with Ref. [13].

Model parameter	Present study		Ref. [13]
	1st approach	2nd approach	
γ_1 in (g/cm^3)$^{1/3}$	3.063	3.060	3.060
γ_2 in (g/cm^3)^q	1.35×10^8	1.31×10^8	4.1×10^{15}
q	6.20	6.19	11.8

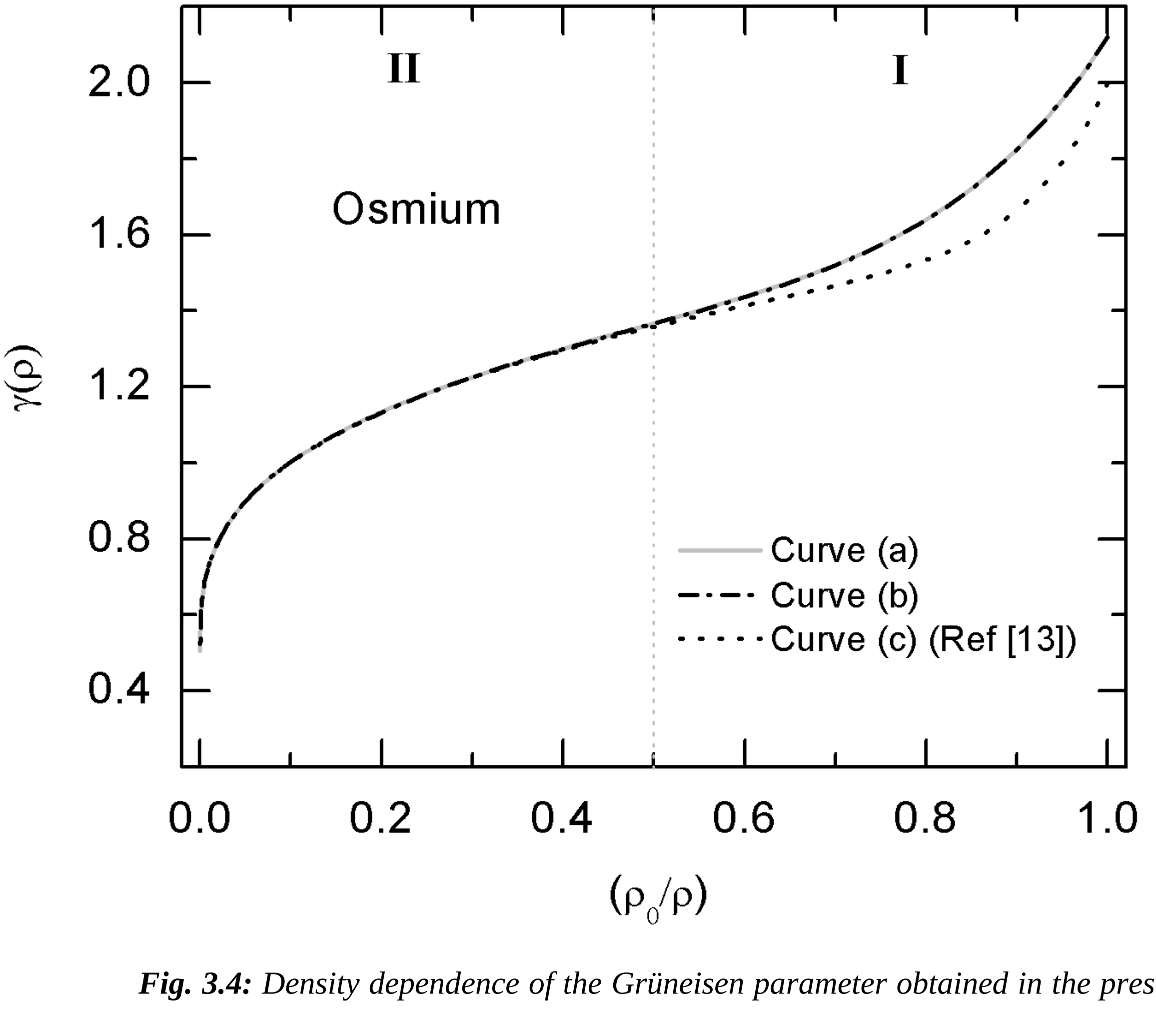

Fig. 3.4: *Density dependence of the Grüneisen parameter obtained in the present study compared with that of Ref. [13].*

In view of this, the coincidence of the three curves (a, b and c) in Region II leads us to conclude that $\gamma(\rho)$ in this region is virtually independent of higher order density term, *i.e.*, (γ_2/ρ^q). The above observations, in conjunction with the reported Z dependence of γ_1, lead us to conclude that the Grüneisen parameter $\gamma(\rho)$ is dependent only on Z at very high compression [33].

3.3 Conclusions

The melting curve of Os has been determined up to 35 GPa and 5800 K using the laser-heated diamond anvil cell experiments employing laser speckle method for accurate detection of onset of melting. The density dependence of Grüneisen parameter ($\gamma(\rho)$) has been determined analytically, using the experimentally obtained melting slope, by adopting two approaches. The study leads us to conclude that the Grüneisen parameter is dependent only on Z at very high compression. The experimental melting curve obtained in the present study would provide an important database for a definitive understanding of the phase diagram of Os and for developing and testing condensed matter theories describing the equation of state, melting and phase stability, which could be of immense fundamental scientific interest.

References

[1] C. S. Perreault, N. Velisavljevic and Y. K. Vohra, *Cogent Phys.*, **4**, 1376899 (2017).

[2] L. Dubrovinsky, N. Dubrovinskaia, E. Bykova, M. Bykov, V. Prakapenka, C. Prescher, K. Glazyrin, H. P. Liermann, M. Hanfland, M. Ekholm, Q. Feng, L. V. Pourovskii, M. I. Katsnelson, J. M. Wills and I. A. Abrikosov, *Nature*, **525**, 226 (2015).

[3] H. Cynn, J. E. Klepeis, C. S.Yoo and D. A.Young, *Phys. Rev. Lett.*, **88**, 2401 (2002).

[4] F. Occelli, D. L. Farber, J. Badro, C. M. Aracne, D. M. Teter, M. Hanfland, B. Canny and B. Couzinet, *Phys. Rev. Lett.*, **93,** 095502 (2004).

[5] T. Kenichi, *Phys. Rev. B*, **70,** 012101 (2004).

[6] M. M. Armentrout and A. Kavner, *J. Appl. Phys.*, **107**, 093528 (2010).

[7] B. K. Godwal, J. Yan, S. M. Clark and R. Jeanloz, *J. Appl. Phys.* **111**, 112608 (2012).

[8] G. A. Voronin, C. Pantea, T. W. Zerda, L. Wang and Y. Zhao, *J. Phys. Chem. Solids* **66**, 706 (2005).

[9] B. R. Sahu and L. Kleinman, *Phys. Rev. B* **72**, 113106 (2005).

[10] M. Hebbache and M. Zemzemi, *Phys. Rev. B* **70**, 224107 (2004).

[11] J. C. Zheng, *Phys. Rev. B* **72**, 052105 (2005).

[12] K. D. Joshi, G. Jyoti and S. C. Gupta, *High Press. Res.*, **23**, 403 (2003).

[13] L. Burakovsky, N. Burakovsky and D. L. Preston, *Phys. Rev. B*, **92**, 174105 (2015).

[14] Y. Liang and Z. Fang, *J. Phys.: Condens. Matter* **18**, 8749 (2006).

[15] Y. Ma, T. Cui, L. Zhang, Y. Xie, and G. Zou, J. S. Tse, X. Gao and D. D. Klug, *Phys. Rev. B* **72**, 174103 (2005).

[16] D. Koudela, M. Richter, A. Möbius, K. Koepernik and H. Eschrig, *Phys. Rev. B* **74**, 214103 (2006).

[17] R. W. Douglass and E. F. Adkins, *Trans. Met. Soc. AIME*, **221**, 248 (1961).

[18] A. G. Knapton, J. Savill and R. Siddall, *J. Less Common Met.*, **2**, 357 (1960).

[19] J. W. Arblaster, *Platinum Met. Rev*. **57**, 177 (2013).

[20] E. Yu. Kulyamina, V. Yu. Zitserman and L. R. Fokin, *Technical Physics*, **62**, 68 (2017).

[21] E. Yu. Kulyamina, V. Yu. Zitserman and L. R. Fokin, *High. Temp.* **53**, 151 (2015).

[22] K. D. Joshi, S. C. Gupta and S. Banerjee, *J. Phys.: Condens. Matter*, **21**, 415402 (2009).

[23] A. R. Regel and V. M.Glazov, *Periodicheskiy zakon i fizicheskie svoistva elektronnykh rasplavov* [The Periodic Law and Physical Properties of Electronic Melts] (Nauka, Moscow, 1978).

[24] T. Gorecki, *High Temp. High Press.*, **11**, 683 (1979).

[25] N. N. Patel, M. Sunder and S. M. Sharma, *Indian J. Phys.*, in press (2018).

[26] G. Shen, M. L. Rivers, Y. Wang and S. R. Sutton, Rev. Sci. Instrum., **72**, 1273 (2001).

[27] D. Errandonea, B. Schwager, R. Ditz, C. Gessmann, R. Boehler and M. Ross, *Phys.Rev.B* **63**, 132104 (2001).

[28] L. Yang, A. Karandikar and R. Boehler, *Rev. Sci. Instrum.*, **83**, 063905 (2012).

[29] D. Errandonea, R. Boehler and M. Ross, *Phys. Rev. B* **65**, 012108 (2001).

[30] D. Errandonea, S. G. MacLeod, J. Ruiz-Fuertes, L. Burakovsky, M. I. McMahon C. W. Wilson, J. Ibañez, D. Daisenberger and C. Popescu, *J. Phys.: Condens. Matter*, in press https://doi.org/10.1088/1361-648X/aacac0.

[31] D. Errandonea, *J. Appl. Phys.*, **108**, 033517 (2010).

[32] C. Dongquan, Z. Wanxing in: *High Pressure Science and Technology, Part III*, edited by C. Homan, R. K. MacCrone, E. Whalley (North-Holland, Amsterdam, 1984) p. 247.

[33] L. Burakovsky and D. L. Preston, *J. Phys. Chem. Solids* **65**, 1581 (2004).

[34] L. Burakovsky and D. L. Preston, *Phys. Rev. E* **63**, 067402 (2001).

[35] A. Y. Potekhin and G. Chabrier, *Phys. Rev. E* **62**, 8554 (2000).

[36] C. Pantea, I. Stroe, H. Ledbetter, J. B. Betts, Y. Zhao, L. L. Daemen, H. Cynn and A. Migliori, *Phys. Rev. B* **80**, 024112 (2009)**.**

Chapter 4

Synthesis of Unconventional Stoichiometric Compounds in the K–Br System at High Pressures

Attaining the nearest closed-shell electronic configuration is the tendency of all main-group elements during chemical synthesis of compounds. Alkali atoms have one extra electron in their valence shell whereas halogen atoms lack one electron to attain the nearest noble gas valence shell electronic configurations. As a result, the alkali atoms react, via electron exchange, with the halogen group of elements. During this chemical reaction, alkali atom donates an electron to the halogen atom to form a positive ion with charge +1 and the halogen atom, by accepting one electron, becomes a negatively charged ion with charge -1. The electrostatic attraction between the alkali and halogen ion result in ionic bonding in alkali halides. Alkali halides considered as prototype ionic solids crystallize in one of the two known crystal structure *viz.,* NaCl structure (B1) having fcc lattice (SG: *Fm-3m*) with atomic positions Na at (0 0 0) and Cl at (1/2 1/2 0) or CsCl structure (B2) having simple cubic lattice (SG: *Pm-3m*) with atomic position Cs (0 0 0) and Cl (1/2 1/2 1/2), at ambient pressure and temperature. At high pressures all the alkali halides are known to transform to the B2 structure. Apart from these AX stoichiometric compounds, where A stands for alkali element and X stands for halogen, few counterintuitive alkali trihalides, *i.e.,* AX_3, were synthesized recently [1, 2]. Furthermore, higher polyhalides, *i.e.,* AX_n with $n>3$, are not known in whole alkali halogen system.

First-principles studies in recent past have proposed the formation of unconventional stoichiometries at high pressures in alkali halogen system as well as other isostructural alkali hydrogen systems [1-3]. $NaCl_3$, lithium polyhydrides and KCl_3 are notable examples of such compounds which have been synthesized at high pressures and high temperatures in the diamond-anvil cell (DAC) based experiments [1-3]. Interestingly, alkali hydrides show a high pressure behaviour similar to alkali halide, *i.e.,* B1 to B2 transition, and some of the proposed alkali polyhydrides are predicted to be high temperature superconductors [4]. The experimental realization of more such compounds and possible synthesis of higher polyhalides AX_n , where n>3, will enrich our understanding of the solid state chemistry of these simple elements and their compounds at high pressure high temperature (HPHT) conditions; especially their reactions and selectivity of different paths. With the above motivations, high temperature and high pressure studies on K-Br system was initiated.

It may be noted that, to date, potassium bromide (KBr) is the only known stoichiometric compound in the K-Br system. KBr exists in the rocksalt-type structure (B1 phase) at ambient conditions and transforms to the cesium chloride-type structure (B2 phase) above 2.0 GPa [5]. In this chapter the synthesis and characterization of two new stoichiometric compounds viz., KBr_3 and KBr_5 in K-Br systems above 2 GPa and 6 GPa at room temperature respectively have been reported. The high pressure behaviour of these compounds and high pressure and and high temperature stability of KBr_5 would be discussed.

4.1 Methodology

4.1.1 Experimental Method

High pressure experiments were performed using an indigenously developed Mao-Bell type DAC having 400 µm culet and ruby as pressure gauge. Prior to loading in the DAC, KBr powder (purity, ~ 99.99%) was dried in a furnace at 200 °C for 24 hrs. Tungsten gaskets with pre-indentation thickness of 50 µm and 150 µm diameters hole were used. A small pit was made at the centre of compacted KBr. Bromine was directly loaded into the KBr pit and the DAC was immediately closed. Due to the high vapour pressure of Br, its exact volume loaded in the DAC could not be estimated. Pressure measurements were carried out using both ruby fluorescence with pressure uncertainty of 0.1 GPa, and the equation of state (EOS) of KBr, with pressure uncertainty of 0.2 GPa [5]. High pressure angle dispersive x-ray diffraction (ADXRD) measurements were carried out at the extreme condition x-ray diffraction (ECXRD) (BL-11) beamline of Indus II synchrotron source, India [6] and Xpress beamline of the Elettra synchrotron source, Italy [7]. The sample to detector distance and the image plate orientation angle were calibrated using CeO_2 as standard. The x-ray data was collected using MAR345 detector. The 2D images were converted into intensity versus diffraction angle (2θ) plots through radial integration using FIT2D software [8]. The lattice parameters were determined by carrying out multi-phase Le Bail refinement using GSAS [9]. We could perform only Le Bail refinement due to the spotty and textured nature of the diffraction images. The typical R_p and wR_p of the Le Bail fit were 2% and 3%, respectively. Raman measurements were carried out in backscattering geometry using a triple stage micro-Raman spectrometer (Jobin Yvon T64000). This set up is equipped with a liquid nitrogen cooled CCD detector and the excitation laser has a wavelength of 532 nm.

Laser heated HPHT experiments were carried out using the LHDAC facility described in **Chapter 2** of this thesis [10]. The sample temperature was measured by spectroradiometry technique wherein the thermal radiation emitted by the hot sample is collected in a 400 nm spectral width. This technique has been described in detail in **Chapter 2** of this thesis.

4.1.2 Theoretical Method

In order to determine the stoichiometries and related crystal structures, first-principles crystal structure searches were performed using the USPEX code [11-13] in combination with VASP code [11, 14-16]. These calculations were performed at 0, 4, 8 and 12 GPa allowing all possible combinations of number of atoms in the unit cell. For most of the simulations, the number of atoms were allowed to take values from 8 to 16 in the unit cell. In principle, variable-composition searches can find out stable stoichiometries and their structures, but variable compositions calculation did not yield a structure which agreed with both Raman and XRD data of the compound formed in the second chemical reaction; hence fixed stoichiometry searches were carried out in this case. Structural search with 24 atoms (for 1:3 composition) was performed only at 15 GPa as none of the earlier structures showed agreement with post laser heated experimental data. Structural optimizations, total energy and electronic band structure calculations were done using Perdew-Burke-Ernzerhof (PBE) exchange-correlations [17]. Core and valence electrons interaction was treated by the all-electron projector augmented wave (PAW) method with K: $3p^6$, $4s^1$ and Br: $4s^2$, $4p^5$ valence electron configurations. In structural searches, the plane wave basis set was constructed with an energy cut-off of 400 eV and reciprocal space integrations were performed using Monkhorst-Pack method with $2\pi \times 0.05$ Å^{-1} grid spacing. Most important structures were re-optimized using an energy cut-off of 500 eV and reciprocal space sampling with $2\pi \times 0.02$ Å^{-1} grid spacing. Electronic properties were investigated by calculating valence charge density, Bader charge [18], electron-localization function (ELF) [19], electronic density of state function and crystal orbit Hamiltonian populations (COHP) [20-22]. Phonon calculations were performed using the QUANTUM-ESPRESSO code [23]. Phonon calculations used the “von Barth-Car” (VBC) norm conserving pseudopotential, as supplied by the code, with Perdew-Zunger exchange-correlation [24]. The charge density and ELF data were rendered using XCrySDen code [25].

4.2 Results and Discussion

Figure 4.1 shows the room temperature pressure evolution of Raman spectra of KBr + Br_2 sample. Raman modes of only bromine are visible up to 2.0 GPa. The bromine Raman modes (at 2.0 GPa) are located at 149.0(6), 287.1(2) and 300.1(1) cm^{-1}, in agreement with the previous measurements [26, 27]. Clearly, these observations rules out a chemical reaction between KBr and Br_2 up to this pressure. It may also be noted that Br_2 does not show a phase transition up to ~ 80 GPa [26]. Furthermore, KBr shows a B1 to B2 phase transition but the B2 phase is Raman inactive, similar to the B1 phase [5].

Above 3.0 GPa, the sample becomes visually black in colour (Fig. 4.2) and twelve new well resolved Raman modes appear in the Raman experiments (Fig. 4.3a). Appearance of these modes clearly indicate the formation of a new compound, but possibility of this compound being a high pressure phase of reactants was ruled out as the new Raman modes could not be assigned to them [5, 26, 27]. Thus it was inferred that a new compound is formed as a result of a chemical reaction between KBr and Br_2. Naturally, this compound will lie at the bromine rich side of the K-Br composition line. Frequencies of the new Raman modes at 3.2 GPa are 53.4(2), 56.9(1), 68.2(1), 76.5(2), 102.1(4), 112.8(3), 123.5(3), 127.0(6), 150.8(2), 156.1(1), 233.7(1) and 212.8(1) cm^{-1}. These modes showed normal behaviour with pressure, *i.e.*, frequency increase with pressure (Fig. 4.3b). Formation of a new crystalline compound (say, $K_{x1}Br_{y1}$) was reconfirmed by the x-ray diffraction experiments which showed new Bragg peaks, apart from KBr (B2 phase) and solid bromine peaks, in the diffraction pattern (Fig. 4.3c). This compound was stable in the pressure range of 3–6 GPa, at room temperature. This compound remained stable up to pressures of less than 1 GPa during the pressure release experiments.

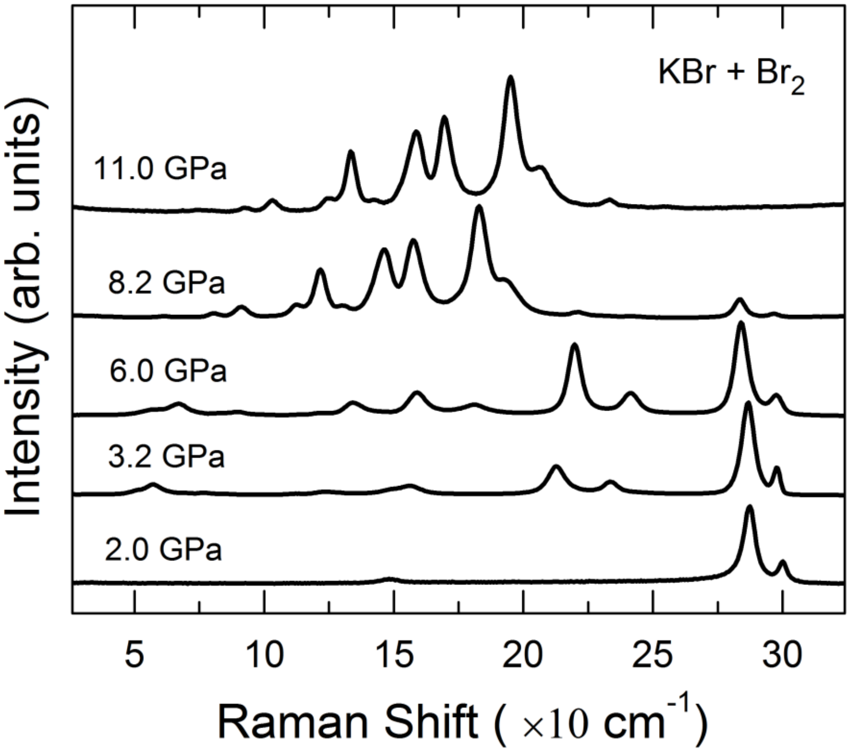

Fig. 4.1: *Pressure evolution of in-situ Raman spectra of KBr + Br_2*

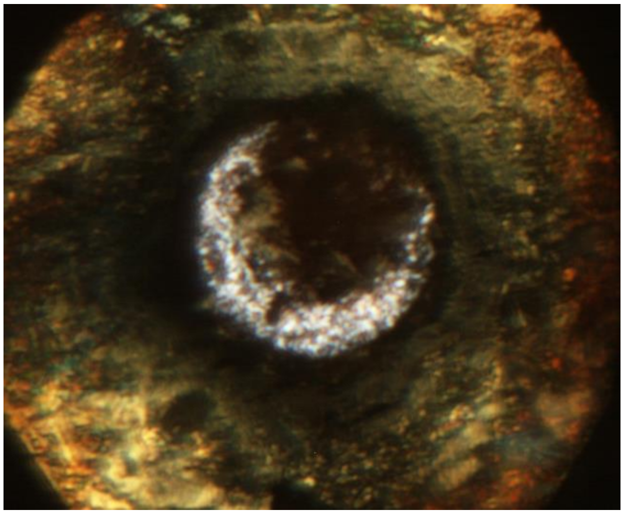

Fig. 4.2: *Image of sample chamber showing visual change in sample colour at 3.2 GPa.*

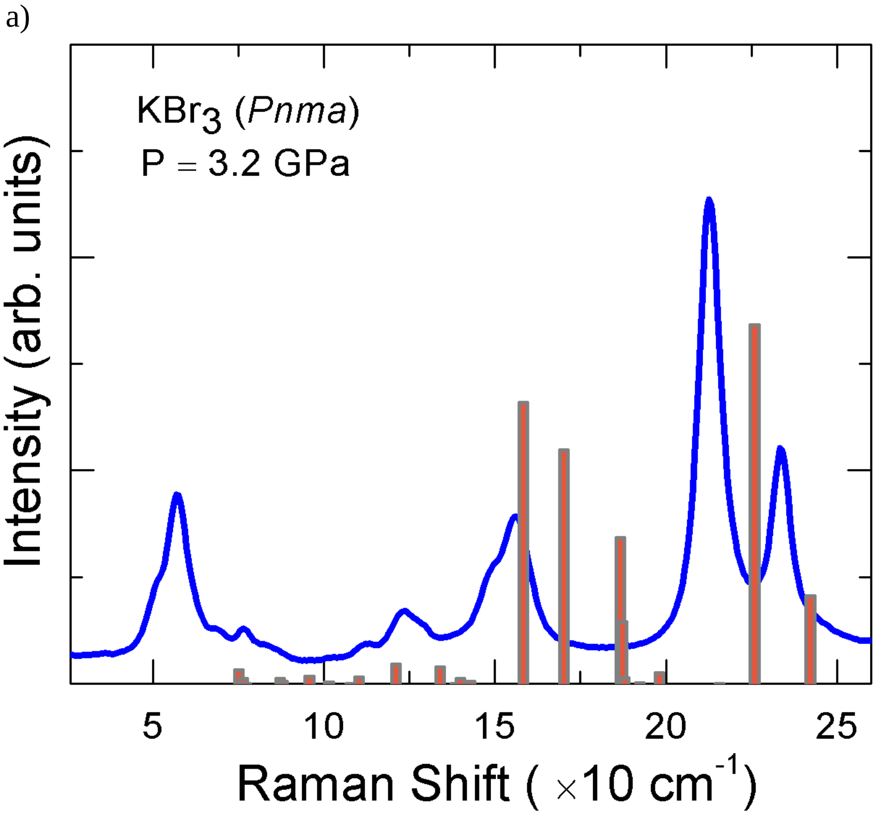
a)
KBr3 (Pnma)
P = 3.2 GPa
Intensity (arb. units)
5
10
15
20
25
Raman Shift (×10 cm-1)

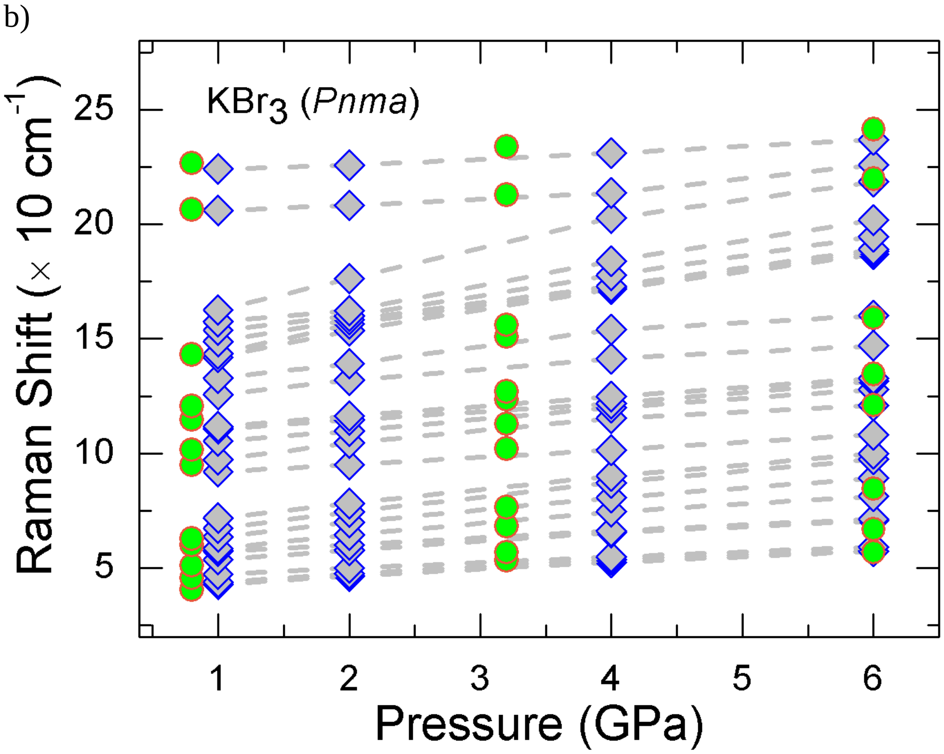
b)
KBr3 (Pnma)
Raman Shift (× 10 cm-1)
5
10
15
20
25
1
2
3
4
5
6
Pressure (GPa)

c)

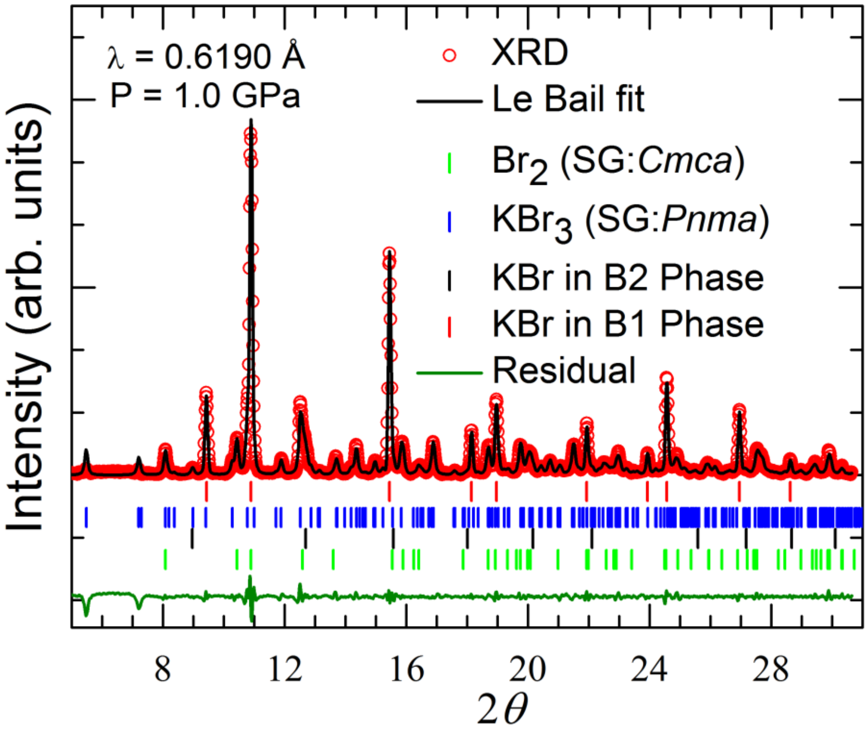

Fig. 4.3: *Structural and vibrational properties of the newly synthesized compound KBr_3 (SG: Pnma). (a) Experimental and theoretical Raman spectra, (b) pressure variation of Raman mode frequencies. Filled circles show experimental points and filled diamond show theoretical points, (c) Le-Bail fit of the pressure release run of ADXRD data.*

Above 6.0 GPa, nine additional well resolved Raman modes appeared (Fig. 4.4a). Intensities of these modes grew with time. However intensities of the earlier observed twelve new modes and bromine modes decreased with time. This observation indicates a simultaneous consumption of both $K_{x1}Br_{y1}$ and Br_2 and the synthesis of another compound (say, $K_{x2}Br_{y2}$) progressively. The frequencies of these modes at 8.2 GPa are 84.4(2), 95.5(1), 116.1(2), 125.1(1), 134.2(2), 149.9(1), 162.0(1), 186.2(1) and 199.2(1) cm^{-1}. Pressure variation of these modes is shown in

Fig. 4.4b. The x-ray diffraction experiments reconfirmed the formation of a new crystalline compound (Fig. 4.4c).

a)

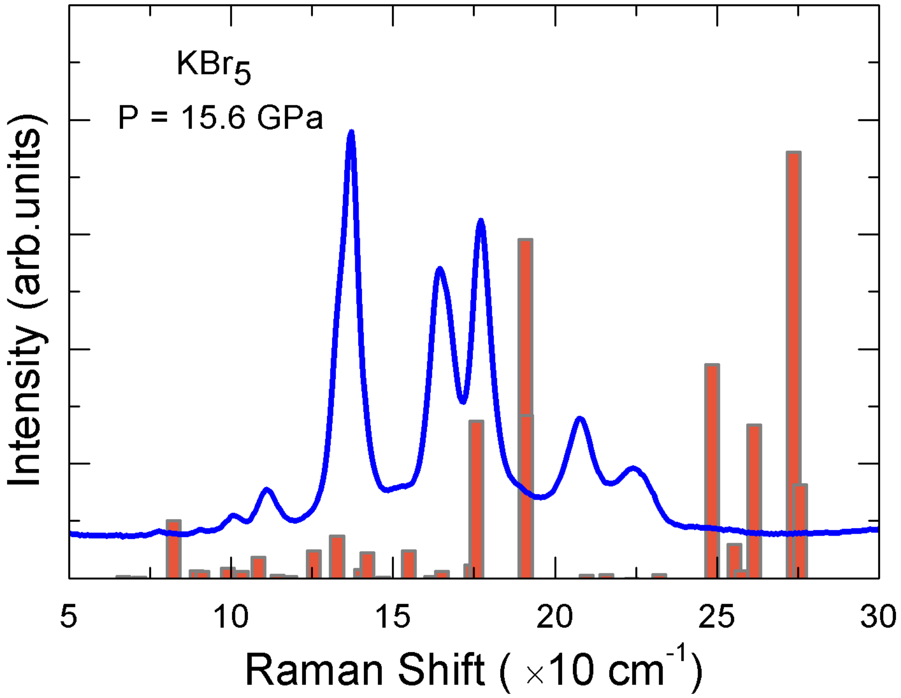

b)

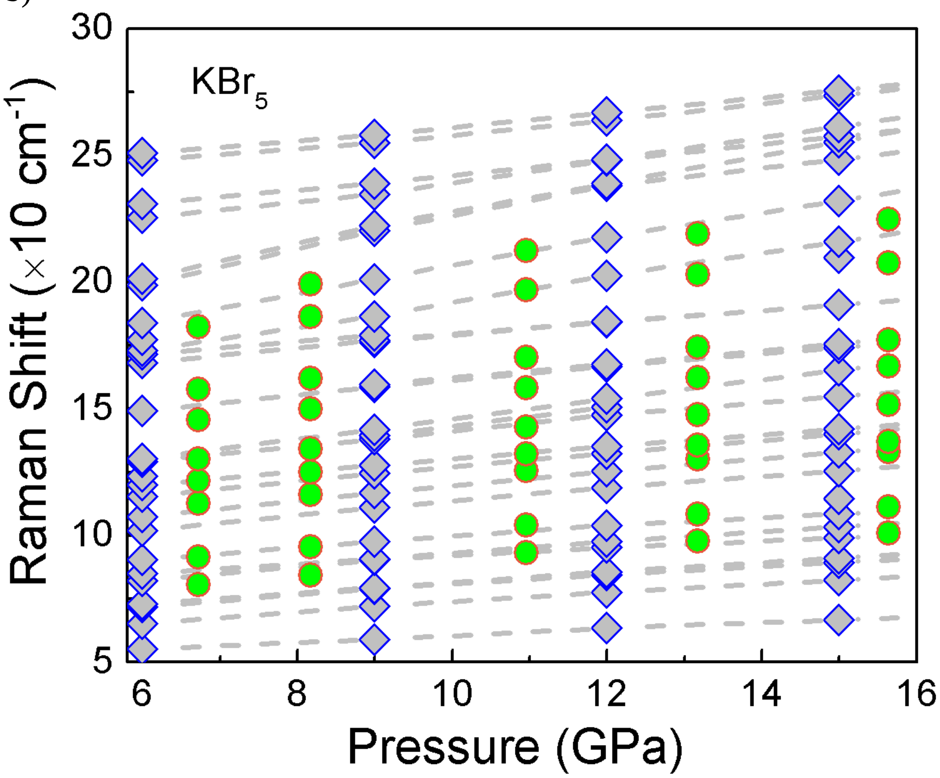

c)

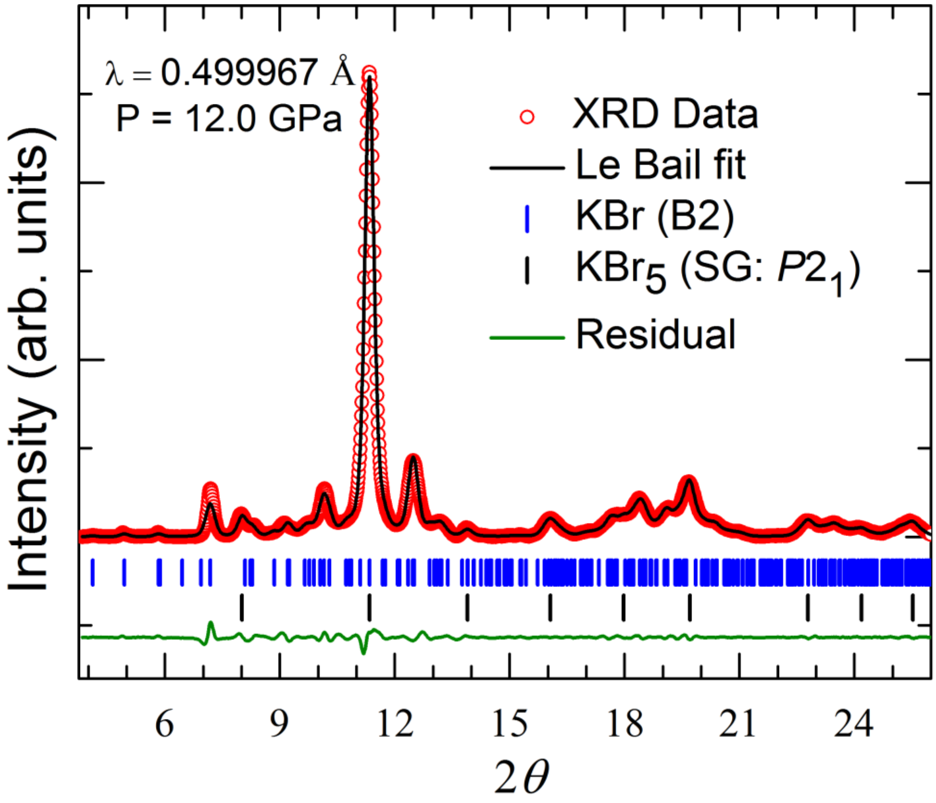

Fig. 4.4: *Structural and vibrational properties of the newly synthesized compound KBr_5 (SG: $P2_1$). (a) Experimental and theoretical Raman spectrum, (b) Pressure variation of Raman mode frequencies. Filled circles show experimental points and filled diamond show theoretical points, (c) Le-Bail fit of ADXRD data at 12 GPa.*

Unlike the first reaction, the second reaction progressed at a much slower rate and it took several hours to complete. The time evolution of the various modes, under constant applied load, is shown in Fig. 4.5a. This compound is also expected to lie in the bromine rich side of the K-Br composition line. During the commencement of the second reaction, the sample chamber pressure increased continuously with time. Time evolution of the sample chamber pressure was monitored in several runs and the pressure was always found to increase by about 2–3 GPa (Fig.

4.5b). In these measurements, the sample pressure was measured from the same ruby ball throughout the run at constant applied external load. To the best of our knowledge, this type of direct observation of pressure increase has not been reported so far. In view of the fact that DAC experiments are carried out at isothermal conditions, this observation implies the direct release of internal energy change into mechanical work. This compound remained stable up to the highest pressure of 24 GPa achieved in the present room temperature study. It may be noted that the present experiments were carried out under non-hydrostatic conditions. However due to the soft nature of both KBr and bromine, the deviatoric stresses are expected to be small in the pressure range covered by the experiments and therefore not a determining factor for the chemical reactions observed [28].

a)

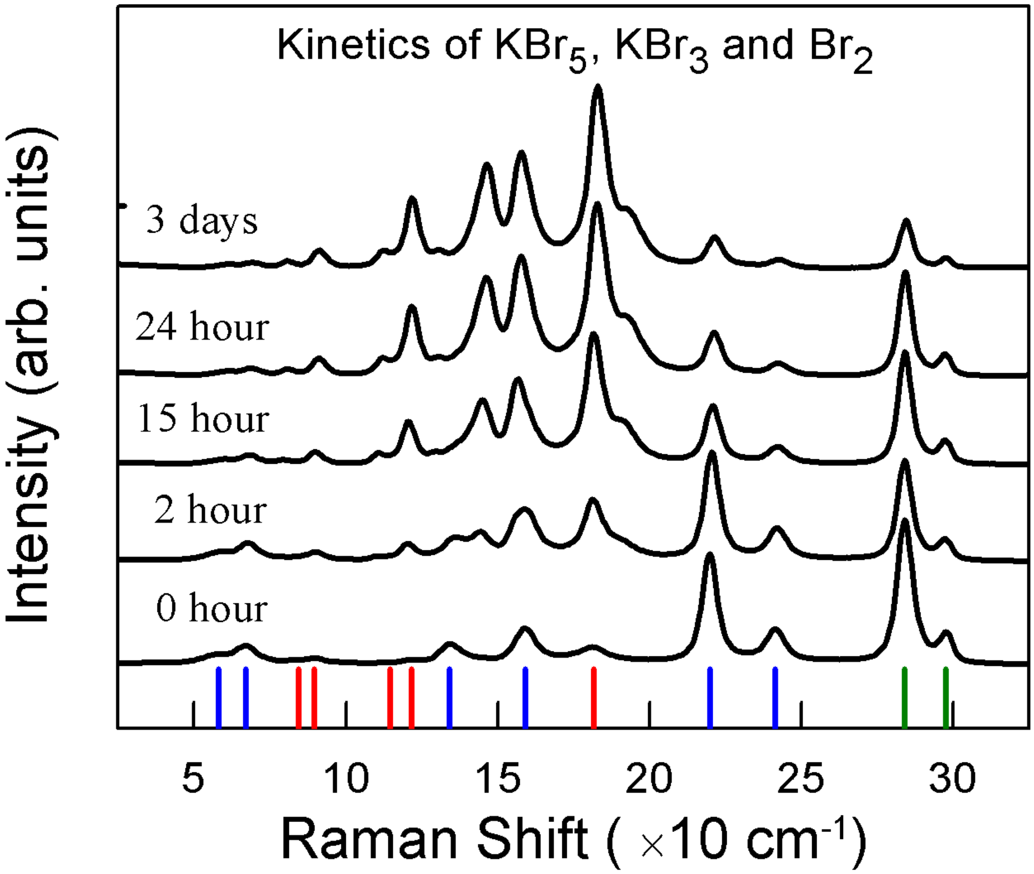

b)

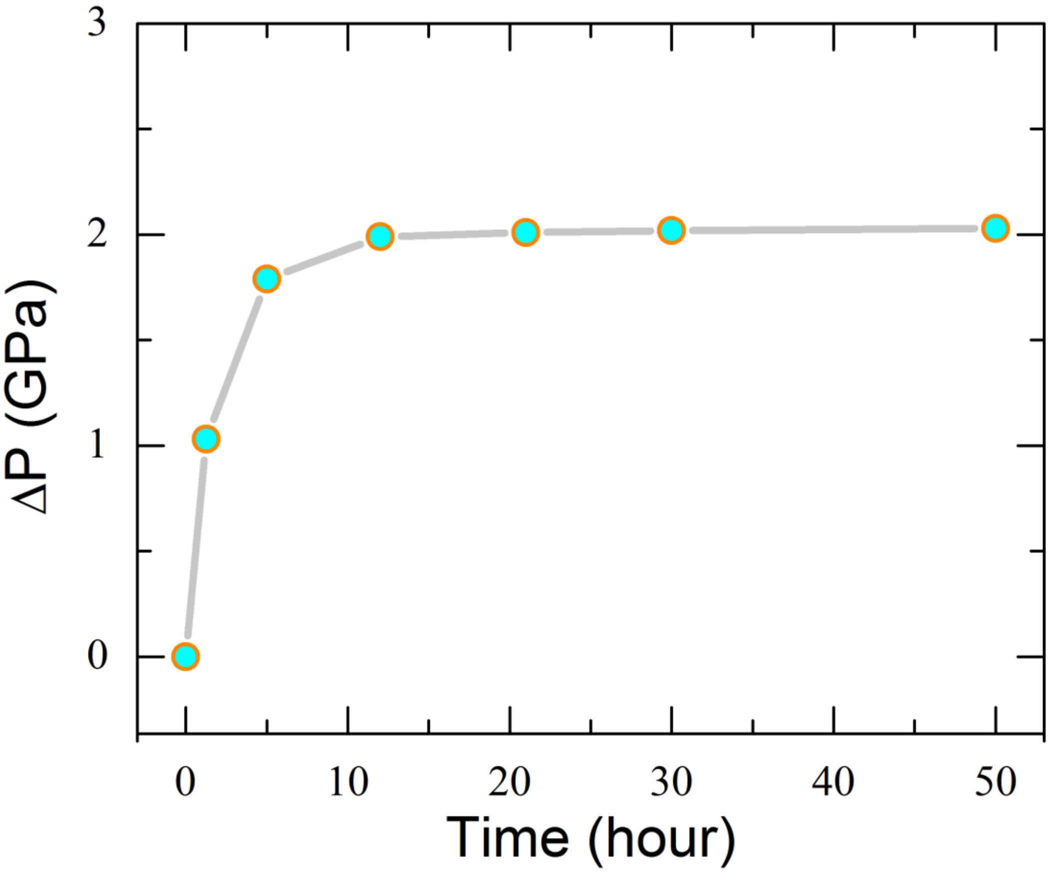

Fig. 4.5: *(a) Time evolution of in-situ Raman spectra of KBr_5, KBr_3 and Br_2 from a fixed sample position. Peaks marked with blue, red and green are guide to eye for high intensity Raman modes corresponding to KBr_3, KBr_5 and Br_2, respectively at time t = 0 and (b) increase of sample chamber pressure with time due to formation of the second stage compound, KBr_5.*

For compound $K_{x1}Br_{y1}$, the orthorhombic structure (SG: *Pnma*) of KBr_3 stoichiometry gave good agreement to the experimental x-ray diffraction pattern as shown in Fig. 4.3c. Calculated Raman frequencies and their pressure variation show reasonably good agreement with the experimental results (Figs. 4.2a and 4.2b). Calculated formation enthalpies also support the existence of this compound at the experimental pressures (Fig. 4.6a). Interestingly, the proposed structure is same as the ambient structure of CsI_3 [29]. Recently, similar structure was also reported in $NaCl_3$ [1]. But unlike our work, the formation of $NaCl_3$ was observed at much higher pressures and higher temperatures. Calculated pressure-volume (PV) EOS and lattice parameters are in reasonably good agreement with the experimental results (Fig. 4.6b and 4.6c). Phonon dispersion calculations yield all frequencies positive indicating vibrational stability of the compound (Fig. 4.6d).

a)

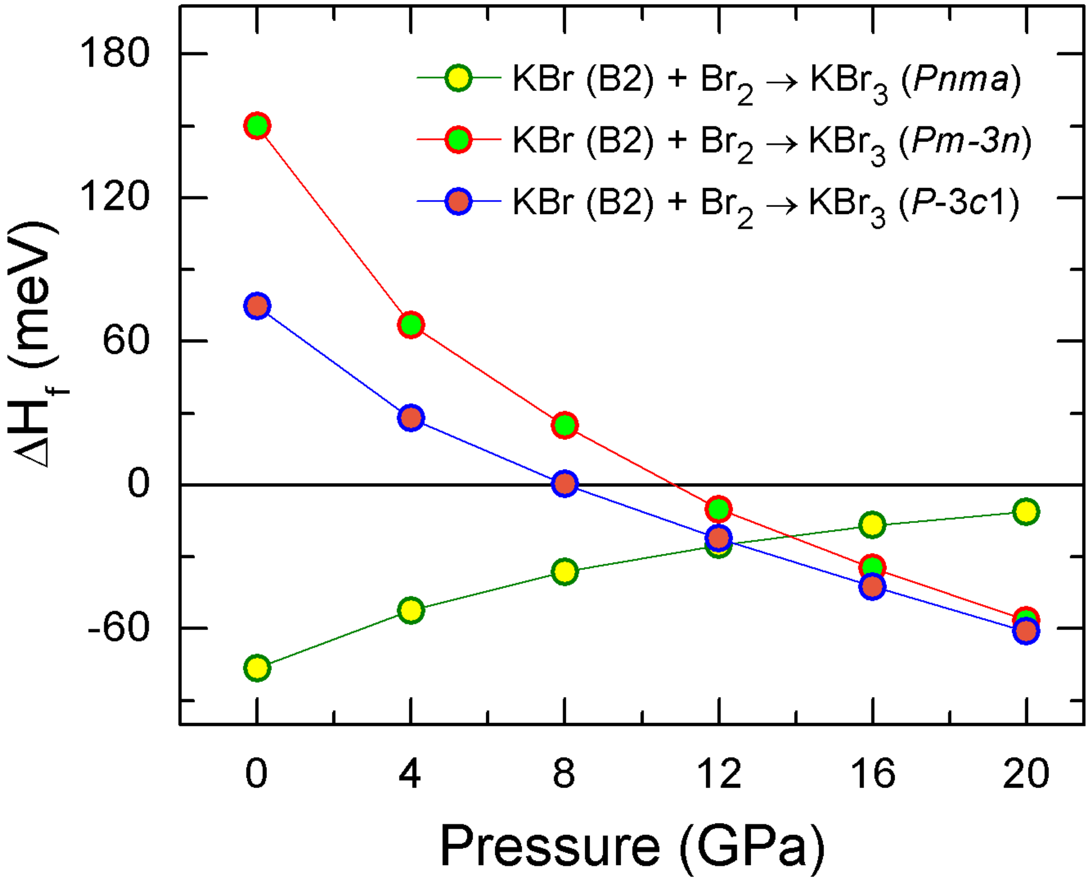

b)

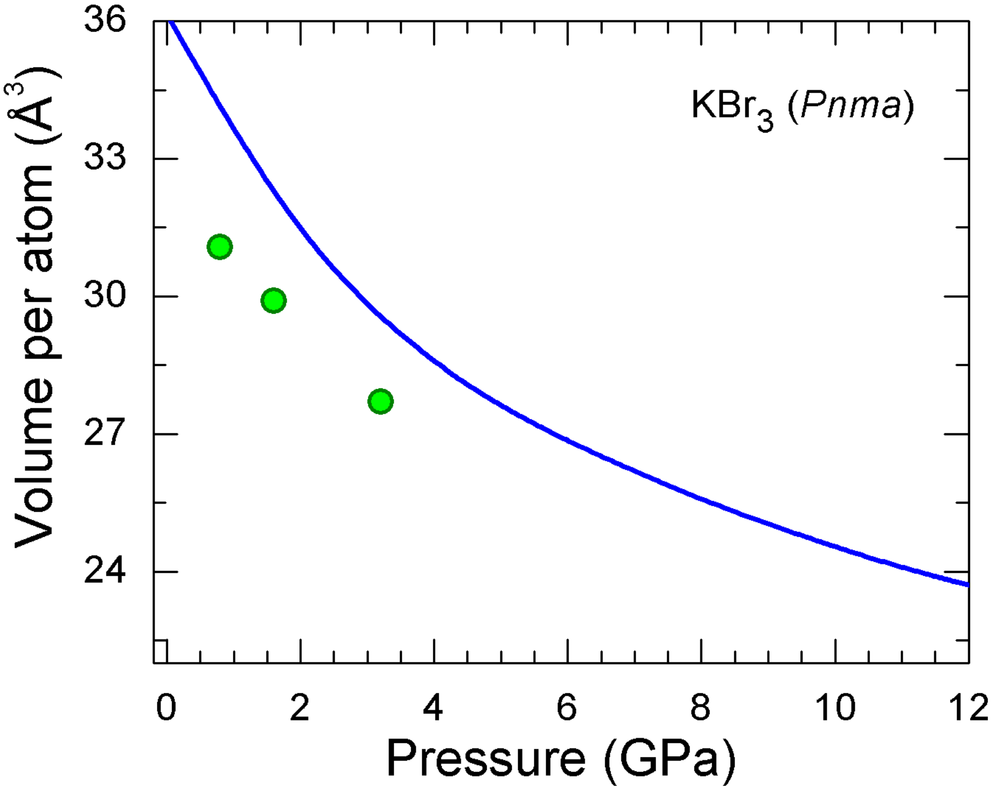

Volume per atom (Å^3)
36
33
30
27
24
KBr$_3$ (*Pnma*)
0
2
4
6
8
10
12
Pressure (GPa)

c)

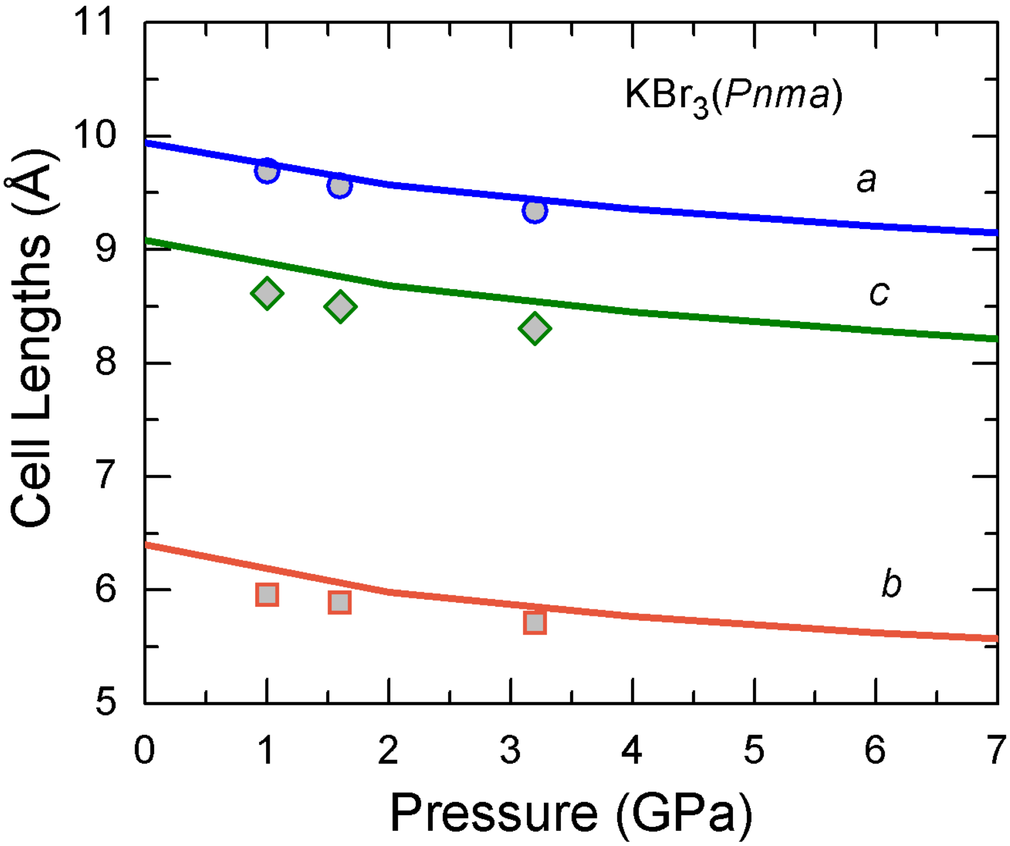

Cell Lengths (Å)
11
10
9
8
7
6
5
KBr$_3$(*Pnma*)
a
c
b
0
1
2
3
4
5
6
7
Pressure (GPa)

d)

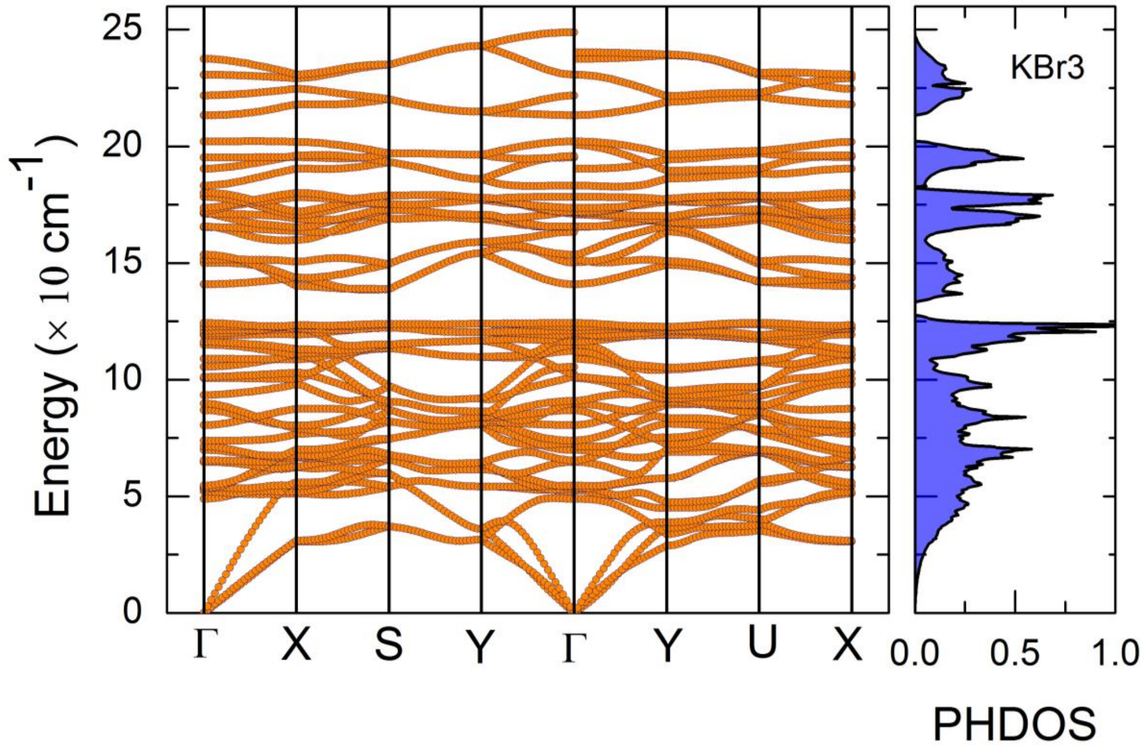

Fig. 4.6: *(a) Formation enthalpies in different reactions for* KBr_3*, Enthalpies are given per atom. (b) Experimental (filled symbols) and theoretical (lines) equations-of-state, along with (c) pressure variation of theoretical (lines) and experimental (symbols) lattice parameters of orthorhombic* KBr_3*. (d) Phonon dispersion curves and phonon density of states (PHDOS) for orthorhombic* KBr_3 *at 4 GPa.*

For $K_{x2}Br_{y2}$ compound, the monoclinic structure (SG: *P2₁*) with KBr_5 stoichiometry as shown in Fig. 4.4c showed good agreement to the experimental x-ray diffraction pattern. Calculated Raman frequencies and their pressure variation have a reasonably good match with the experimental results (Figs. 4.3a and 4.3b). The experimental Raman frequencies and their pressure coefficients for KBr_3 and KBr_5 are shown in Table 4.1 and Table 4.2 respectively.

Table 4.1: Raman mode frequencies (ω_0) of KBr_3 (SG: *Pnma*) and their pressure coefficient obtained by a linear fit.

Raman mode frequency ω_0 (cm^{-1}) (at P=3.2 GPa)	($d\omega/dp$) (cm^{-1}/GPa)
53.4	2.15
56.9	3.07
68.2	3.38
76.5	4.14
102.1	3.00
112.8	4.70
123.5	1.23
127.0	2.71
150.8	3.08
233.7	2.57
212.8	2.84

Table 4.2: Raman mode frequencies (ω_0) of KBr_5 (SG: $P2_1$) and their pressure coefficients obtained by a quadratic fit.

Raman mode frequency ω_0 (cm^{-1}) (at P=8.2 GPa)	($d\omega/dp$) (cm^{-1}/GPa)	($d^2\omega/dp^2$) (cm^{-1}/GPa^2)
84.4	6.25	-0.17
95.5	6.62	-0.19
116.1	6.03	-0.16
125.1	6.03	-0.19
134.2	6.17	-0.17
149.9	7.54	-0.24
162.0	6.02	-0.17
186.2	3.27	0.0
199.2	4.36	0.0

Calculated formation enthalpies also support the formation of this compound at the experimental pressures (Fig 4.6a). This is the first experimental report of synthesis of an alkali-halide in 1:5 stoichiometry. Calculated PV-EOS and lattice parameters are in reasonably good agreement with the experimental data (Fig. 4.7b and 4.7c). Calculated phononic properties establish the vibrational stability of the proposed structure (Fig. 4.7d). Atomic volume for KBr_5 has the largest value among all others, namely KBr, Br_2 and KBr_3, explaining the observed pressure increase during the formation of this compound (Fig. 4.8). Indeed, KBr_5 has about 3.39 % higher atomic volume than KBr at 12 GPa.

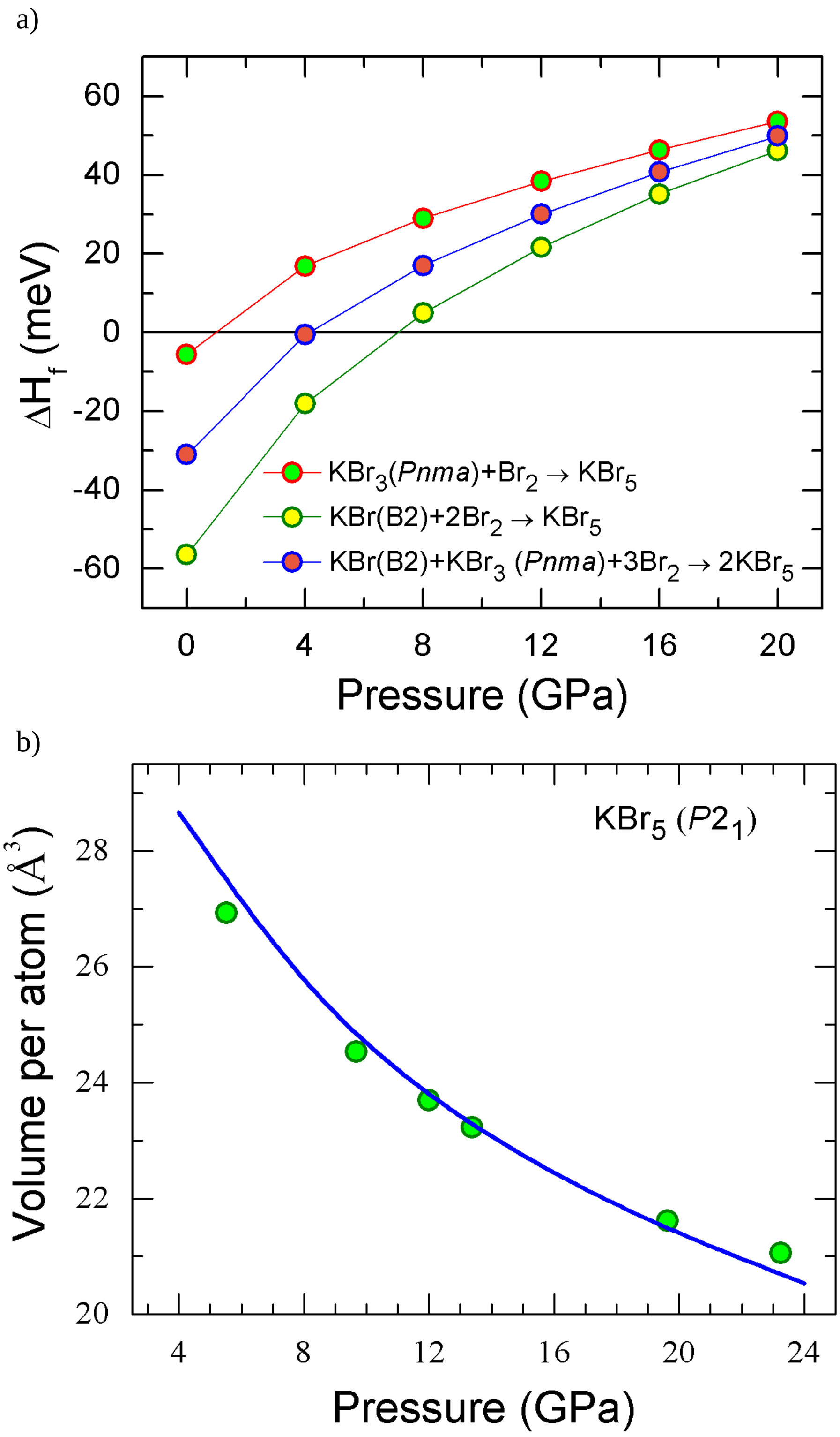

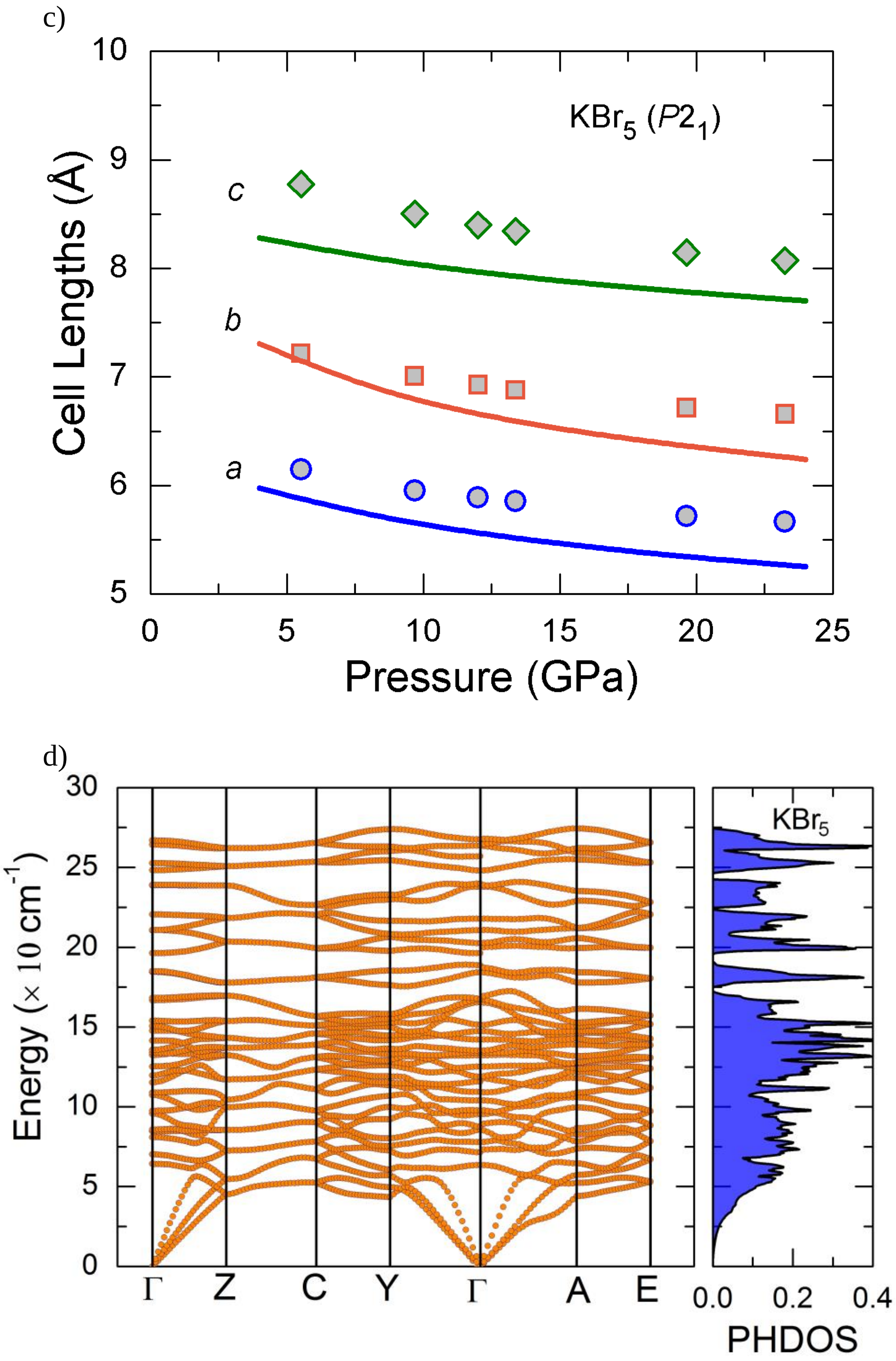

Fig. 4.7: *(a) Formation enthalpies in different reactions for KBr*$_5$*. Enthalpies are given per atom. The experimental observations of simultaneous consumption of Br*$_2$ *and KBr*$_3$ *ruled out second reaction for KBr*$_5$ *formation. (b) Experimental*

(filled symbols) and theoretical (lines) equations-of-state, along with (c) pressure variation of theoretical (lines) and experimental (symbols) lattice parameters of monoclinic KBr_5. (d) Phonon dispersion curves and phonon density of states (PHDOS) for KBr_5 at 12 GPa.

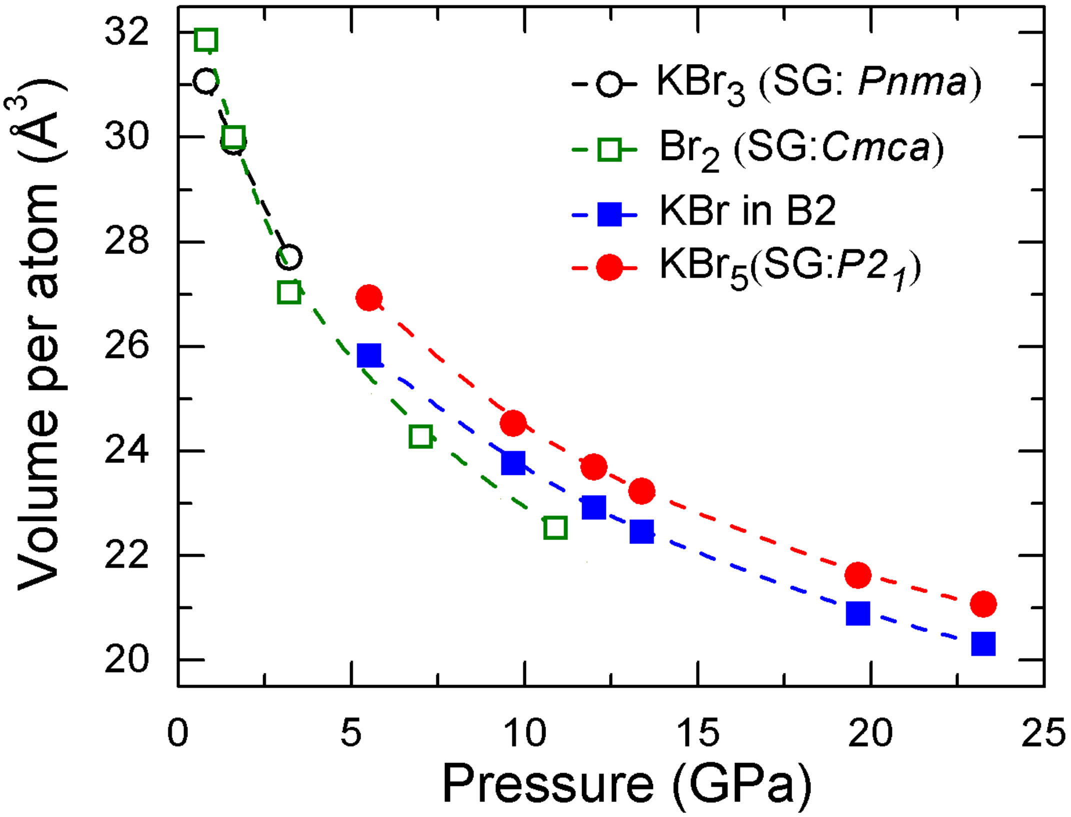

Fig. 4.8: *Experimental equations of state of KBr (B2 phase, SG: Pm-3m), Br_2 (SG: Cmca), KBr_3 (SG: Pnma) and KBr_5 (SG: $P2_1$). Dotted lines are guide to the eye. Error bars in pressure are within the symbol.*

The orthorhombic KBr_3 has an almost linear asymmetric Br_3 units (Table 4.3). The Bader charge analysis shows that the compound has a predominant ionic bonding between potassium and Br_3 unit, but bromine atoms are not bonded through ionic interactions (Table 4.4). The K—Br bond-lengths in the three different stoichiometric compounds are tabulated in Table 4.5. The total DOS function shows insulating nature of this compound.

Table 4.3: Intra-molecular bond-angles and bond-lengths of bromine atoms in different systems.

Material	Space group	Bond-angles (deg.)		Bond-lengths (Å)	
Br_2	liquid	-------		Br–Br	2.28
KBr_3	*P*-3*c*1 (15 GPa)	∠Br1–Br2–Br2	179.47	Br1–Br2 Br2–Br2	2.90 2.51
	Pnma (4 GPa)	∠Br1–Br2–Br3	178.39	Br1–Br2 Br2–Br3	2.64 2.49
KBr_5	$P2_1$ (16 GPa)	∠Br2–Br5–Br4 ∠Br5–Br4–Br1 ∠Br4–Br1–Br3	176.79 115.98 164.15	Br4–Br5 Br2–Br5 Br1–Br3 Br4–Br1	2.55 2.52 2.40 2.64

Table 4.4: Details of most probable compositions and their structures in the K– Br system along with corresponding Bader charges (|e|) and electronic band gaps (E_g) in electron-volts (eV).

Compound	Lattice parameters (Å & °)				Atomic coordinates	Bader Charge, |e|
	Theory	P (GPa)	Experimental	P (GPa)		
KBr (B2 phase)	*a* = 3.8339	4.0			K 1*a* 0.0000; 0.0000; 0.0000 Br 1*b* 0.5000; 0.5000; 0.5000	K: +0.80 Br:: –0.80
KBr$_3$ (*Pnma*)	*a* = 9.3592 *b* = 5.7661 *c* = 8.4534	4.0	*a* = 9.339(3) *b* = 5.712(1) *c* = 8.309(1)	3.2	K1 4*c* 0.1687; 0.2500; 0.5281 Br1 4*c* 0.3428; 0.2500; 0.8463 Br2 4*c* 0.1243; 0.2500; 0.0445 Br3 4*c* 0.4233; 0.2500; 0.2625	K : +0.82 Br1 : –0.47 Br2 : –0.04 Br3 : –0.31 Eg: 2.01
KBr$_3$ (*Pm*-3*n*)	*a* = 5.5332	16.0			K 2*a* 0.0000; 0.0000; 0.0000 Br 6*c* 0.2500; 0.0000; 0.5000	K : +0.74 Br : –0.24 Eg: 3.50
KBr$_3$ (*P*-3*C*1)	*a* = 7.8357 *b* = 9.6237 γ = 120 °	16.0	*a* = 7.838(1) *b* = 9.841(2) γ = 120 °	15.4	K1 2*b* 0.0000; 0.0000; 0.0000 K2 4*d* 0.3333; 0.6666; 0.3223 Br1 6*f* 0.2463; 0.0000; 0.2500 Br2 12*g* 0.3488; 0.4223; 0.0753	K1 : +0.76 K2 : +0.75 Br1 : –0.41 Br2 : –0.17 Eg: 0.19

KBr_5 ($P2_1$)	*a* = 5.5564	12.0	*a* = 5.884(1)	12.0	K	2*a*	0.6977; 0.5012; 0.3788	K : +0.78
	b = 6.6484		*b* = 6.927(1)		Br1	2*a*	0.1552; 0.1931; -0.065	Br1 : –0.02
	c = 7.9628		*c* = 8.401(1)		Br2	2*a*	0.1829; 0.3104; 0.3178	Br2 : –0.31
	β = 104.66 °		β = 123.92 ° (1)		Br3	2*a*	0.7613; 0.3085; 0.7586	Br3 : –0.20
					Br4	2*a*	0.6322; 0.1585; 0.0969	Br4 : –0.17
					Br5	2*a*	0.2721; 0.4928; 0.6044	Br5 : –0.07
								Eg: 1.46
Br_2 (*Cmca*)	*a* = 6.0946	8.0			Br	8*f*	0.0000; 0.8303; 0.3787	
	b = 3.8610							
	c = 8.3080							

Table 4.5: K—Br bond-lengths in different compounds.

Material	Space group	Pressure (GPa)	Bond-lengths (Å)	
KBr_3	*P*-3*c*1	15.0	K–Br1 K–Br2 K–Br2	3.08 3.09 3.14
KBr_3	*Pnma*	4.0	K–Br1 K–Br2 K–Br3	3.14 3.47 3.27
KBr_5	$P2_1$	16.0	K–Br1 K–Br2 K–Br3 K–Br4 K–Br5	3.09 3.05 3.22 3.15 3.24

The monoclinic KBr_5 compound has V-shaped pentabromide (Br_5) units. All Br–Br distances in the pentabromide unit are significantly larger than the distances in the liquid bromine (Table 4.3). The Bader charge analysis shows a charge transfer from potassium atom to the pentabromide unit. Therefore potassium (K^+) and pentabromide unit (Br_5^-) mainly interact through ionic interactions whereas the bromine atoms in pentabromide unit are bonded by covalent interaction. The insulating nature of this compound is evident from the total DOS function.

To get further insight into the chemical reaction pathways, laser heating experiments were carried out using our laboratory based laser heated diamond anvil cell (LHDAC) facility in the pressure range of 14–20 GPa and temperature of ~ 1500 K with typical temperature uncertainty of 100 K. Post laser heated samples were investigated by Raman spectroscopy and x-ray diffraction measurements. Detailed Raman measurements and structural refinements of the various laser heated spots, showed an irreversible decomposition of KBr_5 to a new compound, say $K_{x3}Br_{y3}$ as shown in Fig. 4.9a and 4.9b, rather than to the orthorhombic KBr_3 phase (Fig. 4.3a) as the Raman spectra was distinctly different. Interestingly, a large pressure drop (~ 3GPa in the 18 GPa run) was observed in all the laser heating experiments. This reconfirms the formation of a low density monoclinic KBr_5 compound at room temperature (Fig. 4.8). For compound $K_{x3}Br_{y3}$, the trigonal KBr_3 structure gives an extremely good fit to the x-ray diffraction pattern as shown in Fig. 4.9b. Similar structure has been recently reported in KCl_3 between 20–40 GPa [2].

a)

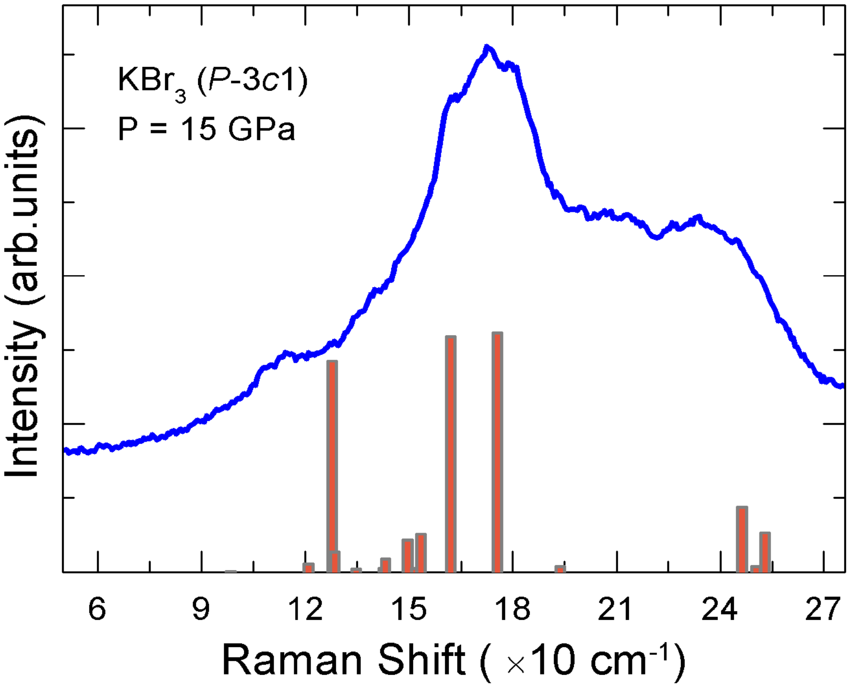

b)

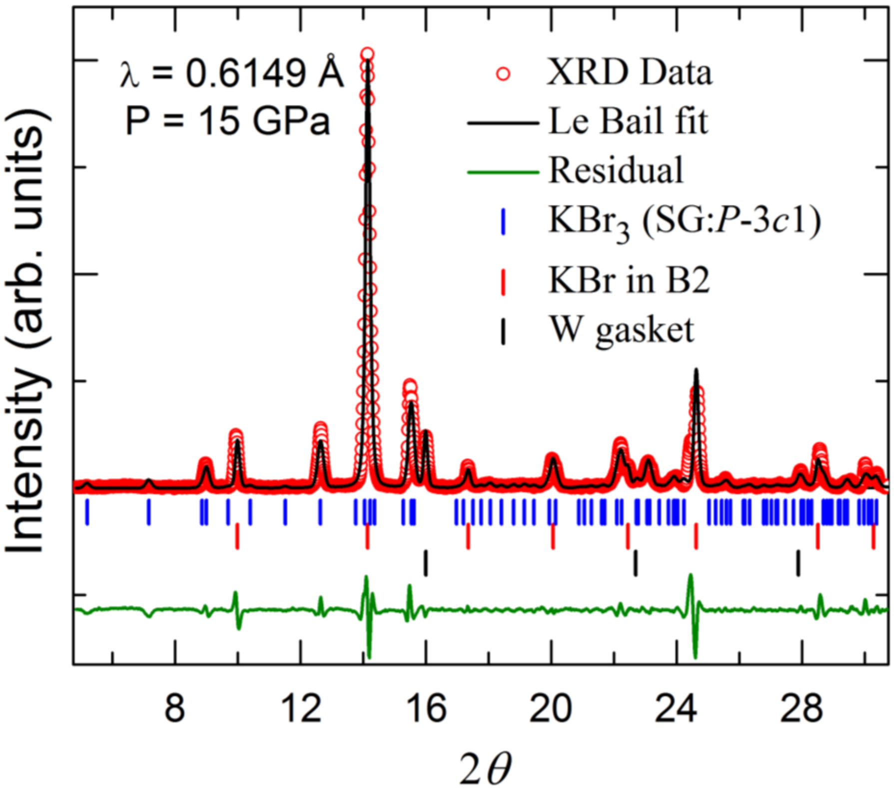

***Fig. 4.9:** Structural and vibrational properties of the newly synthesized trigonal KBr_3 (SG: P-3C1) compound. (a) Experimental and theoretical Raman spectrum, (b) Le Bail fit to ADXRD data at 15 GPa.*

Calculated PV-EOS and lattice parameters are in good agreement with the experimental results (Figs. 4.10a, 4.10b and Table 4.6). Even though the calculated Raman spectrum shows fairly good match with the experimental results, this phase has two small imaginary frequencies at zone centre indicating the dynamical instability of the structure. However, a good agreement between experimental and theoretical results prompted us to speculate that the trigonal phase could be an entropically stabilized phase, as the experiments were performed at finite temperatures whereas calculations were done at zero Kelvin temperature.

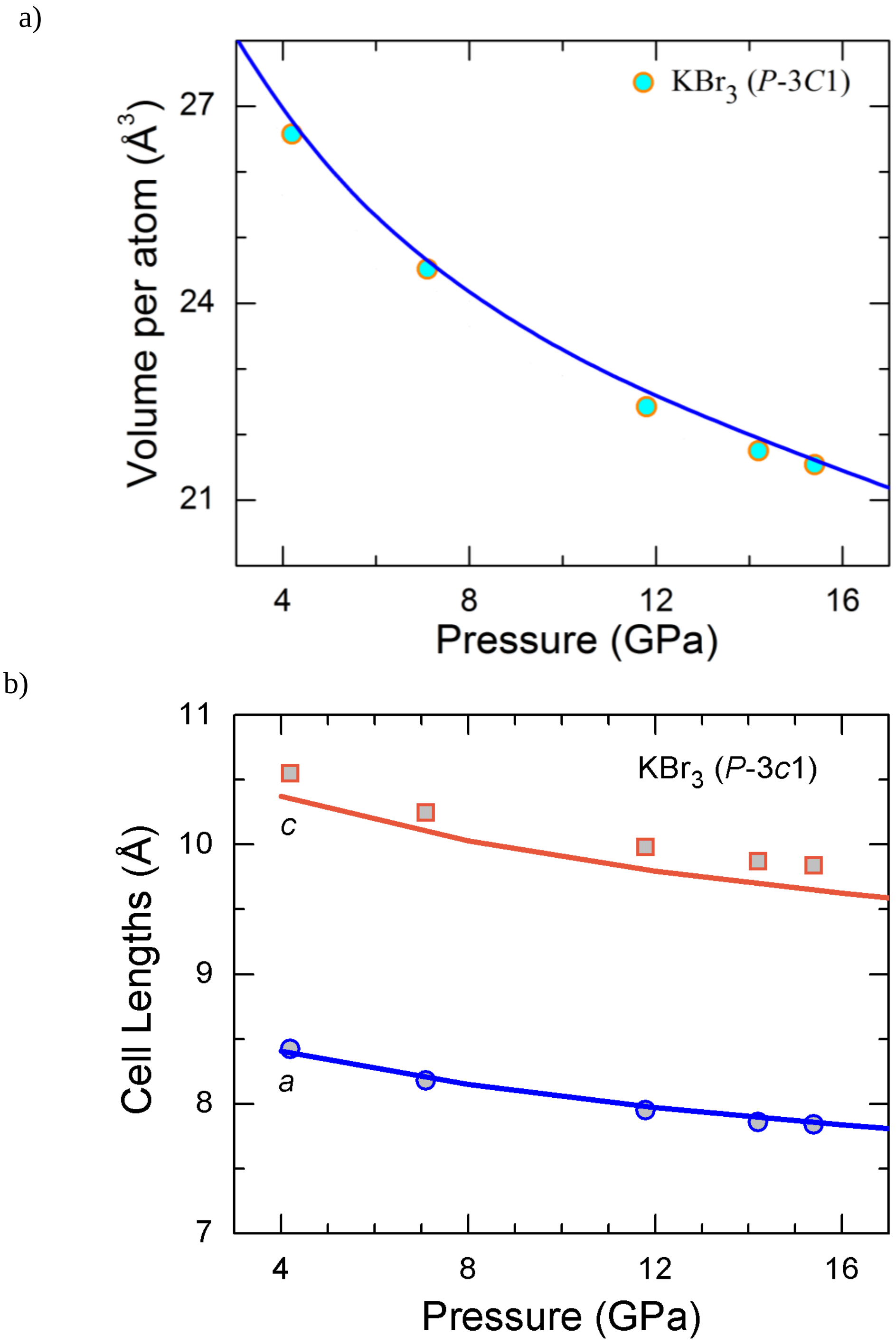

Fig. 4.10: *(a) Experimental (filled symbols) and theoretical (lines) equations of state of trigonal KBr$_3$ (SG: P-3C1), (b) pressure variation of theoretical (lines) and experimental (symbols) lattice parameters of trigonal KBr$_3$ (SG: P-3C1).*

Table 4.6: Experimental and theoretical unit cell volume (V_0), bulk modulus (B_0) and derivative of bulk modulus ($B_0^{'}$) obtained by fitting the Birch-Murnaghan equation of state to the PV data of KBr_3 and KBr_5.

Material	Space Group	V_0 in Å^3	B_0 in GPa	$B_0^{'}$	V_0 in Å^3	B_0 in GPa	$B_0^{'}$
		Experiment			Theory		
KBr_3	*Pnma*	534.37	11.8	4.0	574.09	11.1	4.0
	P-3*c*1	770.73	15.5	4.55	764.47	14.4	4.33
KBr_5	*P*2$_1$	417.68	11.2	4.58	418.35	13.8	3.65

The trigonal KBr_3 has loosely formed Br_3 units. Table 4.3 gives the Bader charges on potassium and bromine atoms. Fig. 4.11a and 4.11b depicts the crystal structures of KBr_3 (both in the orthorhombic and trigonal phase) and KBr_5 along with the enthalpy curve illustrating the structural stability of various phases of KBr_3.

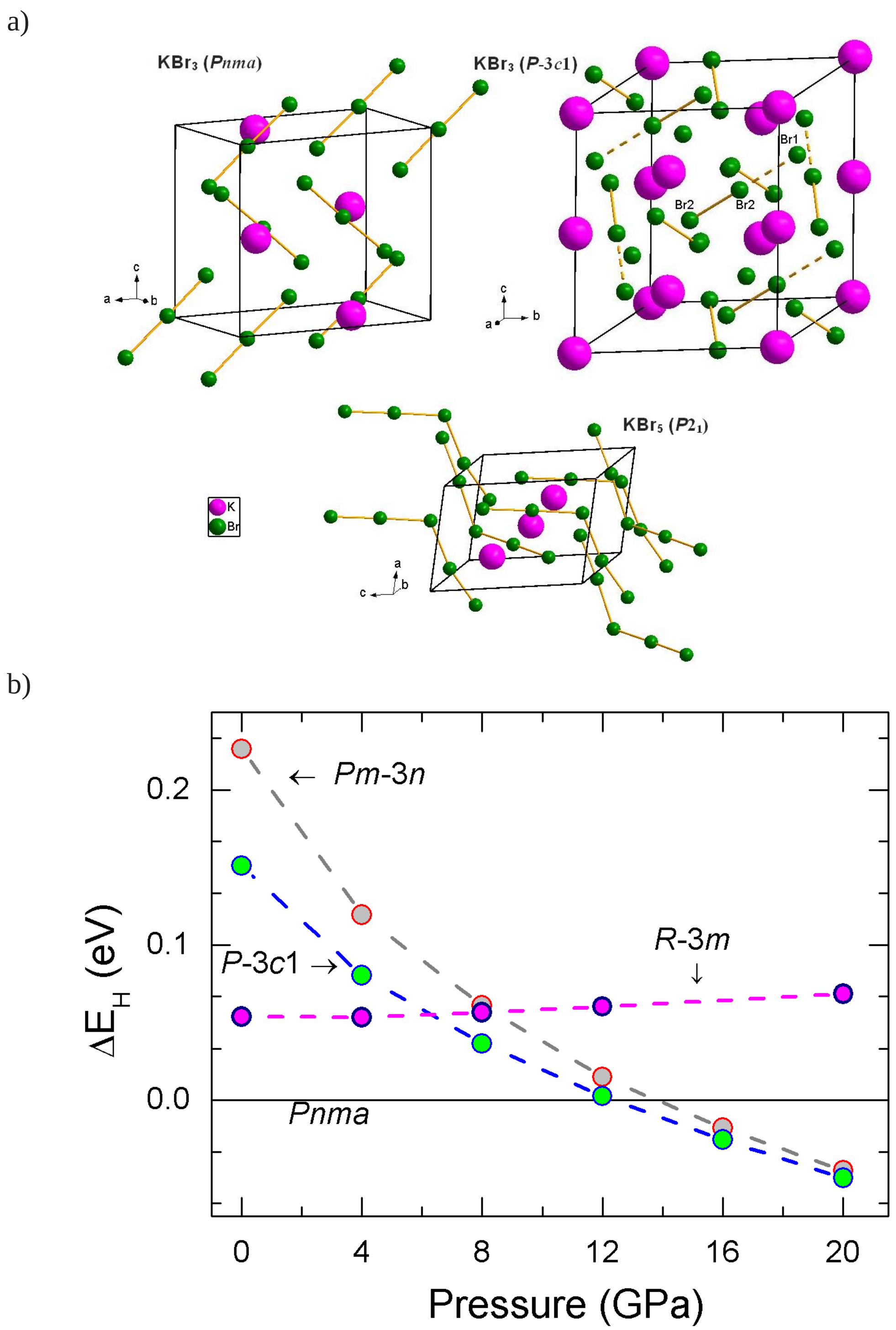

Fig. 4.11: *(a) Crystal structures of KBr_3 (SG: Pnma) and KBr_5 (SG: $P2_1$) and KBr_3 (SG: P-3C1). (b) Enthalpy curve illustrating the structural stability of various phases of KBr_3. Here R-3m structural data was taken from Ref. [2].*

The important aspect of this work is that both KBr_3 and KBr_5 form at low pressures and room temperature in contrast to the compounds formed in the Na-Cl and K-Cl systems where much higher pressure and higher temperature are needed. KBr and Br_2 react only after B1 to B2 phase transition. Thus it appears that the B2 phase plays a significant role in this reaction. This implies that the experimental retrieval of AX_3 (A = alkali metals, X = halogens) stoichiometric compounds at ambient pressure would be possible only for those alkali halides which exist either in the B2 phase at ambient pressure or whose B2 to B1 hysteresis limit extend to ambient pressure. This finding deposes the earlier belief of larger cation and anion radii requirement for the formation of alkali polyhalides [30]. The proposition is well supported by the fact that KI_3, $CsBr_3$, CsI_3 and RbI_3 exist at ambient conditions and also by the decomposition of $NaCl_3$, KCl_3 and KBr_3 below 20, 2.0 and 1.0 GPa respectively. This may provide an impetus to the current search for alkali polyhydrides since alkali hydrides also show B1 to B2 phase transition at high pressures [31, 32].

4.3 Conclusions

This work reports the synthesis of two new stoichiometric compounds, *viz.*, KBr_3 and KBr_5 at high pressures in the K-Br system. Formation of these compounds were detected and confirmed by Raman spectroscopy and x-ray diffraction measurements. Compositions and related crystal structures were solved by first-principles structural search method. The most unusual feature of monoclinic KBr_5 formation is an abnormal pressure increase in the sample chamber. Underlying chemical reaction in KBr_5 formation proceeds very slowly in comparison to the orthorhombic KBr_3 formation reaction. On heating, the monoclinic KBr_5 decomposes into a trigonal KBr_3 and Br_2.

References

[1] W. Zhang, A. R. Oganov, A. F. Goncharov, Q. Zhu, S. E.Boulfelfel, A. O. Lyakhov, E. Stavrou, M. Somayazulu, V. B. Prakapenka and Z. Konopkova, *Science*, **342**, 1502 (2013).

[2] W. Zhang, A. R. Oganov, Q. Zhu, S. S. Lobanov, E. Stavrou and A. F. Goncharov, *Sci. Rep.*, **6**, 26265 (2016).

[3] C. Pépin, P. Loubeyre, F. Occelli and P. Dumas, *Proc. Nat. Acad. Sci.*, **112**, 7672 (2015).

[4] P. Baettig and E. Zurek, *Phys. Rev. Latt.* **106**, 237002 (2011).

[5] A. Dewaele, A. B. Belonoshko, G. Garbarino, F. Occelli, P. Bouvier, M. Hanfland and M. Mezouar, *Phys. Rev. B*, **85**, 214105 (2012).

[6] K. K. Pandey, H. K. Poswal, A. K. Mishra, A. Dwivedi, R. Vasanthi, N. Garg and S. M. Sharma, *Pramana J. Physics* , **80**, 607 (2013).

[7] A. Lausi, M. Polentarutti, S. Onesti, J.R. Plaisier, E. Busetto, G. Bais, L. Barba, A. Cassetta, G. Campi, D. Lamba, A. Pifferi, S. C. Mande, D. D. Sarma, S. M. Sharma and G. Paolucci, *Eur. Phys. J. Plus*, **43**,130 (2015).

[8] A. P. Hammersley, S. O. Svensson, M. Hanfland, A. N. Fitch and D. Hausermann, *High Press. Res.*, **14**, 235 (1996).

[9] A. C. Larson and R. B. Von Dreele, *Los Alamos National Laboratory Report LUAR*, **86**, 748 (1994).

[10] N. N. Patel, S. Meenakshi and S.M. Sharma, *AIP Conf. Proc.*, **1591**, 664 (2014).

[11] A. R. Oganov and C. W. Glass, *J. Chem. Phys.*, **124**, 244704 (2006).

[12] A. R. Oganov, A. O. Lyakhov and M. Valle, *Acc. Chem. Res.*, **44**, 227 (2011).

[13] A. O. Lyakhov, A. R. Oganov, H. T. Stokes and Q. Zhu, *Comput. Phys. Commun.*, **184**, 1172 (2013).

[14] G. Kresse and J. Furthmuller, *J. Comput. Mater. Sci.* **6**, 15 (1996); P. E. Blöchl, *Phys. Rev. B*, **50**, 17953 (1994).

[15] G. Kresse, and D. Joubert, *Phys. Rev. B*, **59**, 1758 (1999).

[16] G. Kresse and H. Hafner, *J. Phys.: Condens. Matter* , **6**, 8245 (1994).

[17] J. P. Perdew, K. Burke and M. Ernzerhof, *Phys. Rev. Lett.*, **77**, 3865 (1996).

[18] R. F. W. Bader, (Oxford Uni. Press, Oxford, 1990).

[19] A. D. Becke and K. E. Edgecombe, *J. Phys. Chem.*, **92**, 5397 (1990).

[20] R. Dronskowski and P. E. Blochl, *J. Phys. Chem.*, **97**, 8617 (1990).

[21] V. L. Deringer, A. L. Tchougréeff, R. Dronskowski, *J. Phys. Chem. A*, ***115,*** 5461 (2011).

[22] S. Maintz, V. L. Deringer, A. L. Tchougréeff and R. Dronskowski, *J. Comput. Chem.*, ***34***, 2557 (2013).

[23] P. Giannozzi, *et al*, *J. Phys.: Condens. Matter*, **21**, 395502 (2009).

[24] J. P. Perdew and A. Zunger, *Phys. Rev. B*, **5048**, 23 (1981).

[25] A. Kokalj, *Comp. Mater. Sci.*, **28**, 155 (2003).

[26] T. Kume, T. Hiraoka, Y. Ohya, S. Sasaki and H. Shimizu, *Phys. Rev. Lett.* , **94**, 065506 (2005).

[27] A. J. Melveger, J. W. Brasch and E. R. Lippincott, *Mat. Res. Bull.*, **4**, 515 (1969).

[28] D. Errandoneaa, Y. Meng, M. Somayazulu and D. Hausermann, *Physica B*, **355**, 116 (2005).

[29] R. M. Bozorth and L. Pauling, *J. Am. Chem. Soc.*, **47**,1561 (1925).

[30] G. L. Clark, *Proc. Natl. Acad. Sci.*, **9**, 117 (1923).

[31] S. J. Duclos, Y.K. Vohra and A. L. Ruoff, *Phys. Rev. B*, **36**, 7664 (1987).

[32] H. D. Hochheimer, K. Strossner, W. Honle, B. Baranowski and F. Filipek, *Z. Phys. Chem.*, **143**, 139 (1985).

Chapter 5

Pressure Induced Polymorphism in Hypervalent CsI_3

Alkali halides serve as the simplest and model ionic solid for both static and dynamic high-pressure investigations. They exhibit a wide variety of phenomena like structural phase transition, metallization, superconductivity *etc.,* when subjected to compression and hence have been extensively investigated, both experimentally and theoretically, for their high pressure behaviour. Interest in the alkali halide system has been rekindled by the recent studies which have reported the formation of low symmetry new unconventional stoichiometric compounds with unusual bonding and electronic properties like $NaCl_3$, Na_3Cl, KCl_3, KBr_3, KBr_5 etc., by combining theoretical predictions and diamond anvil cell based high pressure experiments [1-3]. Among the alkali halides, cesium iodide solution is able to dissolve iodine, bromine or chlorine and produce crystals whose chemical analysis could be expressed by the empirical formulas CsI_3, $CsIBr_2$, $CsBrI_2$, $CsICl_2$, CsIBrCl *etc* [4]. Furthermore, CsI_3 and $CsIBr_2$ have been known to adopt an orthorhombic (*SG: Pnma*) structure under ambient conditions which is the same structure as that of alkali trihalides observed in the Na-Cl and K-Br systems, as described in **Chapter 4** [1, 3]. It may also be noted that $NaCl_3$ is stabilized both in orthorhombic (SG: *Pnma)* and cubic (SG: *Pm-3n*) phase in the Na-Cl system; whereas KCl_3 is stabilized both in trigonal (SG: *P*-3*c*1) and cubic (SG: *Pm-3n*) phase in the K-Cl system and KBr_3 is stabilized both in orthorhombic (SG:

Pnma) and trigonal (SG: *P*-3*c*1) phase in the K-Br system. Table 5.1 summarizes the pressure range of phase stability of the various alkali trihalides.

Table 5.1: Summary of the pressure range of phase stability of the various alkali trihalides

Material	Pressure range of stability		
	Orthorhombic (SG: *Pnma*) phase (GPa)	Trigonal (SG: *P*-3*c*1) phase (GPa)	Cubic (SG: *Pm*-3*n*) phase (GPa)
$NaCl_3$ [1]	20 – 48	------	> 48
KCl_3 [2]	------	8 – 20	> 20
KBr_3 [3]	1 – 6	14 – 20	------

As evident from Table 5.1, the absence of trigonal phase in $NaCl_3$, orthorhombic phase in KCl_3 and cubic phase in KBr_3 makes it difficult to arrive at a systematics for the high pressure structural transition sequence in alkali trihalide systems. Very recently, theoretical calculations by Wei *et al* have predicted a *Pm-3n* phase for CsI_3 under high pressure wherein endless linear chain type structure, due to the hypervalence phenomenon of iodine, is reported [5]. Furthermore, their calculations have also revealed a metallic phase for the *Pm-3n* phase of CsI_3. In the light of the above discussion, experimental high pressure investigations on CsI_3 could shed more light on understanding its structural evolution under compression and give better insight in the search for alkali polyhalides.

With this motivation high pressure structural, vibrational and electrical transport investigations on CsI_3 was carried out at high pressure and room temperature. Existence of high purity stable single phase CsI_3 at ambient condition justifies our preference of CsI_3 over other trihalides. In addition, the recent prediction of superconductivity at very low pressure ~ 10 GPa in the predicted cubic phase of CsI_3 has further encouraged us to investigate the high pressure behaviour of CsI_3 [5].

In the present study the high pressure behaviour of CsI_3 at ambient temperature has been investigated through synchrotron based ADXRD up to 29 GPa, Raman spectroscopy up to 25 GPa and Bridgman anvil apparatus based electrical resistance measurements up to 8 GPa to look for the possibility of structural or electronic transition and any possible metallization under compression.

5.1 Structural Details

The structure of CsI_3 consists of Cs^+ and $[I_3]^-$ ions [6-8]. The I_3^- anion belongs to the class of hypervalent compounds which violate the Lewis octet rule [9, 10]. It has a linear geometric structure wherein the central iodine atom shares two electrons with two adjacent iodine atoms by forming a three-centre four-electron (3c-4e) bond and it gets one electron from cesium atom to keep the other two iodine atoms together [11]. In terms of the molecular orbitals, the 3c-4e bond as indicated in Fig. 5.1a can be described by a set of three molecular orbitals (MOs) derived from colinear p-orbitals on each iodine atom and the two lower-energy MOs (bonding and non bonding) are occupied by two electrons each. The structure of CsI_3 was proposed to be based on the simple orthorhombic lattice with space group *Pnma* as shown in Fig. 5.1b [12, 13]. Interestingly, similar crystal structures with space group *Pnma* have been reported for $NaCl_3$ and KBr_3 under non ambient pressure and temperature conditions [1, 3].

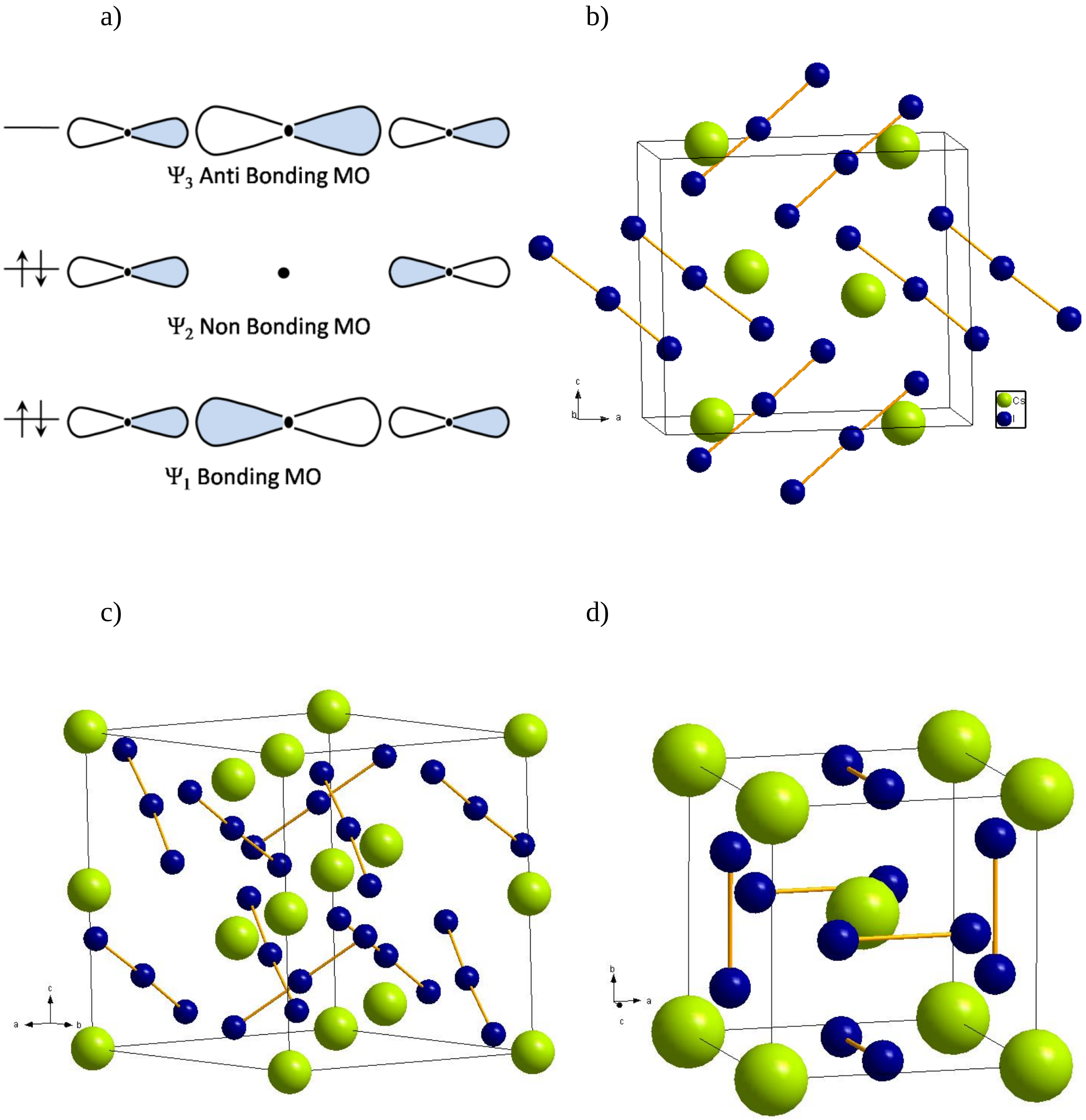

***Fig. 5.1**: a) Molecular orbital representation of 3c-4e bond in I_3^- , Crystal structure of b) orthorhombic (SG: Pnma), c) trigonal (SG: P-3c1) and d) cubic (SG: Pm-3n) CsI_3.*

5.2 Experimental Method

5.2.1 Sample characterization

Polycrystalline CsI_3 of purity (99.9%) was procured commercially from Sigma Aldrich. The sample was characterized using x-ray diffraction. The cell constants and atomic coordinates obtained by Rietveld refinement of the x-ray powder diffraction data confirmed it to be an orthorhombic (*SG: Pnma*, Z = 4) structure with lattice parameters (a = 11.0837(7) Å, b = 6.8443(3) Å, c = 10.0262(6) Å) in good agreement with the literature values [12, 13]. The observed Raman spectrum at ambient condition was consistent with the spectra reported earlier in the literature and the Raman frequencies were found to match well with the reported values [14].

5.2.2 X-ray diffraction

High pressure ADXRD measurements at room temperature were performed on powdered CsI_3 up to 29 GPa on the Xpress beamline at Elettra synchrotron radiation source, Trieste, Italy [15]. A modified Mao-Bell type DAC with diamonds of culet size 400 μm was used with ruby as the internal pressure calibrant. Silicone oil was used as the PTM. It may be noted that 4:1 methanol- ethanol mixture as well as glycerol were tried as the PTM. However the sample was found to dissolve in these two media which led us to select silicone oil as the PTM. The sample chamber was a 150 μm diameter hole drilled in a tungsten gasket of starting thickness 250 μm which was pre-indented to a thickness of 50 μm. Pressure measurement inside the sample chamber was carried out using online ruby fluorescence set up installed at the Xpress beamline [15]. ADXRD diffraction patterns at various pressures were collected using an image plate area detector (MarResearch) employing x-ray wavelength of 0.5007 Å/0.4957Å. The x-ray beam size was constrained using a circular pin hole 30 μm in diameter, which eliminated the diffraction lines from the gasket. The sample to image plate distance was calibrated using LaB_6 and CeO_2 as standards. The x-ray data was collected at small pressure increment steps with a typical exposure time of about 10 minutes. The scanned two-dimensional diffraction images were corrected for image plate tilt and converted to intensity *vs* 2θ profile through radial integration using *FIT2D* software [16]. The lattice parameters of the sample were determined by carrying out full profile Rietveld refinement using GSAS [17]. The parameters refined included the overall scaling factor, Chebyshev polynomial background, lattice constants, Pseudo-Voigt profile function parameters, atomic fractional coordinates and spherical harmonics correction. Multi-phase refinement was carried out and the profile was fitted with the Pseudo-Voigt peak shape with the background fitted by linear interpolation of selected set of points. The fitting procedure was iterative and was terminated on attaining an acceptable weighted R factor or goodness of fit.

5.2.3 Raman measurements

High pressure Raman investigations up to 25 GPa were carried out on polycrystalline CsI_3 using a modified Mao-Bell type DAC and a micro Raman system having a resolution of better than 2 cm^{-1} using a backscattering geometry. Raman signal excited using a 532 nm DPSS laser (Ventus, Laser Quantum), was collected using Jobin Yvon T64000 triple stage Raman spectrograph (with 1800 line grating) equipped with a Peltier cooled CCD detector (Synapse). The sample sensitivity to laser intensity was checked by collecting the ambient Raman spectra at various laser powers as shown in Fig. 5.2, which clearly indicate that the sample remains unaffected by the laser power in the present measurements. The sample loading procedure for these measurements was similar to the one described above for the XRD measurements. Silicone oil was used as the pressure transmitting medium and pressure calibration was carried out using ruby fluorescence technique. The Raman spectra for CsI_3 were recorded at different pressures under quasihydrostatic conditions in the entire spectral region of interest (50– 250 cm^{-1}). The typical laser power and data collection time for the Raman measurements was 4 mW and 10 sec respectively.

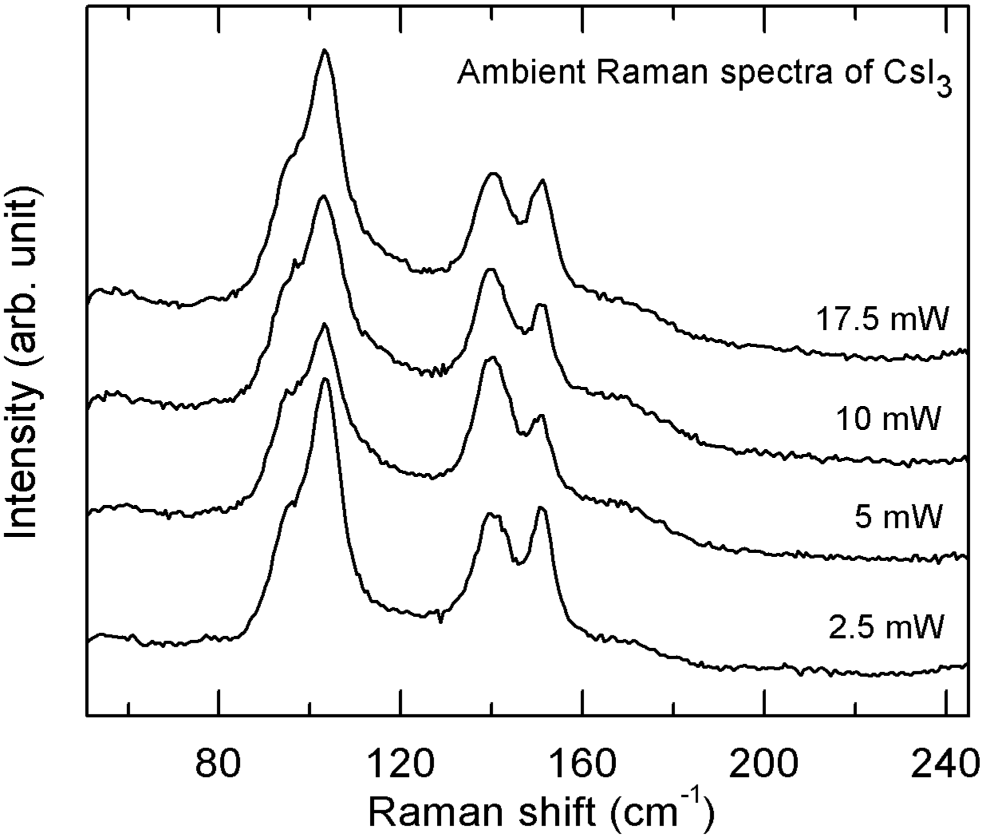

***Fig. 5.2**: The ambient Raman spectra of CsI_3 at various laser powers of the DPSS laser (λ = 532 nm).*

5.2.4 Electrical resistance measurements

High pressure electrical resistance measurements up to 8 GPa was carried out using opposed Bridgman anvil set-up consisting of a 12 mm face diameter tungsten carbide (WC) anvil pair [18]. A pair of pyrophyllite gasket of thickness 200 μm each with a central hole 3 mm in diameter was used to contain the sample. Bismuth was used for the pressure calibration along with steatite as the PTM. Stainless steel wire of 60 µm diameter was used as the leads for the four probe electrical resistance measurements. A well compacted sample pellet was prepared in a pellet making die by application of 2 ton load. Small rectangular shaped sample of approximate dimension 2 mm × 1.5 mm × 0.1 mm was then cut and used for the four probe electrical resistance measurements. Sample was placed directly in contact with the four electrical leads. Thin mylar sheets protected the sample from direct contact with talc and also ensured good electrical contact by preventing talc from entering the sample and electrical leads. A constant current was passed through the two outer leads by a Keithley sourcemeter and the voltage drop across the two inner leads was measured, using a Keithley nanovoltmeter, at each value of pressure with two minutes of pressure soaking time.

5.3 Results and Discussion

5.3.1 High pressure x-ray diffraction

The evolution of diffraction pattern of CsI_3 during pressure increase is depicted in Fig. 5.3. The x-ray patterns could be indexed to the ambient orthorhombic (*SG: Pnma*) phase up to 1.3 GPa. On further pressure increase, new diffraction peaks are seen to emerge along with those of the ambient orthorhombic phase indicating the onset of a structural phase transition above 1.3 GPa. On further increase of pressure, the intensity of the diffraction peaks corresponding to the

Pnma phase reduces and the intensity of the new peaks is seen to build up. The new diffraction peaks could be assigned to a trigonal (*SG: P*-3*c*1) phase by employing *Crysfire* and C*heck Cell* software [19-21]. The ambient and the trigonal phase are seen to coexist up to a pressure of about 10 GPa. Interestingly, this trigonal structure is similar to the structure of KBr_3 and KCl_3 [2, 3].

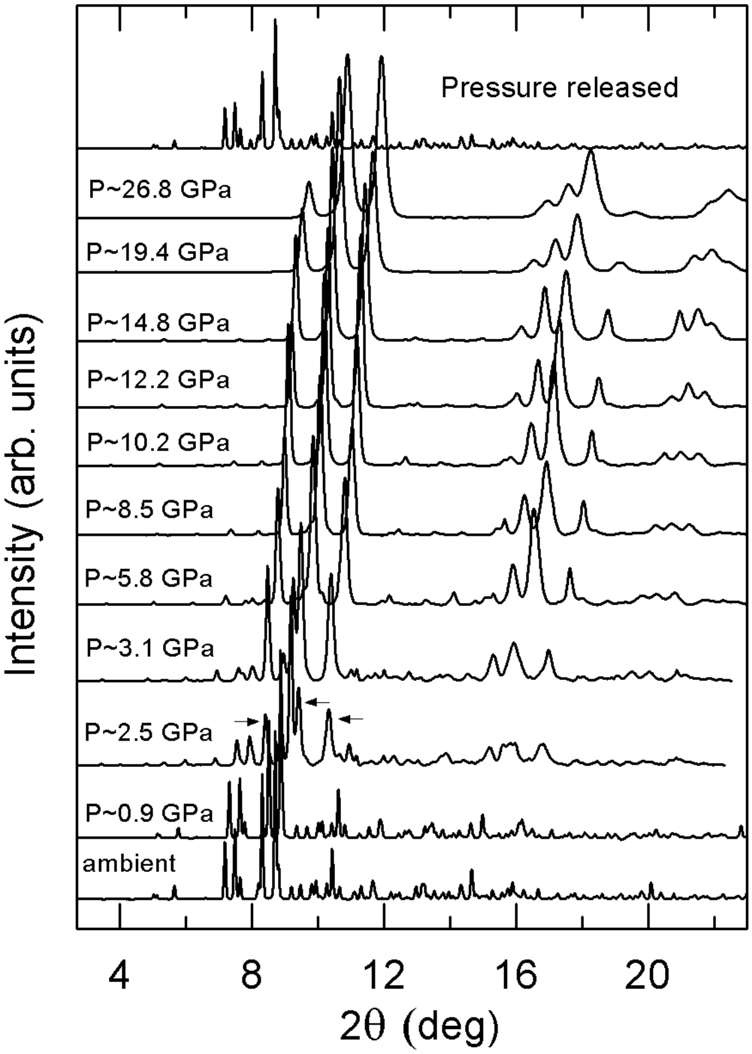

Fig 5.3*: Structural evolution of ADXRD pattern of CsI_3 with pressure. The arrows indicate the new peaks.*

On further pressurization, CsI_3 is found to remain in the trigonal phase till 22.6 GPa. Beyond this pressure, the diffraction peaks associated with the trigonal phase with Miller indices (100), (002), (10-2), (110), (111), (200), (112) *etc.*, are seen to disappear. The disappearance of these diffraction peaks indicate yet another structural phase transition. This new phase could be indexed to a cubic (SG: *Pm*-3*n*) structure and it remains stable up to the highest pressure of 29 GPa achieved in the present study.

The multiphase Rietveld refinement of all the diffraction patterns was carried out to extract information on the structural evolution using GSAS software. A representative Rietveld refinement pattern for the ambient orthorhombic (SG: *Pnma*) phase collected at 0.9 GPa is shown in Fig. 5.4. The Rietveld refined patterns of the trigonal and cubic phase are depicted in Figs. 5.5 and 5.6 respectively. The unit cell parameters and the atomic coordinates extracted for the different phases are tabulated in Table 5.2. Figure 5.1c and 5.1d show the crystal structure of CsI_3 in the trigonal (*SG: P*-3*c*1) and cubic (SG: *Pm*-3*n)* phase.

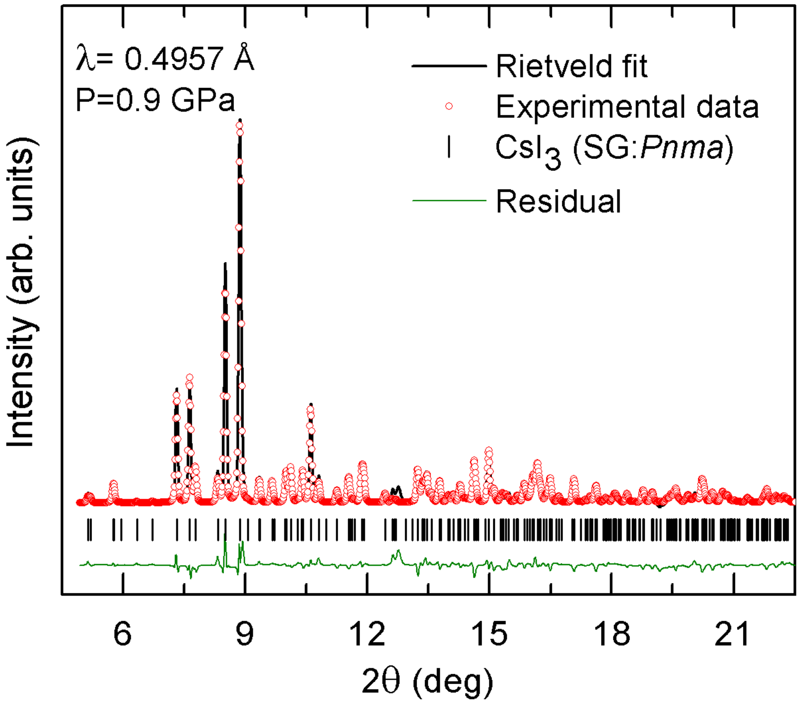

Fig. 5.4: *Rietveld refined ADXRD pattern of orthorhombic (SG: Pnma) CsI_3 at 0.9 GPa. The Rp and wRp factors of the fit are 3.8 and 5.9 %, respectively.*

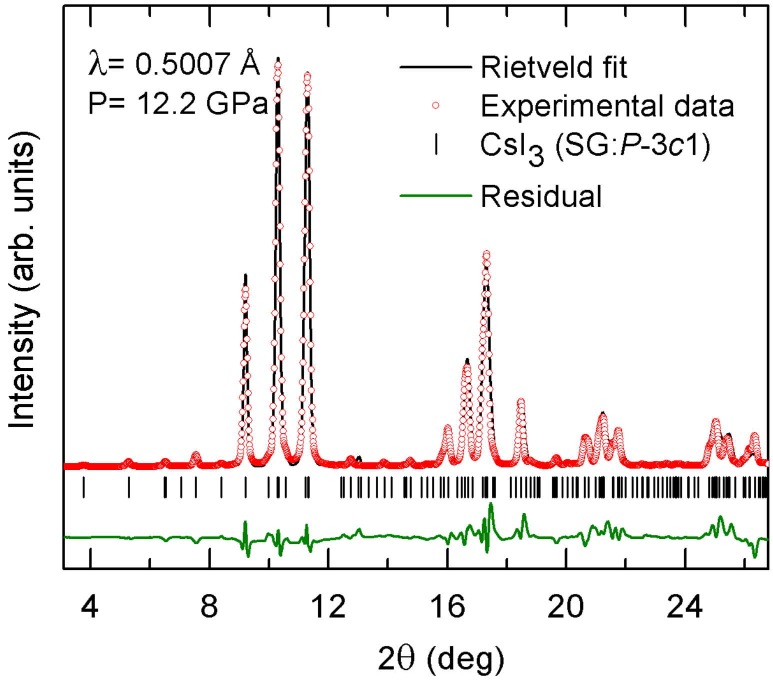

Fig. 5.5: *Rietveld refined ADXRD pattern of trigonal (SG: P-3c1) CsI$_3$ at 12.2 GPa. The Rp and wRp factors of the fit are 3.4 and 5.1 %, respectively.*

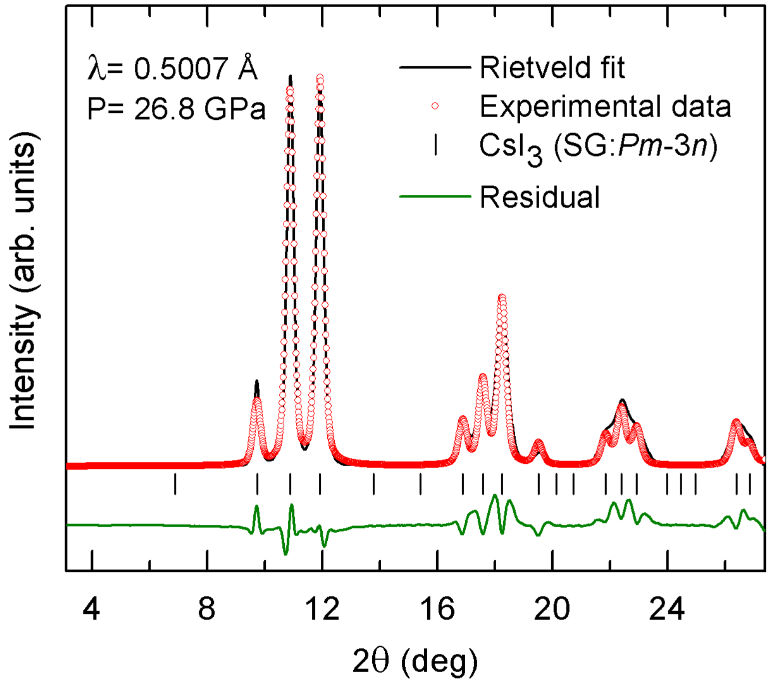

Fig. 5.6: *Rietveld refined ADXRD pattern of cubic (SG: Pm-3n) CsI$_3$ at 26.8 GPa. The Rp and wRp factors of the fit are 2.8 and 3.9%, respectively.*

Table 5.2: Unit cell parameters and atomic coordinates of CsI_3 in the orthorhombic, trigonal and cubic phase.

CsI_3 Phase	Pressure (GPa)	Unit cell Parameters		Atomic coordinates		
		Lattice parameter (Å)	γ			x y z
Orthorhombic (S.G.: *Pnma*)	0.9	a = 10.9148(6) b = 6.6755(3) c = 9.8240(5)	90°	Cs I1 I2 I3	4c 4c 4c 4c	0.8320(5); 0.2500; 0.4672(5) 0.5732(6); 0.2500; 0.7393(6) 0.3804(5); 0.2500; 0.5455(6) 0.1636(6); 0.2500; 0.3535(5)
Trigonal (S.G.: *P*-3*c*1)	12.2	a = 8.7896(4) c = 10.8780(8)	120°	Cs1 Cs2 I1 I2	2b 4d 6f 12g	0.0000; 0.0000; 0.0000 0.3333; 0.6666; 0.8304(14) 0.2405(12); 0.0000; 0.2500 0.3488(6); 0.4294(8); 0.0699(5)
Cubic (S.G.:*Pm*-3*n*)	26.8	a = 5.9046(3)	90°	Cs I	2a 6c	0.0000; 0.0000; 0.0000 0.2500; 0.0000; 0.5000

During decompression, the cubic to trigonal transition is found to be reversible whereas the ADXRD pattern of the pressure released sample, as shown in Fig. 5.7, indicates the coexistence of the trigonal and ambient orthorhombic phase. The variation of volume per formula unit as a function of pressure for the orthorhombic, trigonal and cubic phase is shown in Fig. 5.8.

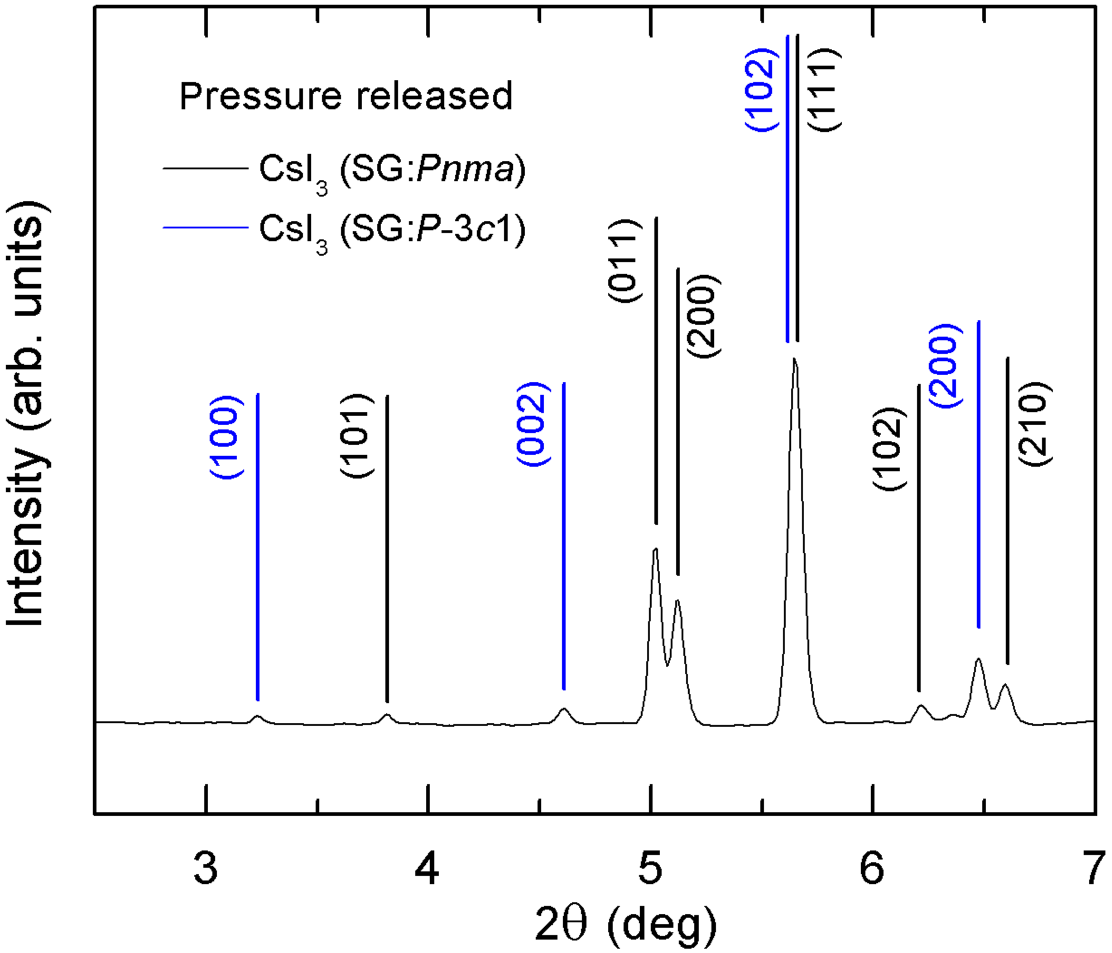

Fig. 5.7: *ADXRD pattern in the 2θ range of 2° to 7° for pressure released CsI_3 depicting the coexistence of orthorhombic and trigonal phases at ambient condition.*

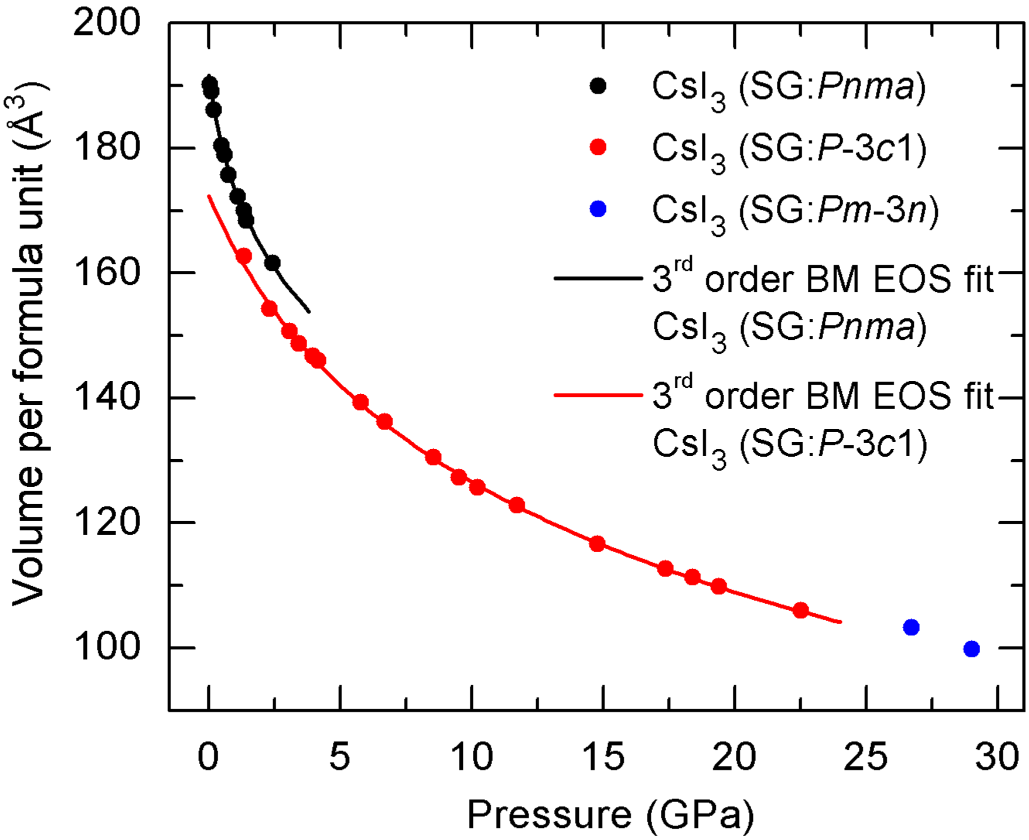

Fig. 5.8: *Variation of volume per formula unit as a function of pressure for all the three phases (orthorhombic, trigonal and cubic) of* CsI_3*. Symbols denote the experimental data points and solid lines denote third order Birch- Murnaghan equation of state fit to the data. Error bars are within symbols.*

It may be noted that the volume at ambient pressure (V_o) employed for the trigonal phase was obtained by extrapolating the P-V data to ambient pressure. The bulk modulus and its pressure derivative for the orthorhombic (*SG: Pnma*) and trigonal (*SG: P-3c1*) phases were calculated by a third order Birch–Murnaghan equation of state [22] fit to the P-V data represented by

$$P(V) = (3/2)B_o [(V_o/V)^{7/3} - (V_o/V)^{5/3}] \{1 + 3/4(B' - 4)[(V_o/V)^{2/3} - 1]\} \qquad (5.1)$$

where B_o and V_o are the ambient pressure bulk modulus and volume respectively, B′ is the pressure derivative of bulk modulus and V is the volume at pressure P. The results of the P-V data fit are tabulated and compared with the analogous compound reported in the K-Br system in Table 5.3. The bulk modulus for the cubic phase could not be determined because of fewer experimental data points.

Table 5.3: Unit cell volume (V_0 in $Å^3$), bulk modulus (B_0 in GPa) and pressure derivative of bulk modulus (B′) obtained by fitting the third order Birch-Murnaghan equation of state to the PV data of orthorhombic and trigonal CsI_3. The corresponding data for KBr_3 [3] are also tabulated for comparison.

	CsI_3		KBr_3 Ref. [3]	
	Pnma	*P*-3*c*1	*Pnma*	*P*-3*c*1
V_0 ($Å^3$)	766.4(16)	1034(6)	534.37	770.73
Bulk modulus B_0 (GPa)	5.6(6)	17.7(9)	11.8	15.5
B′	12(2)	3.94(12)	4.0	4.55

Pressure dependencies of the normalized lattice parameters for the orthorhombic (*SG: Pnma*) and trigonal (*SG: P-3c1*) phases are plotted in Figs. 5.9 and 5.10 respectively. The fitted linear modulus and their pressure derivatives are summarized in Table 5.4. It is evident from Table 5.4 that, in the orthorhombic phase, the largest unit cell axis (a- axis) is the least compressible whereas the smallest unit cell axis (b-axis) is the most compressible.

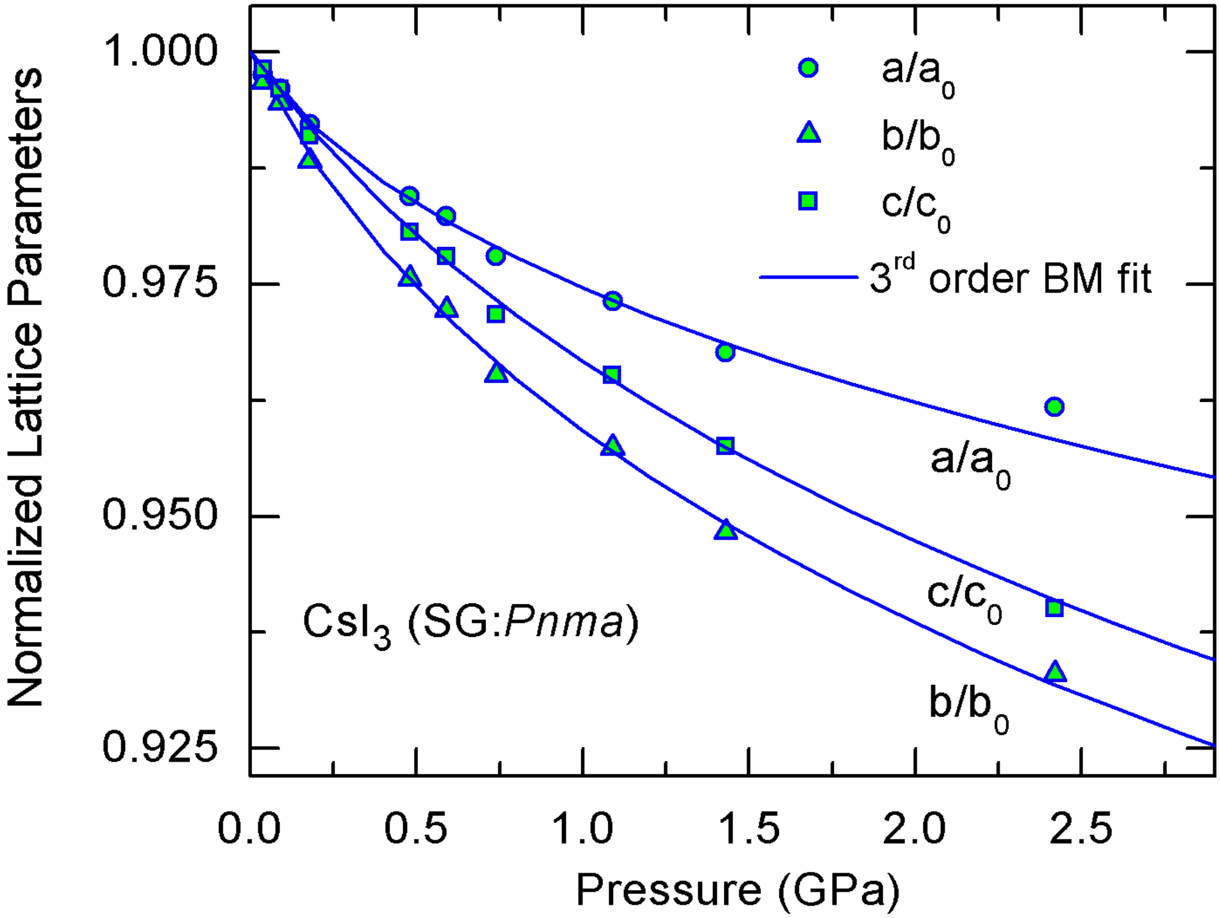

Fig. 5.9: *Variation of normalized lattice parameters of CsI$_3$ in the orthorhombic (SG: Pnma) phase with pressure. The symbols and solid line denote the experimental data points and the third order Birch-Murnaghan fit to the experimental data respectively. Error bars are within symbols.*

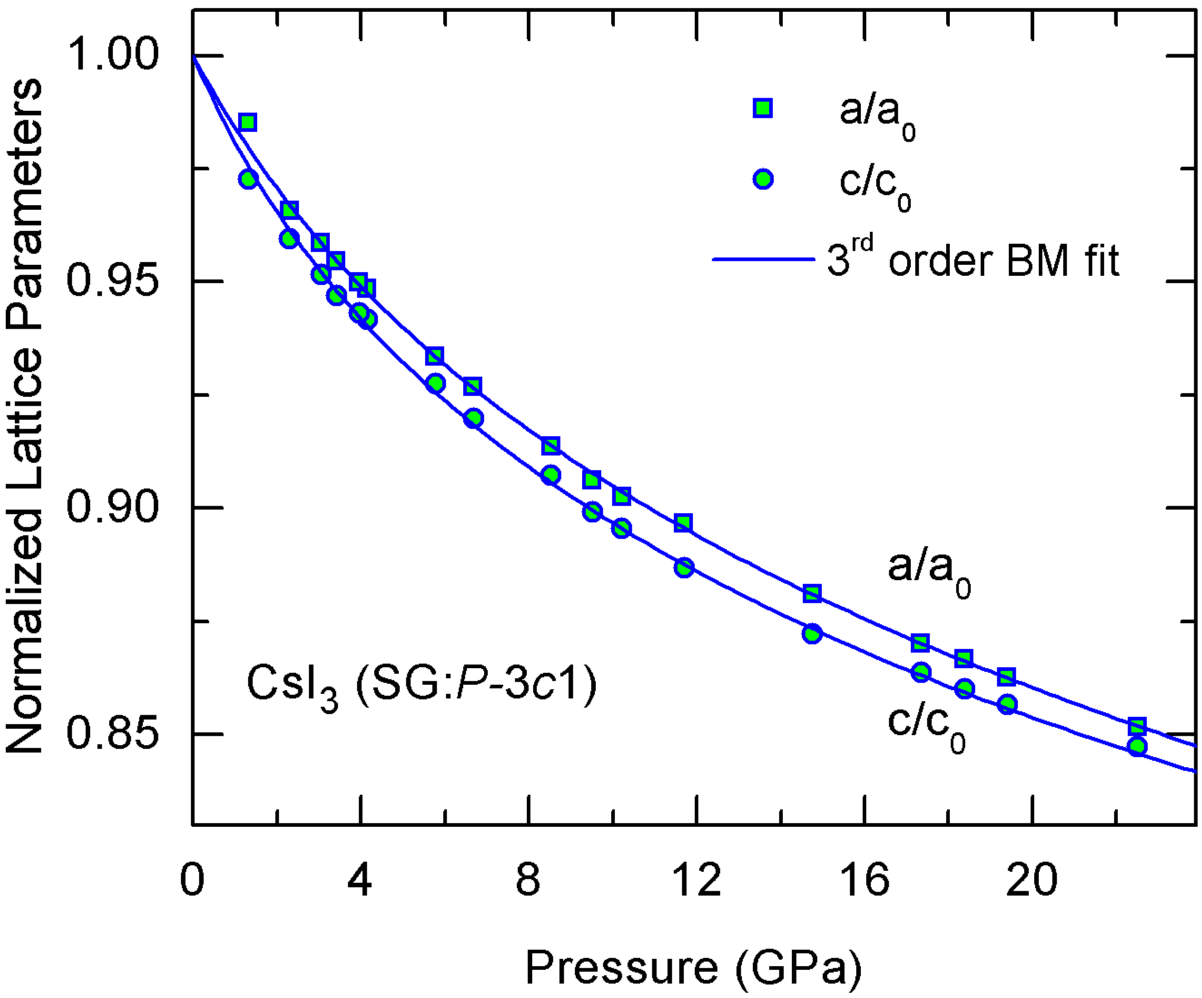

Fig. 5.10: *Variation of normalized lattice parameters of CsI$_3$ in the trigonal (SG: P-3c1) phase with pressure. The symbols and solid line denote the experimental data points and the third order Birch-Murnaghan fit to the experimental data respectively. Error bars are within symbols.*

Table 5.4: Unit cell parameters (a_0, b_0, c_0 in Å), linear modulus (M_0 in GPa) and pressure derivative of linear modulus (M′) at ambient pressure obtained by fitting the third order Birch-Murnaghan equation of state to the pressure variation of lattice parameters of orthorhombic and trigonal CsI$_3$.

CsI$_3$	a_0 (Å)	M_{0a} (GPa)	M_a'	b_0 (Å)	M_{0b} (GPa)	M_b'	c_0 (Å)	M_{0c} (GPa)	M_c'
Pnma	11.111(14)	18(6)	77(36)	6.866(6)	13.7(15)	29(5)	10.045(7)	19.9(17)	24(4)
P-3c1	9.846(16)	57(3)	11.4(3)	9.846(16)	57(3)	11.4(3)	12.32(6)	45(6)	12.8(10)

The layered structure along b-axis explains the high compressibility in this direction and resultant low linear modulus for b-axis whereas the presence of large number of sigma bonds in ac-plane explains the low compressibility of a-axis and c-axis. In the trigonal phase, the c-axis is seen to be little more compressible than the a-axis and b-axis.

5.3.2 High pressure Raman spectroscopy

Figure 5.11 shows the evolution of Raman spectra of CsI$_3$ with pressure. The Raman spectra of CsI$_3$ at ambient condition, as depicted in Fig. 5.11, is in good agreement with the reported values [14]. There are five distinct Raman modes observed at 94, 102, 138.7, 149 and

167.5 cm^{-1} at ambient condition. The Raman mode at 94 and 102 cm^{-1} could be attributed to the symmetrical stretching vibration of the I_3^- units. The Raman modes at 138.7 and 149 cm^{-1} correspond to the antisymmetrical stretching vibration of the I_3^- units.

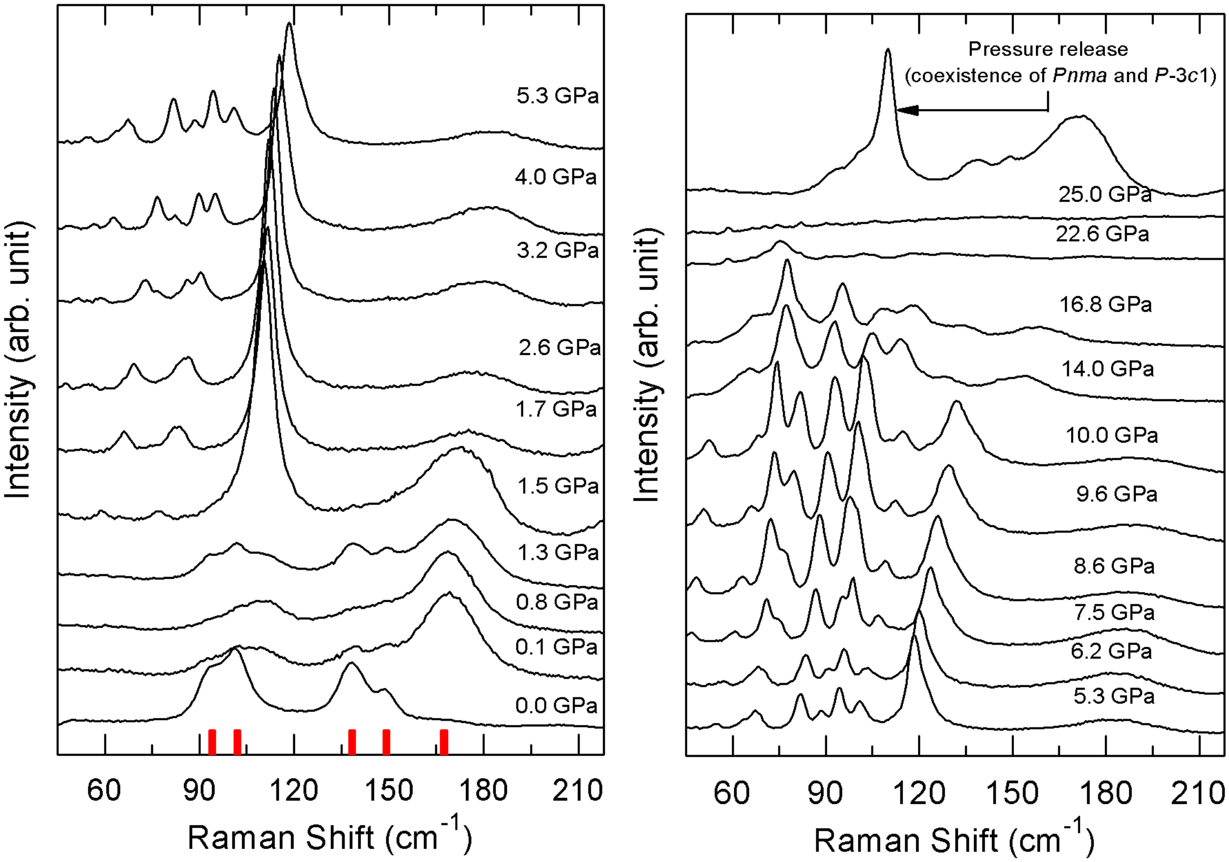

Fig. 5.11: *Pressure evolution of Raman spectra of CsI_3. The bars indicate the Raman modes at ambient conditions.*

With increasing pressure, all the Raman mode frequencies show a positive slope with pressure. Above 1.3 GPa, abrupt changes in the Raman spectra are observed and additional Raman modes appear at 59.0, 77.0 and 110.3 cm^{-1}. The appearance of new Raman modes above 1.3 GPa indicate the onset of a phase transition. This new phase has been attributed to the trigonal (SG:

P-3c1) phase as observed in our present ADXRD measurements. On further increase of pressure, the highest frequency Raman mode corresponding to the *Pnma* phase is seen to survive upto 10 GPa along with the Raman modes corresponding to the trigonal phase, confirming coexistence of both the phases in the pressure range of 1.3 to 10 GPa.

The pressure dependence of mode frequencies is shown in Fig. 5.12. Raman mode frequencies at ambient pressure and coefficient of their pressure derivatives obtained by linear or quadratic fit are summarized in Table 5.5. Above 4.0 GPa, a splitting is observed for the Raman mode at 107 and 118 cm^{-1}. In addition, major intensity redistribution is observed in the overall Raman spectra. It is evident from Fig. 5.12 that all the Raman modes show a change of slope above 4.0 GPa. Hence the various attributes around 4.0 GPa such as slope change and mode splitting indicate yet another phase transition in CsI_3. At still higher pressures, the intensities of all the Raman modes are found to decrease with increasing pressure. Above 13 GPa, the mode at 77 cm^{-1} is found to soften and a complete loss of Raman intensity is observed above 22.6 GPa indicating a phase transformation to a Raman inactive phase or amorphization or band gap closure/collapse. However, based on our ADXRD measurements this transition has been attributed to the structural phase transition to the cubic (SG: *Pm*-3*n)* phase. It may be noted that this cubic phase in CsI_3 has been reported to be a metallic phase by theoretical calculation by Wei *et al* [5]. Similar crystal structure has also been reported for $NaCl_3$ [1]. Reappearance of Raman modes during pressure release reconfirms the reversible nature of observed phase transition. The pressure released pattern shows Raman modes of both trigonal and ambient orthorhombic phase corroborating our ADXRD results. The existence of trigonal phase upon pressure release suggest small energy difference between the trigonal and the orthorhombic phase.

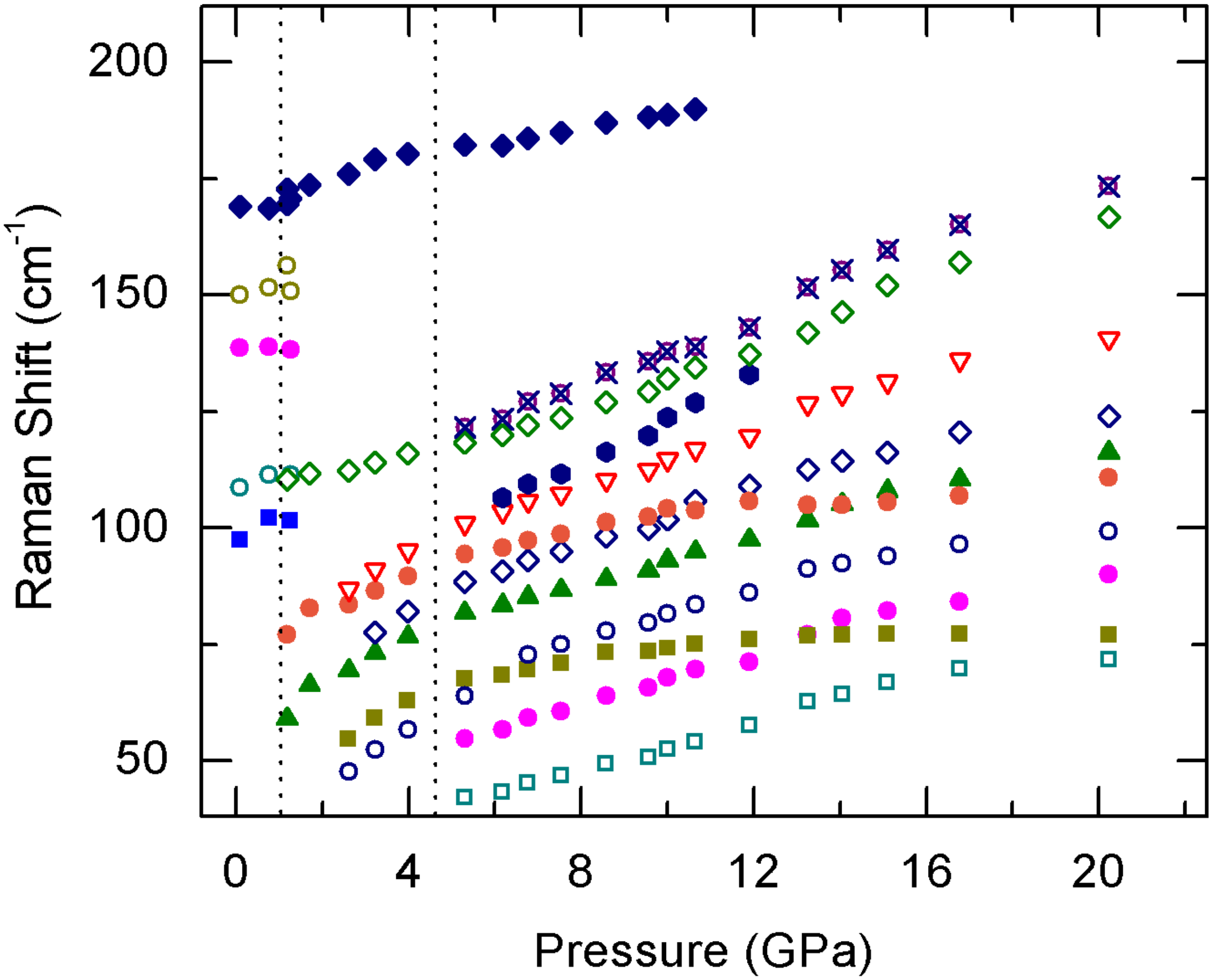

Fig. 5.12: *Variation of Raman mode frequencies of CsI$_3$ with pressure. Dotted vertical lines are placed at phase transition boundary. Error bars are within symbols.*

Table 5.5: Raman mode frequencies of CsI$_3$ at ambient pressure (ω_0) and their pressure coefficients for the orthorhombic and trigonal phase obtained by a linear or quadratic fit.

Orthorhombic (*SG:Pnma*) phase in the pressure range of 0.1MPa to 1.3 GPa		**Trigonal (*SG:P-3c1)* phase in the pressure range of 1.3 to 4.0 GPa**		**Trigonal (*SG:P-3c1*) phase in the pressure range of 4.0 to 20 GPa**		
ω (cm^{-1}) at 0.1 MPa	dω$_0$/dp (cm^{-1}/GPa)	ω (cm^{-1}) at 2.6 GPa	dω$_0$/dp (cm^{-1}/GPa)	ω (cm^{-1}) at 5.3 GPa	dω$_0$/dp (cm^{-1}/GPa)	d^2 ω$_0$/dp^2 (cm^{-1}/GPa^2)
94	3.7(24)	47.7	6.5(5)	42	2.3(1)	------
102	2.5(12)	54.7	5.8(7)	54.6	2.5(1)	------
138.7	-0.3(4)	69.3	5.9(8)	63.8	5.5(4)	-0.12(1)
149	0.7(12)	73.2	6.1	67.5	2.7(1)	-0.081(6)
167.5	1.9(1)	83.5	4.0(7)	81.8	2.5(1)	------
		86.9	5.9(5)	88.4	2.6(1)	------
		112.2	1.9(3)	94.3	3.8(4)	-0.12(2)
				101.0	2.9(1)	------
				104.4	4.6(2)	------
				118.2	3.4(1)	------
				121.7	3.7(1)	------

5.3.3 High pressure electrical resistance measurements

Figure 5.13 depicts the variation of electrical resistance with pressure for CsI$_3$. Initially the resistance decreases with pressure up to 1.6 GPa and beyond this pressure it starts increasing.

This change in the slope is attributed to the orthorhombic to trigonal phase transition observed in the XRD and Raman measurements. On further increase of pressure, the resistance continues to increase with a plateau like region up to 4.5 GPa beyond which there is an exponential increase in the resistance and around 8 GPa the resistance value exceeds the limit of the measuring instrument. This sharp increase in the resistance, in the absence of any structural phase transition as observed in our XRD studies, is indicative of major electronic rearrangements. The changes observed in the Raman spectra around 4.0 GPa also corroborate the present observation. It is also noteworthy that a reversible behaviour is observed on pressure release consistent with our Raman and ADXRD measurements.

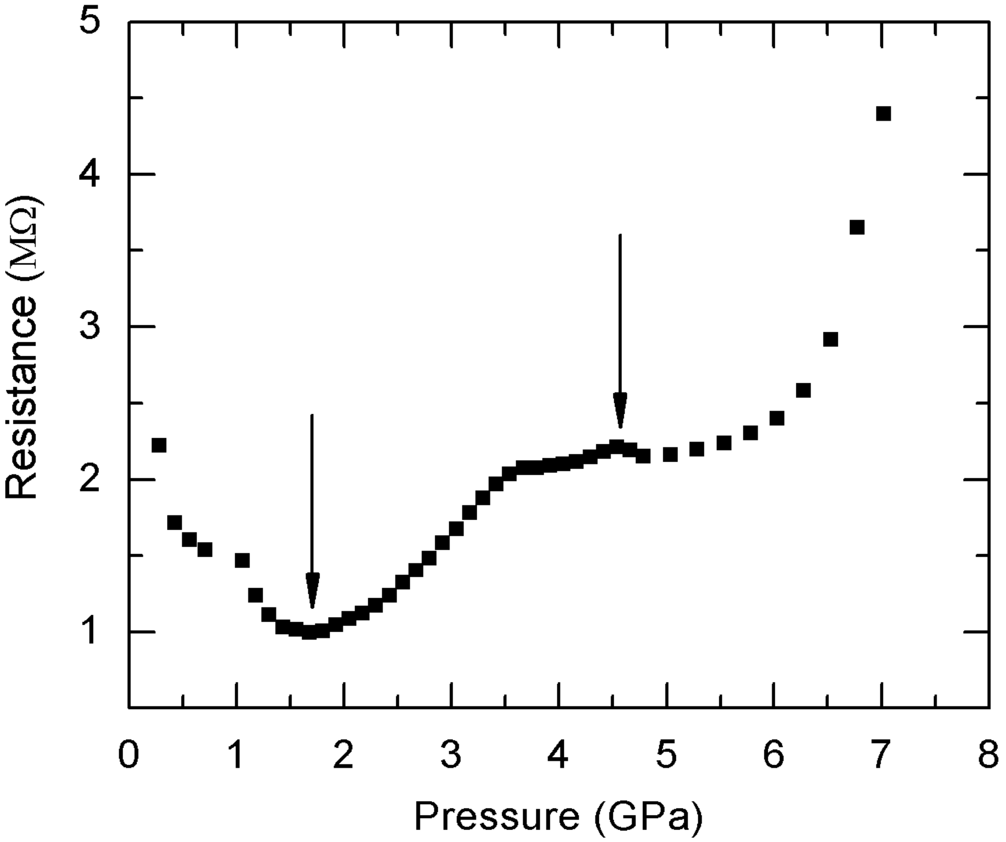

Fig. 5.13: *Variation of electrical resistance of CsI_3 with pressure. Arrows denote the transition points.*

A significant feature of the present study is the observation of a transition around 1.3 GPa in the x-ray measurements which is well corroborated by Raman and electrical resistance measurements. Hence we attribute this to a first order structural transition from an orthorhombic (SG: *Pnma*) to a trigonal (SG: *P*-3*c*1) phase accompanied with volume discontinuity of 4.5%. It may also be noted that although Raman spectra show significant changes around 4.0 GPa, our x-ray diffraction measurements indicate no signature of any structural phase transition around this pressure. Furthermore, an anomaly is also observed in the electrical resistance measurements. The P-V data as shown in Fig. 5.8 do not reveal any discontinuity around 4.0 GPa. This leads us to believe that this transition could be an electronic transition.

In order to better understand the anomaly in the Raman and resistance data we have analyzed the experimental P-V data for the trigonal phase through the use of the universal equation of state (UEOS) calculated by fixing V_o to the extrapolated value at ambient pressure [23]. The UEOS can be represented as follows:

$$\ln H = \ln[PX^2/3(1-X)] = \ln B_0 + \eta\,(1-X) \qquad (5.2)$$

where $X=(V/V_o)^{1/3}$, P is the pressure, V_o is the ambient volume and η is related to B_o' by

$$\eta = 3(B_o'-1)/2 \qquad (5.3)$$

In particular, electronic transition will lead to a deviation from linearity in the UEOS [23, 24]. As observed from the UEOS plot shown in Fig. 5.14, there is indeed a change of slope corresponding to a pressure of ~ 4.1 GPa ((1-X) ~ 0.06). This pressure is in good agreement with the pressure at which the Raman modes show splitting and is also consistent with the anomaly observed between 4 and 5 GPa in the electrical resistance behaviour with pressure. This leads us to conclude that CsI_3 shows an electronic transition at ~ 4.0 GPa.

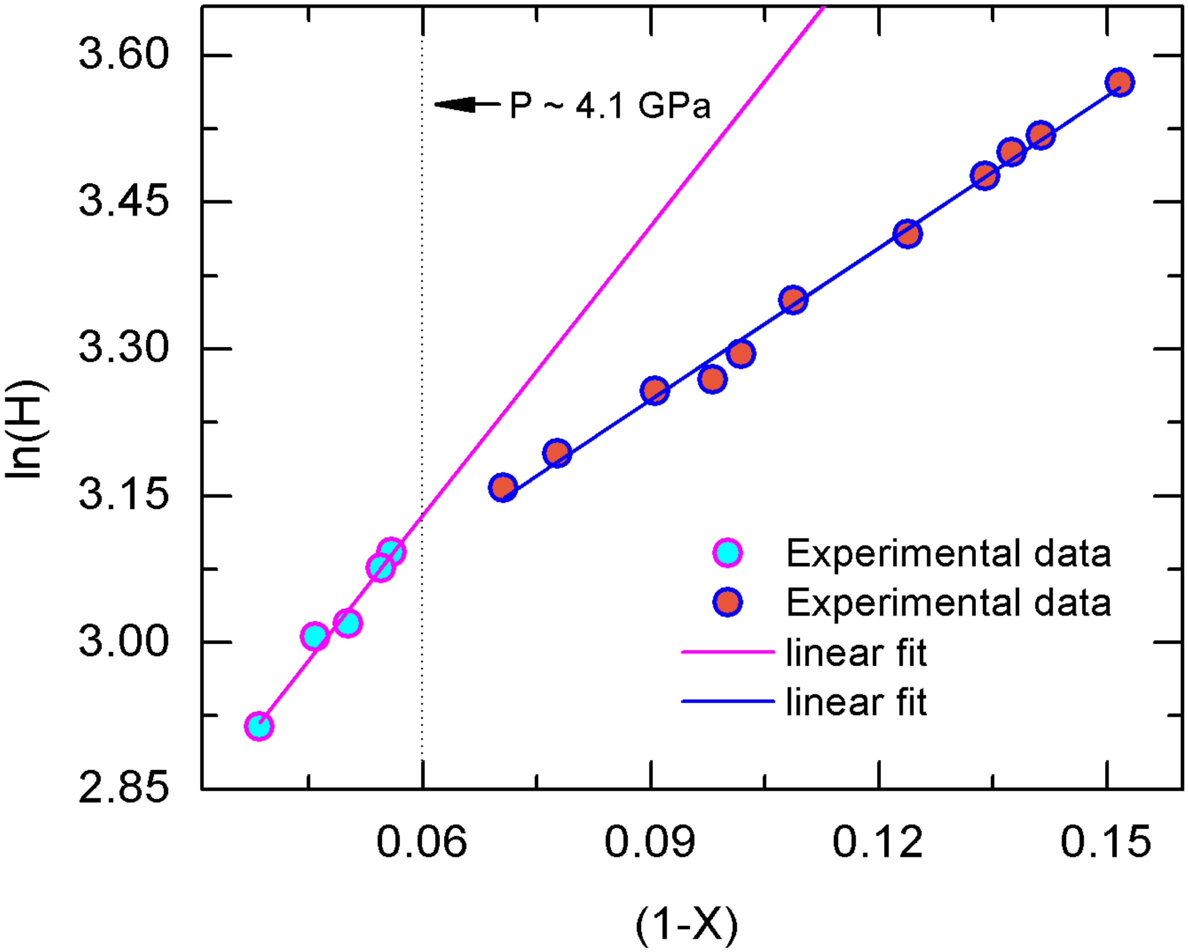

Fig. 5.14: *Universal equation of state (i.e., lnH vs (1-X) where H= $[PX^2/3(1-X)]$ and X= $(V/V_o)^{1/3}$ for CsI_3 in the trigonal phase. The dotted line denotes the electronic transition pressure.*

It is noteworthy that up to now all the high pressure phases of all alkali trihalide ($NaCl_3$, KBr_3, KCl_3) have been reported to decompose on pressure release to ambient conditions [1-3]. The recovery of CsI_3 in the metastable high pressure phase (SG: *P*-3*c*1) at ambient conditions thus makes CsI_3 unique in whole alkali polyhalogen system reported so far. This may have considerable impact on the ongoing search and synthesis of alkali polyhydrides, which are also considered to be potential candidates to show high temperature superconductivity [25, 26].

5.4 Conclusions

The ambient temperature high pressure behaviour of CsI_3, investigated using three complimentary high pressure techniques *viz.*, ADXRD, Raman and electrical resistance measurement, indicate three phase transitions up to 29 GPa. The onset of the ambient orthorhombic to trigonal structural phase transition is found to occur above 1.3 GPa and is associated with a volume discontinuity of 4.5%. The coexistence of the orthorhombic and trigonal phase is observed up to 10 GPa. The stability region of the trigonal phase is found to be up to 22.6 GPa above which the trigonal phase transforms to a cubic phase which remains stable till the maximum pressure of 29 GPa achieved in this study. The present study has thus revealed a three phase structural sequence in alkali trihalides, *viz.*, orthorhombic (*SG: Pnma*) to trigonal (*SG:P*-3*c*1) to finally cubic phase (*SG:Pm*-3*n*). In addition to the structural phase transitions, an electronic transition has also been observed around 4.0 GPa. The results of the present investigation thus throw light on the structural transition sequence of alkali polyhalides as a whole and provide useful inputs in understanding and standardizing the pressure effects on the alkali trihalide systems. The observation of a trigonal phase intermediate between the orthorhombic and the cubic phase in our study as against the theoretical prediction of a direct orthorhombic to cubic phase transition at 7.8 GPa will encourage further improvements in computational models for detailed theoretical investigation of alkali polyhalides.

References

[1] W. Zhang, A. R. Oganov, A. F. Goncharov, Q. Zhu, S. E.Boulfelfel, A. O. Lyakhov, E. Stavrou, M. Somayazulu, V. B. Prakapenka and Z. Konopkova, *Science*, **342**, 1502 (2013).

[2] W. Zhang, A. R. Oganov, Q. Zhu, S. S. Lobanov, E. Stavrou and A. F. Goncharov, *Sci. Rep.*, **6**, 26265 (2016).

[3] N. N. Patel, Ashok K. Verma, A. K. Mishra, M. Sunder and S. M. Sharma, *Phys. Chem. Chem. Phys.*, **19**, 7996 (2017).

[4] G.L. Clark, *Proc. Nat. Acad. Sci.*, **9**, 117 (1923).

[5] S. Wei, J. Wang, S. Deng, S. Zhang and Q. Li, *Sci. Rep.*, **5**,14393 (2015).

[6] G. L. Breneman and R. D. Willett, *Acta Cryst. B* **25**, 1073 (1969).

[7] C. L. Rose and S. Mooney, *Acta Cryst.*, **12**, 187 (1959).

[8] J.C. Slater, *Acta Cryst.* **12**, 197 (1959).

[9] J.I. Musher, Angew. *Chem. Int. Ed.*, **8**, 54 (1969).

[10] G.N. Lewis, *J. Am. Chem. Soc.*, **38**, 262 (1916).

[11] G.C. Pimentel, *J. Chem. Phys.*, **19**, 446 (1951).

[12] R.M. Bozorth and L. Pauling, *J. Am. Chem. Soc.* **47**, 1561 (1925).

[13] H.A. Tasman and K.H. Boswijk, *Acta Cryst.*, **8**, 59 (1955).

[14] K. Odagi, H. Nakayama and K. Ishii, *Bull. Chem. Soc. Jpn.*, **63**, 3277 (1990).

[15] A. Lausi, M. Polentarutti, S. Onesti, J.R. Plaisier, E. Busetto, G. Bais, L. Barba, A. Cassetta, G. Campi, D. Lamba, A. Pifferi, S. C. Mande, D. D. Sarma, S. M. Sharma and G. Paolucci, *Eur. Phys. J. Plus*, **43**,130, (2015).

[16] A. P. Hammersley, S. O. Svensson, M. Hanfland, A. N. Fitch and D. Hausermann, *High Press. Res.*, **14**, 235 (1996).

[17] A. C. Larson and R. B. Von Dreele, *Los Alamos National Laboratory Report LUAR* , **86**, 748 (1994).

[18] P. W Bridgmann, *J. Appl. Phys.*, **12**, 461 (1941).

[19] R. Shirley, *The Crysfire 2002 System for Automatic Powder Indexing: User's Manual*, (2002).

[20] P. E.Werner, L. Eriksson and M. Westdahl, *J. Appl. Cryst.* **18**, 367, (1985).

[21] J. Laugier and B. Bochu, *CHEKCELL Graphical indexing and spacegroup assignment helper tool*, (2002).

[22] F. Birch, *J. Geophys. Res.*, **83,** 1257 (1978).

[23] J.H. Rose, J.R. Smith, F. Guinea and J. Ferrante, *Phys. Rev. B* **29**, 2963 (1984).

[24] S.K. Sikka, *Phys. Rev. B* **38,** 8463 (1988).

[25] P. Baettig and E. Zurek, *Phys. Rev. Lett.*, **106**, 237002 (2011).

[26] J. Hooper and E. Zurek, *J. Phys. Chem. C*, **116**, 13322 (2012).

Chapter 6

Summary and Future Scope

6.1 Summary

The studies presented in this thesis highlight the significance of laser heating in material synthesis and investigation of the phase behaviour of materials at high pressure high temperature (HPHT). The work included can be broadly classified as follows

(1) Development of instrumentation for HPHT laser heating of materials.

(2) Determination of melting curve of some elemental systems and compounds at HPHT.

(3) HPHT synthesis of some novel and counterintuitive materials.

The instrumentation part of the thesis includes the design, development and standardization of a single sided laser heated diamond anvil cell (LHDAC) in an off-axis angular heating geometry incorporating spectroradiometry for temperature determination. Three melting criteria were implemented in the LHDAC facility, *viz.,* flash heating method, laser speckle method and temperature plateau method. In addition, a cryo-loader was designed for cryogenic loading of liquefied argon, as the pressure transmitting medium, in the DAC.

Establishment of melting curve of elements and compounds is of considerable importance in applied physics and geophysics. As a part of this thesis work, the high pressure melting curve of KBr was determined up to 24 GPa and compared with available literature data. The first experimental report of high pressure melting curve of Os up to 35 GPa has also been reported is this thesis. The study was aimed at resolving the discrepancies in melting curve and melting slope at ambient pressure reported by the various theoretical melting studies. The experimental melting slope was used for the analytical determination of Grüneisen parameter ($\gamma(\rho)$).

LHDAC is an invaluable tool for HPHT synthesis of new and novel materials. The feasibility of the LHDAC facility, developed as a part of this thesis work, for material synthesis has been demonstrated by the HPHT synthesis of GaN by direct reaction of Ga metal with N_2 at 9 GPa and 1925 K and the HPHT synthesis of Mo_2N at 5 GPa and 1500 K using Mo metal and N_2 as precursors.

In addition, synthesis of two new counter-intuitive stoichiometric compounds, *viz.,* KBr_3 and KBr_5, in K-Br system is a major outcome of this thesis. A room temperature high pressure chemical reaction between KBr and Br_2 resulted in the formation of an orthorhombic KBr_3 (*SG: Pnma*) at ~ 2.0 GPa. Further compression led to the formation of a monoclinic KBr_5 (*SG:* $P2_1$) at ~ 6.0 GPa. The stoichiometry and crystal structure of this compound was determined using ADXRD and Raman measurements in conjunction with *ab-initio* evolutionary structural search. It may be noted that KBr_5 is the first ever compound synthesized in 1:5 stoichiometry in whole alkali–halogen system. HPHT experiments on KBr_5 using LHDAC facility, carried out in pressure range of 14-20 GPa showed that KBr_5 decomposes above 1500 K in to KBr_3 and Br_2

with large drop in sample chamber pressure and KBr_3 synthesized in laser heating experiments was stabilized in trigonal (*SG: P-3c1*) structure rather than orthorhombic (*SG: Pnma*) structure.

Ambient temperature high pressure ADXRD, Raman and electrical resistance measurements were also carried out on the alkali trihalide "CsI_3" up to 29, 25 and 8 GPa respectively. The studies confirmed three phase transitions up to 29 GPa under quasihydrostatic conditions. The ambient orthorhombic phase was found to transform to a trigonal structural phase above 1.3 GPa with a volume discontinuity of 4.5%. The stability region of the trigonal phase was found to be up to 22.6 GPa. At further higher pressure the trigonal phase was found to transform to a cubic phase which remained stable till the maximum pressure of 29 GPa achieved in this study. Furthermore, an electronic transition was also observed around 4.0 GPa. The study has thus revealed a three phase structural sequence in alkali trihalides, *viz.*, orthorhombic (*SG: Pnma*) to trigonal (*SG:P*-3*c*1) to finally cubic phase (*SG:Pm*-3*n*) in CsI_3. These results throw light on the structural transition sequence of alkali polyhalides and provide useful inputs in understanding the pressure effects on the alkali trihalide systems.

6.2 Future Scope

The work reported in this thesis highlight the importance of HPHT LHDAC facility for investigation of the phase behaviour of materials and for synthesis of novel materials. Future extension could include incorporation of double sided heating in present LHDAC facility. This would minimize the axial temperature gradient in the heated sample. Also, the Gaussian profile of TEM_{00} mode of IR laser introduce large radial temperature gradient, which has been minimized in the present study by defocusing the incident IR laser in the adapted angular geometry. The incorporation of a focal-πshaper to get flat top IR laser profile at the sample position in 180° heating geometry could also be another desirable extension.

The present work has also shown that a variety of diagnostic techniques are required to understand the behaviour of materials at non ambient pressure and temperature conditions. An important aspect would be to couple the LHDAC facility to important diagnostic techniques like ADXRD at the ECXRD synchrotron beam line at Indus-2, Indore and Raman spectroscopy for *in situ* characterization of the synthesized samples. This would also be advantageous for detection and characterization of unquenchable HPHT phases.

A significant aspect of HPHT research is the investigation of phase behaviour of interesting materials. The melting curve of the refractory metal “Os” has been experimentally established for the first time up to 35 GPa. Future work could include the investigation of melting behaviour of other presently unexplored refractory metals like Iridium (Ir) and Hafnium (Hf).

Furthermore, material synthesis at HPHT also provides a unique opportunity to study high pressure chemistry and validation of octet rule at extreme conditions. The access to new chemical pathways for the synthesis of counter-intuitive compounds in LHDAC would be beneficial for realization of alkali polyhalides in yet unexplored alkali-halogen systems, like Cs-Cl, Cs-F, Cs-Br *etc*.

A. Diamond Anvil Cell

Diamond anvil cell (DAC) is a revolutionary compact device, which can fit into the palm of one’s hand, capable of generating very high static pressures of a few Mbars in laboratory. It exploits the fact that diamond is hardest material known to mankind, with a bulk modulus of 440 GPa, to achieve extremely high pressures. The basic principle of the DAC as shown in Fig. A.1 is very simple. The sample placed in a hole drilled in metallic gasket filled with a pressure transmitting fluid is squeezed between the flat parallel faces of two opposed diamond anvils (DA) by applying an uniaxial load, which pushes the two opposed anvils together. Generation of high pressure is based on the principle of massive support.

DAs are made from commercially available jewel cut diamonds by polishing off the tip of each diamond to generate a flat circular culet. Apart from jewel cut diamond many other custom made anvil designs, as shown in Fig. A.2, are also used in DAC.

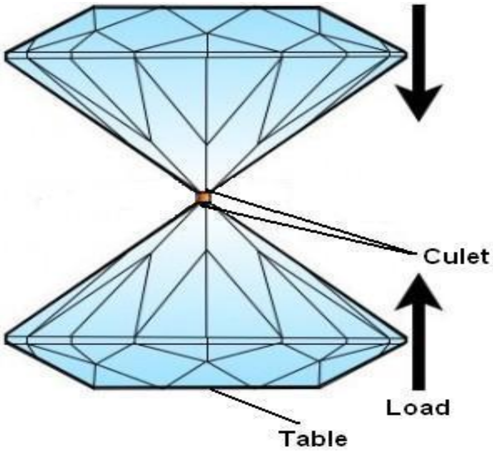

Fig. A.1: *Schematic diagram of DAC [1].*

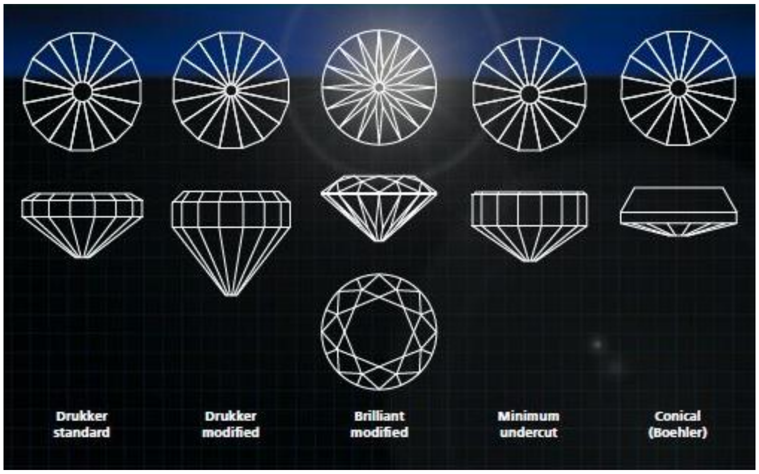

Fig. A.2: *Various designs of DA used in DAC for high pressure generation [1].*

Fig. A.3: *Various designs of DAC used for high pressure generation [2].*

The variations in the DAC as illustrated Fig. A.3 arise from the different ways in which the force-generating and the anvil-alignment mechanisms are designed. DAC used for experiments presented in this thesis is of Mao-Bell design and are shown in Fig. A.4. In this design one diamond with culet diameter d in mm, is mounted on the piston and another on the cylinder of the DAC as shown in Fig. A.5. The maximum pressure achieved by DAC for a given culet size is estimated by the following

$$P_{max} = 12.5/d^2 \qquad \text{(A1)}$$

For practical purpose $P = 0.8P_{max}$ is considered as a safe limit for diamond in high pressure DAC experiments.

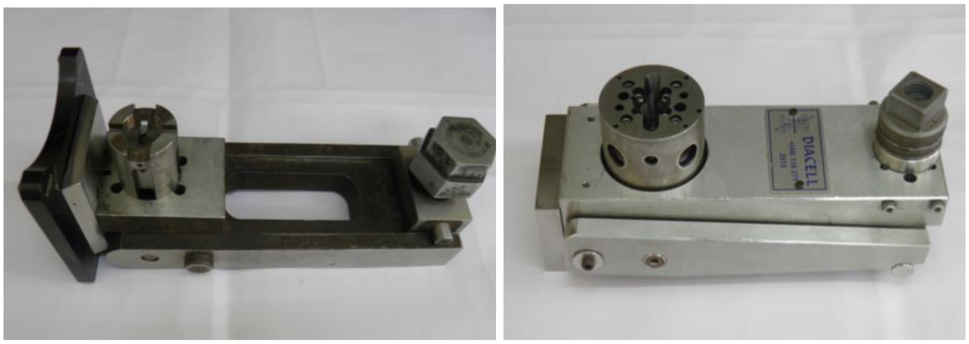

Fig. A.4: *Mao-Bell type diamond anvil cells used for studies presented in this thesis.*

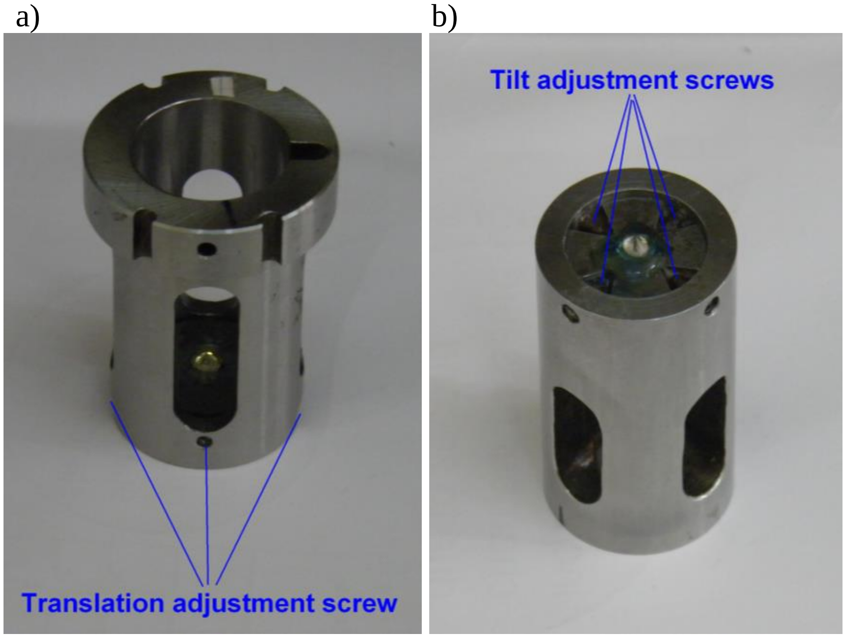

Fig. A.5: *Translation and tilt adjustment screws in a) cylinder and b) piston respectively.*

Due to the brittle nature of diamond the diamond anvil centering and tilt alignment is a crucial part of DAC preparation. Hence extreme care has to be taken to align the DA to prevent their premature failure. Figure A.6a and b shows unaligned DA wherein relative anvil translation and tilt is more than the experimentally accepted limits. In the case of Mao-Bell DAC as shown in Fig. A.5, the tilt adjustment screws on the piston are used to adjust the parallelism of DA and translation screws on the cylinder are used for their lateral alignment. The mechanism for applying a smoothly varying load is a belleville spring-loaded lever arm with a mechanical advantage of 5:1 actuated by a screw. This cell can sustain a pressure of ~ 1 Mbar with ordinary diamond anvils and is capable of generating a pressure of ~ 5 Mbar with bevelled DA [3].

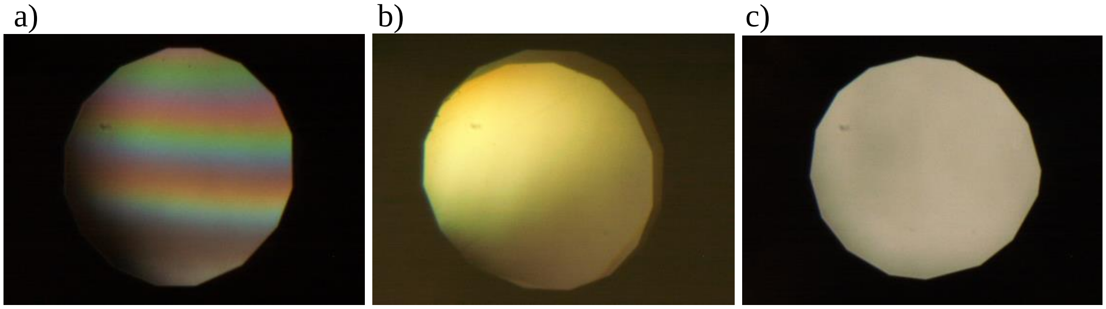

Fig. A.6: *a) Microscopic image of tilt misalignment between two DA. Optical path difference resulting from the tilt of the two culets result in the observed colour fringes; b) microscopic image of translation misalignment between the two DA; c) microscopic image of perfectly aligned DA.*

References:

[1] http://sites.coloradocollege.edu/pcervantes/facilities/

[2] https://www.almax-easylab.com/ProductList.aspx?id=10030

[3] R. Dias and I. F. Silvera, *Science*, **355**, 715 (2017).

B. X-ray Diffraction (XRD) Technique

X-ray diffraction (XRD) is an important and versatile analytical technique primarily used for phase identification of any material. It can provide information on the crystal structure, unit cell dimensions, phase fraction of different phases present in probed sample volume.

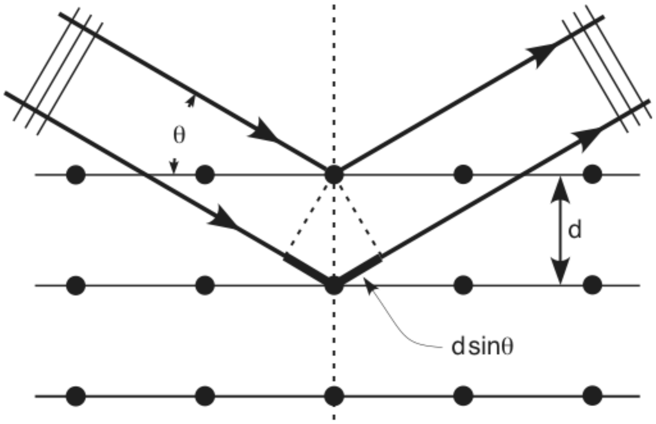

Fig B.1: *Schematic illustration of Bragg's law [1]*

The basic principle of XRD is the fact that x-ray wavelengths are of the same order as the atomic spacing in materials. Hence the scattering of x-rays by the core electrons gives rise to constructive and destructive interference in accordance with the superposition principle. The condition for constructive interference is given by Bragg's law (see Fig. B.1)

$$n\lambda = 2d_{hkl}\sin\theta \qquad \text{(B1)}$$

where n is an integer, λ the x-ray wavelength, d_{hkl} the distance between adjacent parallel planes, (h k l) are the Miller indices of crystal planes and 2θ is the scattering angle. Relations of d_{hkl} with lattice parameters for the seven lattice systems are tabulated in Figure B.2.

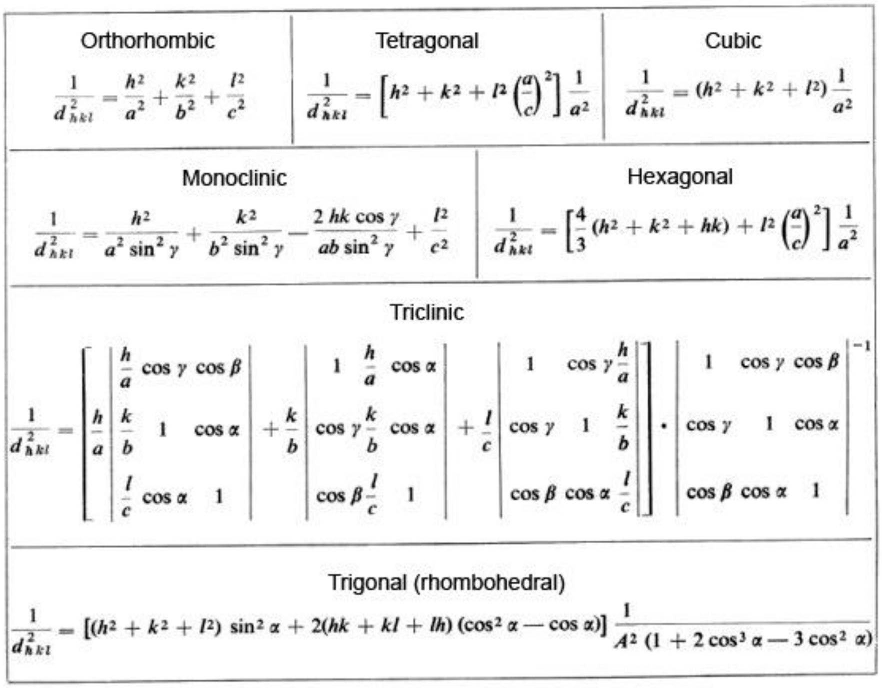

Orthorhombic

$$\frac{1}{d_{hkl}^2} = \frac{h^2}{a^2} + \frac{k^2}{b^2} + \frac{l^2}{c^2}$$

Tetragonal

$$\frac{1}{d_{hkl}^2} = \left[h^2 + k^2 + l^2\left(\frac{a}{c}\right)^2\right]\frac{1}{a^2}$$

Cubic

$$\frac{1}{d_{hkl}^2} = (h^2 + k^2 + l^2)\frac{1}{a^2}$$

Monoclinic

$$\frac{1}{d_{hkl}^2} = \frac{h^2}{a^2\sin^2\gamma} + \frac{k^2}{b^2\sin^2\gamma} - \frac{2hk\cos\gamma}{ab\sin^2\gamma} + \frac{l^2}{c^2}$$

Hexagonal

$$\frac{1}{d_{hkl}^2} = \left[\frac{4}{3}(h^2 + k^2 + hk) + l^2\left(\frac{a}{c}\right)^2\right]\frac{1}{a^2}$$

Triclinic

$$\frac{1}{d_{hkl}^2} = \left[\frac{h}{a}\begin{vmatrix} \frac{h}{a} & \cos\gamma & \cos\beta \\ \frac{k}{b} & 1 & \cos\alpha \\ \frac{l}{c} & \cos\alpha & 1 \end{vmatrix} + \frac{k}{b}\begin{vmatrix} 1 & \frac{h}{a} & \cos\alpha \\ \cos\gamma & \frac{k}{b} & \cos\alpha \\ \cos\beta & \frac{l}{c} & 1 \end{vmatrix} + \frac{l}{c}\begin{vmatrix} 1 & \cos\gamma & \frac{h}{a} \\ \cos\gamma & 1 & \frac{k}{b} \\ \cos\beta & \cos\alpha & \frac{l}{c} \end{vmatrix}\right] \cdot \begin{vmatrix} 1 & \cos\gamma & \cos\beta \\ \cos\gamma & 1 & \cos\alpha \\ \cos\beta & \cos\alpha & 1 \end{vmatrix}^{-1}$$

Trigonal (rhombohedral)

$$\frac{1}{d_{hkl}^2} = [(h^2 + k^2 + l^2)\sin^2\alpha + 2(hk + kl + lh)(\cos^2\alpha - \cos\alpha)]\frac{1}{A^2(1 + 2\cos^3\alpha - 3\cos^2\alpha)}$$

Fig. B.2: *Relations of d_{hkl} with lattice parameters for seven lattice systems where a, b, c, α, β and γ are lattice parameters of the crystal [2].*

Bragg condition gives only positional information of the diffracted x-ray beam whereas the intensity of diffracted light is given by Eq. B2 and Eq.B3.

$$I_{hkl} \propto \left|S_{hkl}\right|^2 \tag{B2}$$

$$S_{hkl} \equiv \sum_{j=1}^{m} f_j \exp\left[2\pi i\left(hx_j + ky_j + lz_j\right)\right] \tag{B3}$$

where S_{hkl} and f_{hkl} are structure factor and atomic form factor, x_j, y_j and z_j are fractional coordinates of j^{th} atom. The structure factor S_{hkl} sums the result of scattering from all the atoms in the unit cell to form a diffraction peak from the (hkl) plane of atoms. Thus the intensity of diffracted light is determined by i) position of atoms in atomic plane, *i.e.*, their fractional coordinates, and ii) atomic form factors (f_{hkl}) of atoms. f_{hkl} is a function of atomic number (Z) and increases with increasing Z.

References

[1] https://commons.wikimedia.org/wiki/File:Bragg_diffraction.png

[2] http://www.xtal.iqfr.csic.es/Cristalografia/parte_04-en.html.

C. Raman spectroscopy

Raman spectroscopy is a powerful spectroscopic technique used to observe the vibrational, rotational and other low energy excitations in materials. A compound's unique Raman spectrum arises from its molecular vibrations due to which this technique serves as a finger print of the molecule. Raman scattering is an inelastic scattering of photons by atom's elementary excitations in materials arising from a change in the polarizability. When a beam of monochromatic light is incident on the sample, photons are absorbed by it and scattered. The vast majority of photons are scattered elastically resulting in Rayleigh scattering, whereas a small fraction of light (~ one photon per 10^6 photons) is scattered inelastically giving rise to Raman spectrum. The wavelength of the Raman lines are hence different from the incident monochromatic light. Most of the Raman scattered photons are shifted to longer wavelengths *i.e.*, $\varepsilon < \varepsilon_0$, (Stokes shift), but a small portion are shifted to shorter wavelengths *i.e.*, $\varepsilon > \varepsilon_0$ (anti-Stokes shift). Stokes lines result when, during light matter interaction, the system excited from the ground state returns to a higher energy state. The anti Stokes lines, on the other hand, are observed during the transition of system from excited state to the ground state. In each case, the incident photon excites an electron into a higher virtual energy level and then the electron decays back to a lower level, emitting a scattered photon. The relative intensity of Stokes and anti Stokes lines depend on the number of electrons occupying the high energy states. Figure C.1 shows Raman and Rayleigh scattering in the form of energy level diagram.

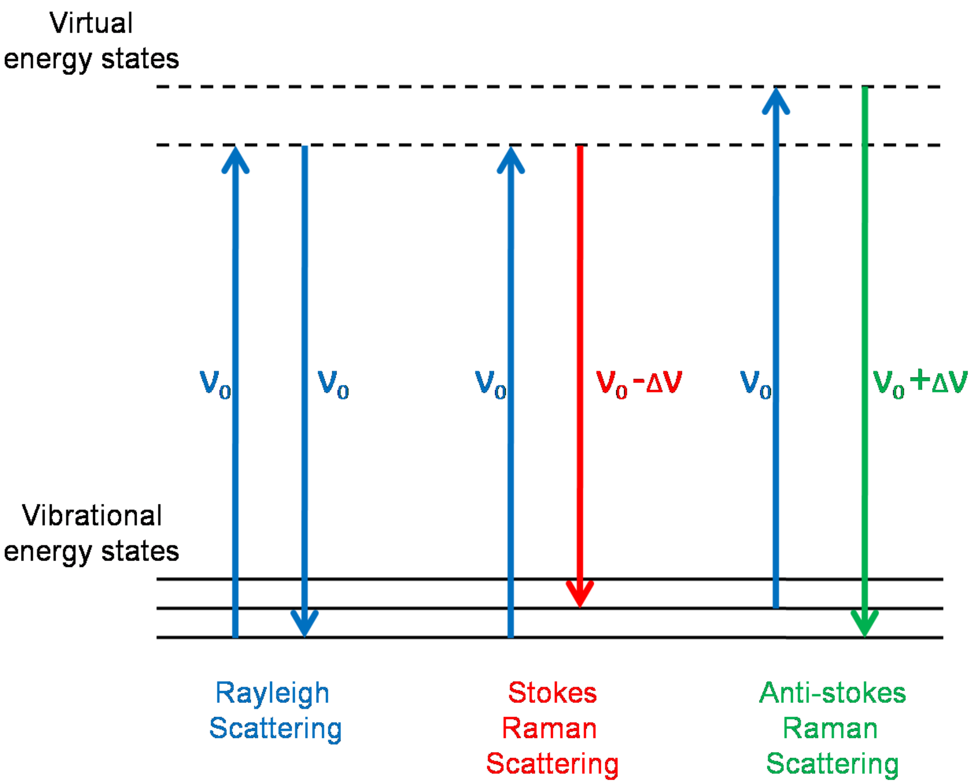

Fig. C.1: *Energy level diagram depicting Rayleigh, Stokes and anti Stokes Raman scattering.* ν_0 *is incident photon frequency, energy* $\varepsilon_0 = h\nu_0$, *and* $\Delta\nu$ *is frequency corresponding to the energy difference between excited and ground state respectively.*

D. Scanning Electron Microscopy (SEM)

Scanning electron microscopy **(**SEM) is a non-destructive technique used to investigate the surface morphology of materials. It typically consists of a vacuum chamber, an electron gun, sample stage and various detectors (see Fig. D.1). In the electron gun, electrons are produced either by field emission or thermionic emission technique and are accelerated to a high voltage up to 30 kV. These electrons are focused to a narrow beam and directed on to the sample. The high energy electron beam interaction with the material in SEM generates secondary electrons, backscattered electrons, characteristic x-rays *etc.*, depending on the nature of interaction *viz.*, (elastic or inelastic). Secondary electrons and backscattered electrons are commonly used for imaging the samples.

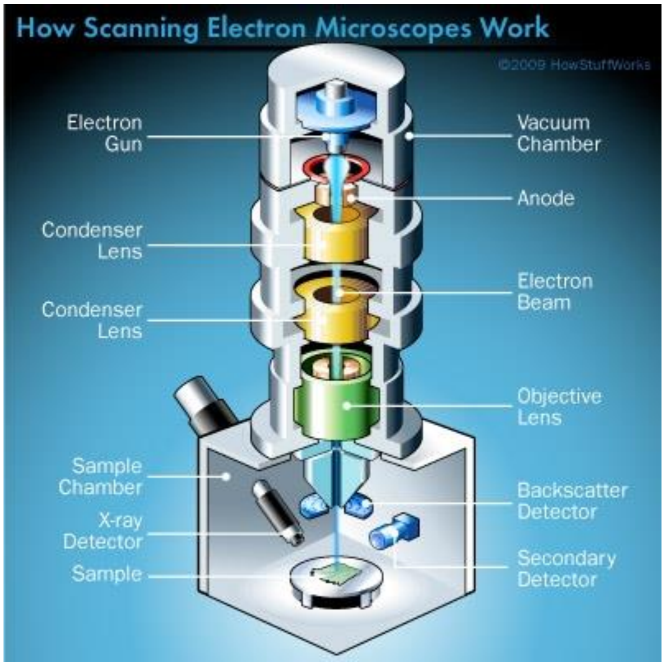

Fig. D.1: *Schematic diagram of Scanning Electron Microscope (SEM) [1].*

Reference:

[1] https://science.howstuffworks.com/scanning-electron-microscope2.htm.

E. Ruby Pressure Scale

Ruby gauge is an important and popular gauge for pressure determination in DAC based high pressure experiments. Compositionally, ruby is 0.05 wt% Cr^{3+} doped alumina. It has a strong luminescence doublet peaks R_1 and R_2 at 694.2 nm and 692.8 nm under ambient conditions. Energy band U or Y is populated when visible laser is incident on the ruby crystal. Pumping of these levels populates the metastable states $^2T_1$ and ^2E by fast non-radiative decay. Subsequently, much slower ($\tau \sim 3$ ms) radiative transition from metastable state ^2E to ground state takes place giving rise to R_1 and R_2 lines.

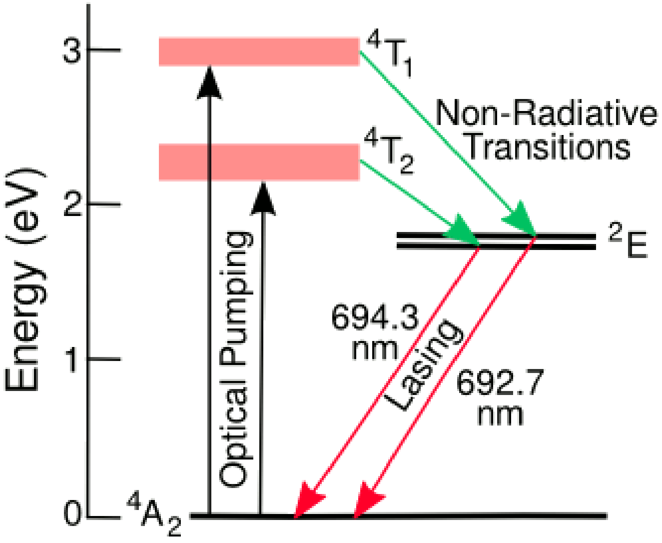

Fig. E.1: *Energy level diagram for fluorescence of Ruby [1].*

Initially, ruby pressure gauge was developed by calibrating the wavelength shift of R_1 line with pressure against the Decker equation of state for NaCl up to 19.5 GPa [2]. It was found that the R_1 line shifts approximately linearly with pressure, with a coefficient $dP/d\lambda=2.746$ Kbar/Å or $d\lambda/dP= 0.364$ Å/Kbar. Calibration of ruby scale at higher pressure up to 180 GPa was subsequently done using shock equation of state data of some metals (like Cu, Mo, Pd and Ag) [3].

Pressure calibration for quasihydrostatic and hydrostatic experiments can be expressed as

$$P = \left(\frac{1904}{B}\right)\left[\left(1+\left(\frac{\delta\lambda}{694.24}\right)\right)^{B} - 1\right] \qquad \text{(E1)}$$

where P is in GPa and δλ is the wavelength shift of R_1 line in nm and B is 7.665 and 5 for hydrostatic and quasihydrostatic conditions respectively.

References

[1] http://freewiring.today/ruby-laser-with-energy-level-diagram.html

[2] D. L. Decker, *J. Appl. Phys.*, **42**, 3239 (1971).

[3] H. K. Mao, P. M. Bell, J. W. Shaner and D. J. Steinberg, *J. Appl. Phys.*, **49**, 3276 (1978).

F. Rietveld Refinement

The x-ray powder diffraction data analysis consist of three parts *viz.*, (i) conversion of the azimuthal integration of 2D image plate data to produce a 1D output in 2θ, d-spacing, or q-space using Fit2D software, (ii) Le Bail fitting of 1D intensity *vs* 2θ diffraction profile and (iii) Rietveld refinement of the diffraction profile using GSAS software [1].

The first step of integration of the 2D data necessitates accurate calibration of experimental geometry such as sample to detector distance, beam centre, detector tilt and detector rotation angle. Standards (Calibrant) such as cerium oxide (CeO_2), lanthanum hexaboride (LaB_6) *etc.*, whose lattice parameters and hence d-spacings are accurately known, are used to calibrate the above parameters along with x-ray wavelength. The Fit2D software then interpolates each pixel on the image to a d-spacing and integrates to give 1D diffraction peak profile [2].

The second step, *i.e.*, Le Bail profile refinement requires the initial guess lattice parameters and space groups of all solid phases present in the XRD data. In this method, a polynomial profile describing the background to the diffraction profile is calculated, and this is refined using a least squares method. Then the individual integrated peak intensities and shapes are treated as least squares parameters. The peak shapes are modelled as Gaussian, Lorentzian or Pseudo-Voigt profiles (Pseudo-Voigt peak profile is a convolution of a Gaussian and a Lorentzian peak). H_k^2 is the variance of diffraction peak, which varies with 2θ and is given by

$$\mathrm{H}_{\mathrm{k}}^{2} = U \tan^{2}\theta_{k} + V \tan\theta_{k} + W \qquad \text{(F1)}$$

Furthermore, the individual Bragg peak positions are obtained through refinement of the unit cell dimensions *i.e.*, the lattice parameters a, b, and c, and the angles between them *viz.*, α, β, and γ.

The Le Bail refinement method provides information about the lattice parameters and peak shape, but does not take into account the atomic position, site occupancies, phase fraction, thermal effect and preferred orientation of the sample.

In the third step, Rietveld refinement is performed on Le Bail refined data. In this method, the structure factor and Debye-Waller factors for each atom are considered to calculate the peak intensities. The principle of Rietveld refinement is to minimize the sum of the differences of observed and calculated profile (function S) using linear least square method.

$$\mathrm{S} = \sum_k w_k \left(Y_k^o - \frac{Y_k^c}{c} \right)^2 \tag{F2}$$

where w_k is the statistical weight, c is an overall scaling factor. Y^0 and Y^c are observed and calculated profile respectively.

Reference:

[1] B. H. Toby, *J. Appl. Cryst,*. **34**, 210 (2001).

[2] A P Hammersley, *ESRF Internal Report*, **ESRF98HA01T**, FIT2D V9.129 Reference Manual V3.1 (1998).